

Alma Mater Studiorum-Università degli Studi di Bologna
Dipartimento di Chimica Fisica e Inorganica

Dottorato di Ricerca in Scienze Chimiche (XIX Ciclo)
S.S.D. CHIM/02

PhD Dissertation

*Self-Organisation Phenomena in Thin Films and
Molecular Nanostructures*

Presented by:

Dr. Jean Crispin Kengne

Supervisor:
Prof. Aldo Brillante

Co-supervisor:
Dr. Fabio Biscarini

PhD Coordinator:
Prof. Vincenzo Balzani

Bologna, March 2007

CONTENTS

1	<u>General introduction</u>	1
1.1	Nanotechnology and Nanostructures	1
1.1.1	Bottom up fabrication and Self organisation	2
1.1.2	History of the idea	3
1.1.3	Self-organisation vs. entropy	5
1.1.4	Self-organisation in Chemistry and Biology	5
1.1.5	Self-organisation and Self assembly	6
1.2	Rotaxanes: what are they?	7
1.2.2	Rotaxanes synthetic strategies	7
1.2.3	Self-organisation of rotaxanes nanostructures	9
1.3	Organic semiconductors	13
1.3.1	Quinquethiophenes: What are they?	13
1.3.2	Organic Field Effect Transistors.	14
1.3.3	Thin Films and their importance in technology.	19
1.3.4	Thin films growth modes	20
1.3.5	High vacuum deposition	22
1.4	Thesis overview	23
	References	23
2	<u>Self Organisation of Rotaxane Thin Films into</u>	

<u>Spatially Correlated Nanostructures.</u>	31
2.1 Introduction	31
2.2 Experimental and methods	32
2.2.1 Materials and thin films	32
2.2.2 TEM /SAED experiments	33
2.2.3 Morphology characterisation	33
2.2.4 Modelling	34
2.3 Results	34
2.3.1 Thermal annealing of rotaxane 1	34
2.3.2 Thermal annealing of rotaxane 2	39
2.3.3 Solvent annealing of both rotaxanes	42
2.3.4 Texturing analysis by AFM of rotaxane 1	43
2.3.5 Structural investigation by TEM and SAED	44
2.3.6 Energetics of rotaxane Surfaces	47
2.4 Discussion and conclusions	50
References	53
3 <u>Thickness control of Rotaxane Thin Films grown by Spin Coating</u>	55
3.1 Introduction	55
3.2 Theory of spin coating.	56
3.3 Model of the spinning process	57

3.3.1	Angular velocity, concentration and viscosity	58
3.3.2	Solvent evaporation and solute diffusivity	59
3.4	Experimental section	61
3.5	Results and discussion	62
3.6	Conclusion	66
	References	67
4	<u>Viscoelastic properties of rotaxane</u>	69
4.1	Introduction	69
4.2	Forces in AFM	69
4.3	Force Curves measurements	72
4.4	Theoretical considerations	74
4.5	Experimental section	75
4.6	Results and discussion	76
4.6.1	Recrystallisation by nucleation and growth of holes	76
4.6.2	Recrystallisation by Ostwald ripening	76
4.6.3	Comparison of Surface Energies by three methods	78
4.7	Conclusions	79
	References	80
5	<u>FET device Performance, Morphology and X-ray Thin Film of unsubstituted and modified Quinquethiophenes</u>	80
		83

5.1	Introduction	83
5.2	Motivations and Aim of the work	84
5.3	Experimental section	85
5.3.1	Materials, instruments and methods	85
5.3.2	Results	86
5.3.2.1	Results by XRD	86
5.3.2.2	Results by AFM	91
5.3.3	Field Effect Transistor	95
5.4	Discussion and Conclusion	100
	References	104
	Appendix	108

Keywords

Self-Organisation

Thin Films

Nanostructures

Rotaxane

Quinquethiophene

OFETs

AFM

Spin Coating

Chapter 1

General introduction

1.1 Nanotechnology and Nanostructures

Nanostructures are systems whose size in at least one dimension is less than 100 nm. The variety of interdisciplinary research fields dealing with these nanosized materials is termed Nanotechnology. The idea of nanotechnology dates back to 1959, when the physicist Richard Feynman presented his famous talk entitled “There’s plenty of room at the bottom” [1] at the annual conference of the American Physical Society. However, the very birth of nanotechnology has been represented by the invention of the Scanning Tunneling Microscope (STM) by Binnig and Rohner, [2] which made possible to observe materials down to single atoms in real space and manipulate them one by one by making use of the strong interaction between tip and sample at small working distance. [3] Following Moore’s law, which states that the density of transistors in a chip doubles approximately every eighteen months, electronic components and circuits have been downscaled to dimensions of hundreds of nanometers, thanks to the development of sophisticated techniques such as photolithography, electron beam lithography and focus ion beam. However nowadays nanotechnologies are not limited to the improvement of microelectronics devices by means of their miniaturisation, but the application fields are more numerous, viz. solid state technologies, biotechnologies, device technologies, sensors, design and control of innovative nanostructured materials and many more. Nanostructured

materials have revealed peculiar new properties associated with size and spatial organisation.

1.1.1 Bottom up fabrication and Self- Organisation

Nanostructured materials can be fabricated following two different strategies, as schematised in Figure 1.1 In the top-down process a macroscopic object is progressively cut and shaped in order to obtain a functional architecture.

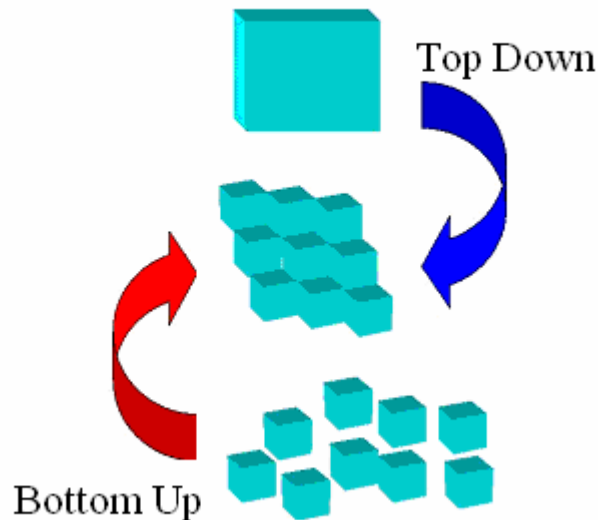


Figure 1.1 Schematisation of the approaches “Bottom Up” and “Top Down” used for the fabrication of nanoarchitectures.

This methodology is adopted by the lithographic techniques, which have been used in microelectronics to produce circuitry of high quality. However, despite of the possibility to fabricate very reliable and complex architectures, the improvement of lithography to yield smaller and smaller objects is reaching its physical limit because of undesired phenomena such as diffraction of radiation through the slit of a photolithographic mask and uncontrolled diffusion of electrons

inside polymeric photoresists. Moreover these techniques are very expensive and in the case of electron beam lithography, nanoarchitectures can only be produced serially, which severely limits their industrial applications. In view of these limitations the bottom-up approach has been more recently developed. [2,4] With this technique architectures are built by manipulation of molecules, which are assembled into functional structures. Macroscopic tools, because of their dimensions, are not suitable to arrange molecules at specific positions, and the process is inadequate to build sophisticated functional architectures. Therefore the instruments for handling molecules have been incorporated into the molecules themselves, with a new approach called “self-assembly”.

Bottom-up nanotechnologies are based on molecules endowed with the capability of organising into more complex meso and nanoscopic structures. The driving forces of this organisation are complementary specific interactions on one hand and intermolecular competitive interactions such as hydrophilic/hydrophobic forces, hydrogen bonds, Van der Waals interactions on the other hand. All these forces contribute to minimise the free energy of the possible supramolecular configurations. [5,6] The ultimate purpose of bottom-up nanotechnology is hence the fabrication of architectures which are self-built starting from suitably designed molecules. Moreover, these structures have to be connected with the “macroscopic world”, that is, they should give a detectable response when addressed by a stimulus.

1.1.2 History of the idea

The idea that the dynamics of a system may lead to increase the inherent order of the system itself has a long history. One of the earliest statements of this idea was by the philosopher Descartes, in the fifth part of his “*Discours de la methode*”, where he presented it

hypothetically. Descartes introduced the idea that the ordinary laws of nature tend to produce organisation. The term "self-organizing" seems to have been first introduced in 1947 by the psychiatrist and engineer Ross Ashby. [7] Self-Organisation as a word and concept was used by those associated with general systems theory in the 1960s, but did not become commonplace in the scientific literature until its adoption by physicists and researchers in the field of complex systems in the 1970s and 1980s. It defines a process in which the internal organisation of a system, normally an open one, improves spontaneously without being driven or managed by an external source. Self-organizing systems display emergent properties. Although most robust and unambiguous examples of self-organizing systems are from physics, where the concept was first noted, self organisation is present in many other disciplines like chemistry, biology, mathematics, computer science and human society. Self-organisation, despite its intuitive simplicity as a concept, has proven notoriously difficult to define and pin down formally or mathematically, and it is entirely possible that any precise definition might not include all the phenomena to which the label has been applied. Von Bertalanffy presented the notion of self-organization as the ability of a system to grow towards more organisation and complexity, that is to say his capacity of maintaining unceasing exchanges of matter, energy and information with his environment, and to regulate in the most adapted way, his metabolism.

Self organisation relies upon four basic ingredients: positive feedback, negative feedback, balance of exploitation and exploration, and multiple interactions. To answer the basic question, these ingredients have to be identified for the various phenomena and one has to understand these ingredients and combine to generate structural organisation.

1.1.3 Self-Organisation vs. Entropy

The idea of self-organisation challenges the earlier paradigm of ever-decreasing order which was based on a philosophical generalisation of the second law of thermodynamics. However, at the microscopic or local level, both need not to be in contradiction: it is possible for a system to reduce its entropy by transferring it to its environment. In open systems, it is the flow of matter and energy through the system that allows the system to self-organise and to exchange entropy with the environment. This is the basis of the theory of dissipative structures. Ilya Prigogine noted that self-organisation can only occur far away from thermodynamic equilibrium. [9] It would appear that, since isolated systems cannot decrease their entropy, only open systems can exhibit self-organisation. However, also a closed system can gain macroscopic order while increasing its overall entropy. Specifically, a few of the system's macroscopic degrees of freedom can become more ordered at the expense of microscopic disorder. This is particularly relevant for dynamical systems formed by a complex of building blocks of specific physical properties or biological systems where the increasing organisation of large molecules is more than compensated for by the increasing entropy of small molecules, especially water. [10]

1.1.4 Self-Organisation in Chemistry and Biology.

Non covalent interactions play critical roles in the biological world. Thus, with just a few building blocks, strands of nucleic acids allow huge amounts of information to be stored, retrieved, and processed via weak hydrogen bonds. Similarly, a large array of signalling molecules within cells recognizes subtle differences in protein surfaces. Beyond molecular chemistry based on the covalent bond, supramolecular chemistry has implemented these principles of molecular information

in chemistry. Through manipulation of intermolecular non covalent interactions, it explores the storage of information at the molecular level and its retrieval, transfer, and processing at the supramolecular level. These occur via interactional algorithms operating through molecular recognition events based on well-defined interaction patterns (such as hydrogen bonding arrays, sequences of donor and acceptor groups, and ion coordination sites). The goal of supramolecular chemistry is to achieve the control over the complex spatial (structural) and temporal (dynamic) features of matter through self-organisation. [11]

1.1.5 Self-Organization and self assembly

Self assembly is the spontaneous association of molecules under equilibrium conditions into stable, structurally well defined aggregates joined by non covalent bonds. [12] Examples are molecular cages containing a weakly bound dipoles, interlocked rings, self assembled monolayers. A particularly attractive goal is the self-assembly of nanostructures. In order to connect nanostructures to the outside world, viz by the so call integration across the length scales, it is necessary to build up larger assemblies by guided self-assembly. The information necessary for the organization process is embedded in the components and is expressed through molecular interactions. A distinction can be made between self organisation like the formation of crystals, vesicles or liquid crystalline phase and the much broader principle of self assembly that governs the spontaneous generation of even very larges systems capable of executing complex functions. Fascinating examples for making more complex systems in which a self assembly process allows also the design of specific functions, are the mechanically interlocked structures such as catenanes and rotaxanes [13] where self organisation is mainly governed by multiple interactions.

1.2 Rotaxanes: what are they?

The word rotaxane derives from the latin “rota” meaning wheel and “axis” meaning axle. In chemistry, the [2] rotaxanes (Figure 1.2) (the prefix indicates the number of the interlocked components) represent a group of compounds in which a macrocycle (wheel) is strung in a bead on a linear component (axle) bearing bulky groups at both ends to prevent the components from disassembling. Rotaxanes without such a physical barrier are termed pseudorotaxanes. No covalent bond holds the components together, but rather mechanical bonds are responsible for the linking of the components. Thus, rotaxanes behave like well defined molecular compounds with properties significantly different from those of their individuals components. These unique features offer the possibility of designing nanoscopic equivalents of bearings, joints, motors, rotors, pistons, and other macroscopic assemblies, composed of interlocked mechanical parts [14].

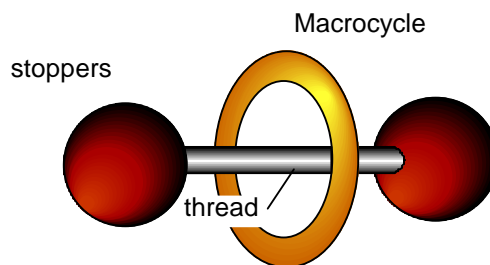


Figure 1.2. Schematic presentation of a [2] rotaxane

1.2.2 Rotaxanes synthetic strategies

Three different routes are described in literature for the synthesis of rotaxanes: threading, clipping and slippage. Although their synthesis is not the subject of this thesis, a brief description of the methods is reported in the following and is schematically illustrated in Figure 1.3

In the “**threading**” procedure, the macrocycle will first encircle the thread to form a so-called pseudorotaxane. By endcapping the thread with bulky groups that prevent the dethreading, a [2] rotaxane is formed.

In the “**clipping**” method, the macrocycle is assembled in the presence of the endcapped thread or dumbbell by condensation.

As a third possible route, careful selection of the size of the macrocycle can allow “**slippage**” of the cyclic molecule over the blocking groups at elevated temperature and yields, depending on the energy barrier, either rotaxanes or pseudorotaxanes. [13]

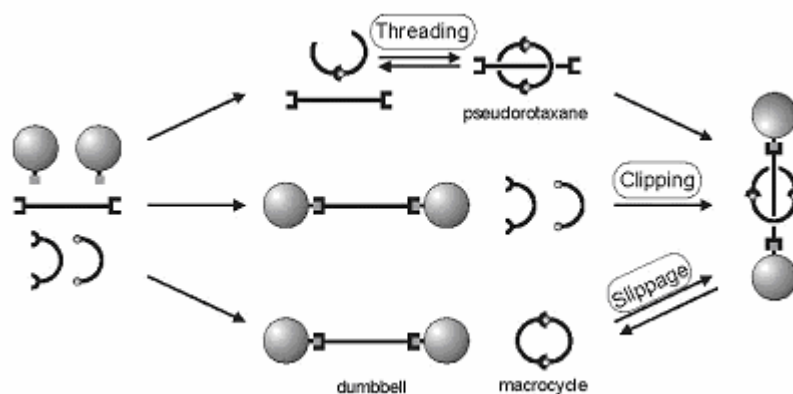


Figure 1.3. Three different strategies for the synthesis of [2] rotaxanes.

The choice of one of these three routes in the preparation of a rotaxane depends mainly on the chemical nature of the different components and on the chemistry required to establish the interlocked molecule. An interaction between the two individual components is very often the driving force in the synthesis of rotaxanes. The different types of interactions, which can occur in the mechanically linked species can be divided into Van der Waals interactions, hydrophobic interactions, hydrogen bonding, donor–acceptor interactions and transition metal coordination.

In the case of rotaxanes studied in this thesis work the most important interactions are hydrogen bonding and $\pi - \pi$. They are tertiary amide-based rotaxanes as depicted in Figure 1.4 left and right synthesized by Leigh and co-workers. [15,16] Here after they will be called rotaxane **1** and rotaxane **2** respectively. The decisive element for molecular recognition is the mono amide functionality. Hydrogen bond is essentially responsible for the self organisation process whereas π - π interactions are thought to be of only minor significance.

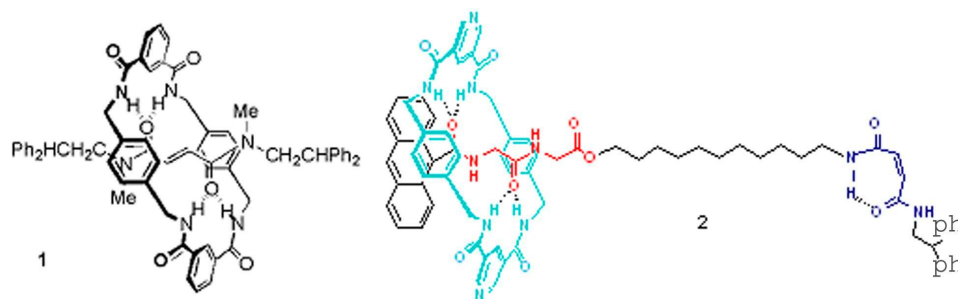


Figure 1.4 Chemical structure of the [2] rotaxanes, investigated in this thesis. They were termed rotaxane **1** and rotaxane **2** respectively.

1.2.3 Self organisation of rotaxanes nanostructures

Rotaxanes are molecular systems that respond to an external stimulus (electrical, chemical, optical, mechanical, or environmental) and modify their co-conformation accordingly. Therefore, they are potentially interesting as molecular actuators, [14] building blocks for mechanical molecular machines [14] and potential memories and sensors. [14] Rotaxanes form a class of molecular architectures with adaptive functionality. [14] Several examples of controllable or triggered motions (Figure 1.5) of the macrocycle with respect to the thread have been reported, resulting in changes of properties such as conductivity, [17] circular dichroism, [18] and fluorescence. [16,19]

These results suggest that new paradigms for switching, information storage, sensing, adaptive surface behavior, and smart coatings could be developed based on rotaxane architectures. However, the degree to which such effects, which have mostly been observed in solution, can be transferred to the condensed phase is not yet clear, [20] especially with respect to the technologically relevant medium of thin films. Nor, indeed, is it clear how the stimulus/response process can be most effectively controlled.

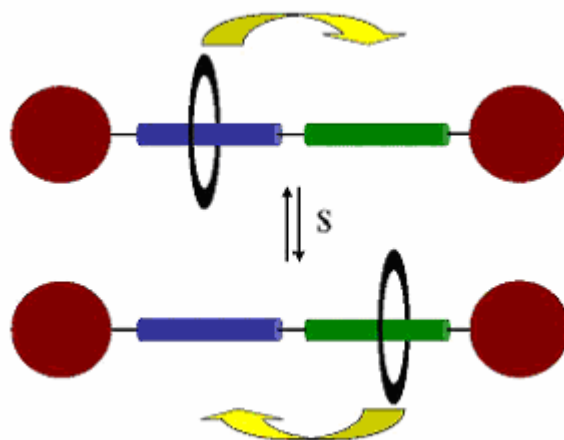


Figure 1.5. Example of a triggered motion of the macrocycle in a [2] rotaxane (reversible shuttling of the macrocycle).

There have been many studies on the triggered response of rotaxane thin films. [21] The experimental results on electrical switching of a rotaxane system developed by Stoddart and Heath have raised several questions related to the mechanism, whether it occurs at a single-molecule level [22] or it is due to a local re-organisation. [23] The analysis of the energetics of a different rotaxane system in the solid state suggested that the mobility of the macrocycle with respect to the thread would be enhanced if the hydrogen bonding ability of the macrocycle was saturated by interactions with the thread rather than by

intermolecular interactions. [24] This assertion was supported by atomic force microscopy (AFM) indentation of microcrystals, which demonstrated the larger plasticity of the rotaxane crystals with respect to crystals of either the thread or the macrocycle. Cavallini et al. recently reported a remarkable phenomenon whereby a local mechanical perturbation applied via AFM operated at a precise load force on a region of a rotaxane thin film transforms it into arrays of regularly spaced nanostructures (dots), [25] as shown in Figure 1.6, that could coalesce to form lines [26] under the right conditions.

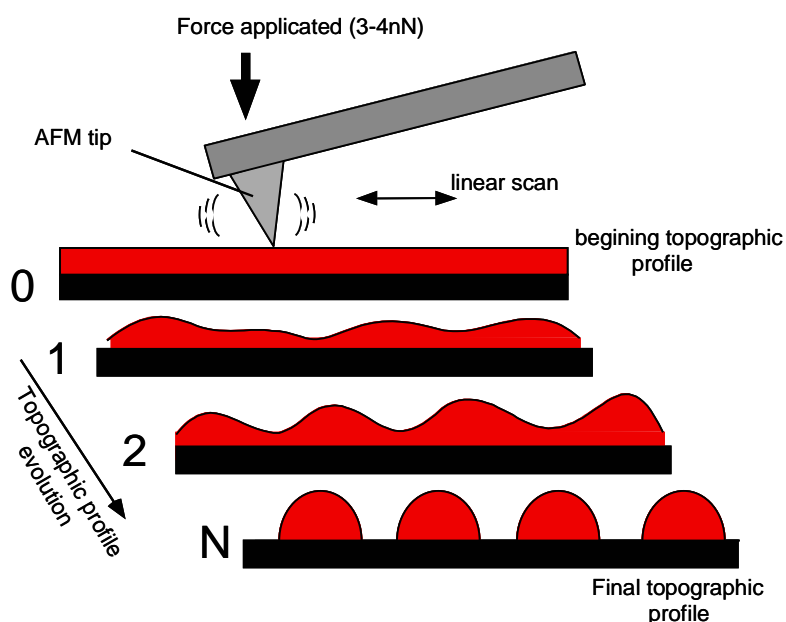


Figure 1.6. Self-organisation of a thin rotaxane film into nanodots upon a mechanical stimulus (AFM Tip).

This self-organization occurs collectively as the perturbation is applied. The phenomenon is reminiscent of the phenomenology of spinodal dewetting [27] since the characteristic length scale is controlled by the film thickness. Getting a good control of these nanodots will lead to the birth of new information storage devices. (Figure 1.7).

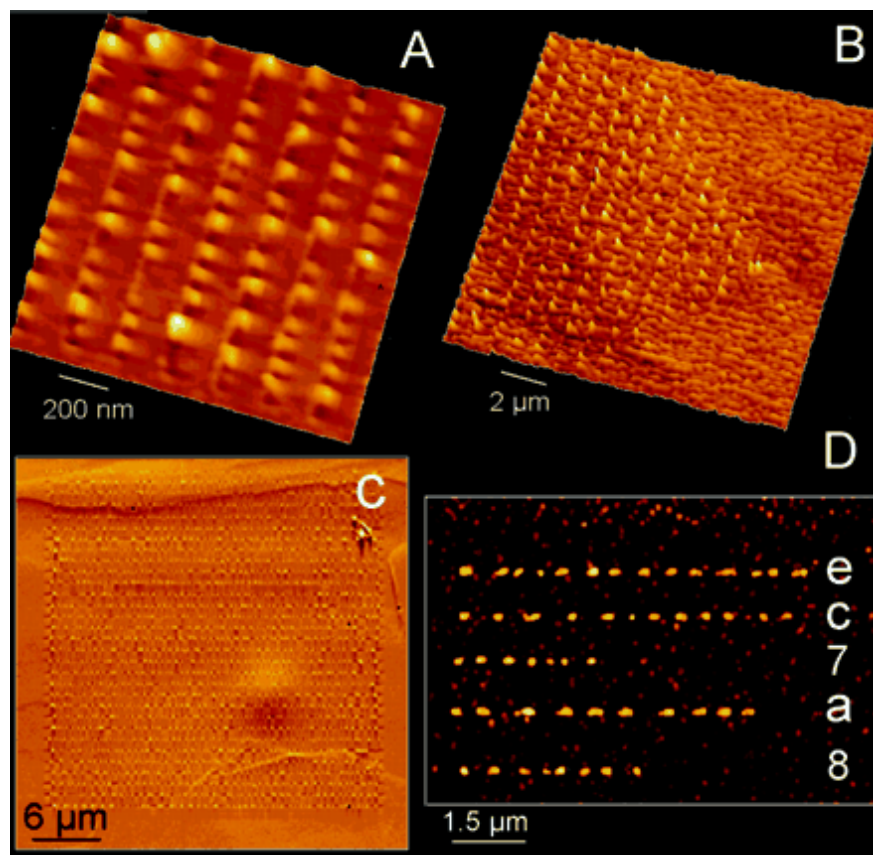


Figure 1.7. (A) Array of dots fabricated of rotaxane **1** by individual line scans of the AFM tip on a 5-nm-thick film of rotaxane **1** deposited on highly oriented pyrolytic graphite. (B) For a given thickness (here 20 nm), the number of dots is linearly proportional to the scan length. The number of dots can be determined with an accuracy of at least 2%. Film thickness controls the characteristic size. Varying the film thickness in the range between 3 and 35 nm, interdot distance increases from 100 to 500 nm, the dot full-width-half-maximum from 40 to 250 nm, and the dot height from 1 to 20 nm, with a dispersion of 10 to 20%. (C) Pattern made of 31 lines with 45 dots each on an ≈ 30 by $30 \mu\text{m}^2$ area on a thicker film. (D) Proof-of-concept for information storage. The sequence "e c 7 a 8" in the hexadecimal base corresponds to the number 968616. (From ref. 25).

In this thesis we have studied the mechanism of the self-organisation of rotaxane **1** and **2** thin films upon thermal and chemical stimulus and the effect of the substrate on their thin films. Then we have determined the phenomenological parameters which can be used to control the thickness of rotaxane films, by spin coating. Thus, we have studied the viscoelastic properties of rotaxane **1** since it exhibits

nanocrystals when annealed, that we have not obtained with the rotaxane **2**.

1.3 Organic semi conductors

1.3.1 Quinquethiophenes: What are they?

Thin films of quinquethiophenes have been investigated because of their relevance as active layer on Organic Field Effect Transistor (OFETs)

Quinquethiophenes [28] are a family of oligothiophenes with 5 thiophenes units linked. They are a well know organic semiconductors materials. The molecular structures of the oligomers we have investigated are shown in Figure 1.8.

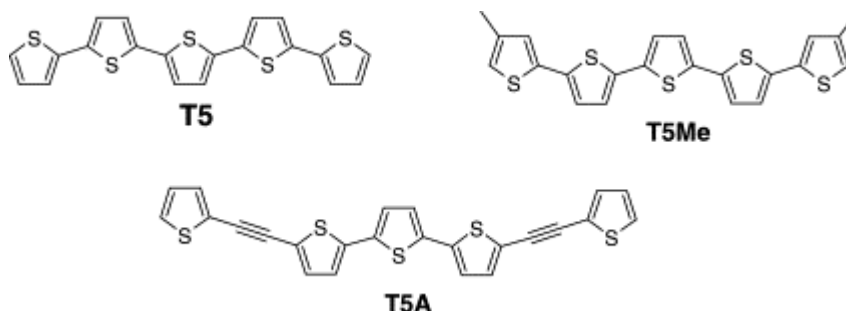


Figure 1.8. Molecular structure of unsubstituted quinquethiophene (T5) substituted quinquethiophene (T5Me) and modified quinquethiophene (T5A).

The immensely broad spectrum of organic semiconductor molecules can be classified into two major groups: polymers, and small weight molecules or oligomers. Polymers are long-chain molecules formed by the repetition of molecular units. The number of repetition units is indeterminate, thus leading to a variable molecular mass. On the contrary, small weight molecules have a well defined molecular weight. From the point of view of their electronic and optic properties both groups can be considered rather similar, being the main

difference the thin-film deposition methods. In this sense, polymers show the advantage of being processable from solution. Oligomers are in most of the cases insoluble and are thus deposited by technically more demanding methods with consequently higher associated costs. However, their major advantage with respect to the polymers is that they can be grown in thin films of high purity and crystalline order, two important requirements to obtain high charge carrier mobility.

Thin films of organics oligo-thiophenes are of great interest as active layers in devices such as field-effect transistors, [29,30] light emitting diodes, [31] solar photovoltaic cells. [32] The transport phenomena in these molecular devices depends on the interplay between electronic structure and order in the molecular assembly. These films allow for the investigation of fundamental physical phenomena, such as mobility, charge injection, and interface phenomena in organic layers, that critically depend on structure [33] and morphology. [34]

1.3.2 Organic Field Effect Transistors (OFETs)

The potential use of organic semiconductors in field-effect transistors (OFETs) was already demonstrated in the late eighties. [35,36] Since then, tremendous efforts have been devoted to the development and optimization of these devices, which consequently lead to a rapid progress, to the level that the performance of good organic thin film transistors (OTFT) rivals that of commercial amorphous silicon transistors. Thin film field-effect transistors consist on a semiconducting film contacted by metallic source and drain electrodes, and a third electrode (gate) separated from the semiconducting film by a dielectric layer. There are several different options to arrange the elements of the device, being the main difference the relative position of the contacts with respect to the

semiconductor (on top or bottom), as shown in Figure 1.9. The typical dimensions for the channel length (L) and width (W) are in the range of 1 to 50 μm and 100 μm to 11 cm respectively, though devices with channel lengths in the nanoscale have already been demonstrated. [37]

The operation of OFETs depends on the applied gate and source-drain voltages. [37, 38] When a positive voltage is applied to the gate (V_G), negative charges are capacitively induced in the semiconducting layer (Figure 1.9) and vice-versa. Much of this charge is mobile and thus moves in response to an applied source-drain voltage (V_D).

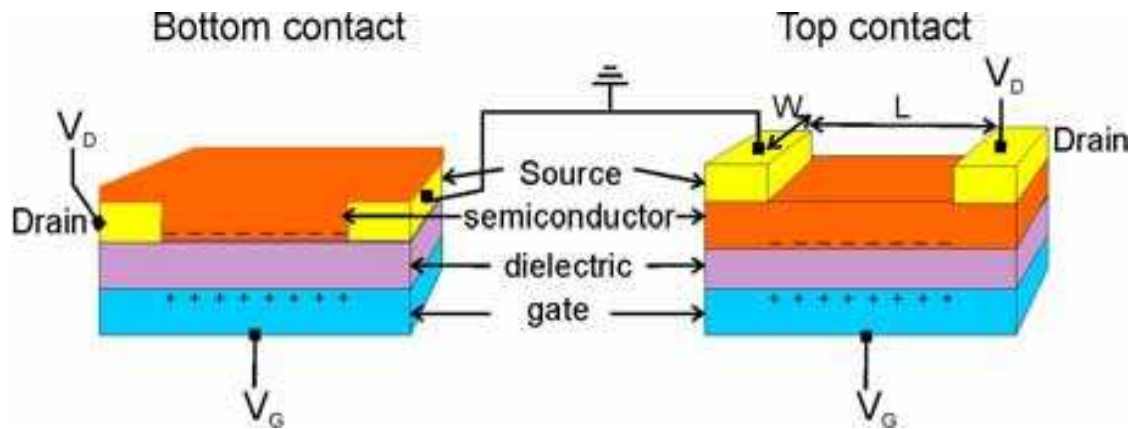


Figure 1.9. Representation of thin film transistors possible configurations.

Ideally, at $V_G=0$ there is an absence of mobile charge carriers and a consequently low conductance in the semiconducting film. The device is “off”. Upon gate voltage application, the charge injection increases the conductance and the device is turned “on”. In order to clarify the underlying concepts of the field effect transistor operation, Figure 1.10 shows, in a simplified way, a scheme of the evolution of the electronic energy levels in the device. The application of V_G shifts the semiconductor energy levels with respect to the Fermi levels of the contacts, until the HOMO ($V_G<0$, p-channel operation) or the LUMO ($V_G>0$, n-channel operation) reach the Fermi level. This leads to a charge injection into the semiconductor and to an electric current

between source and drain upon application of a drain voltage. However, additional aspects not taken into account in this simple representation make that, with few exceptions, a given organic semiconductor acts only as hole or electron conductor and is consequently classified as n- or p-type semiconductor.

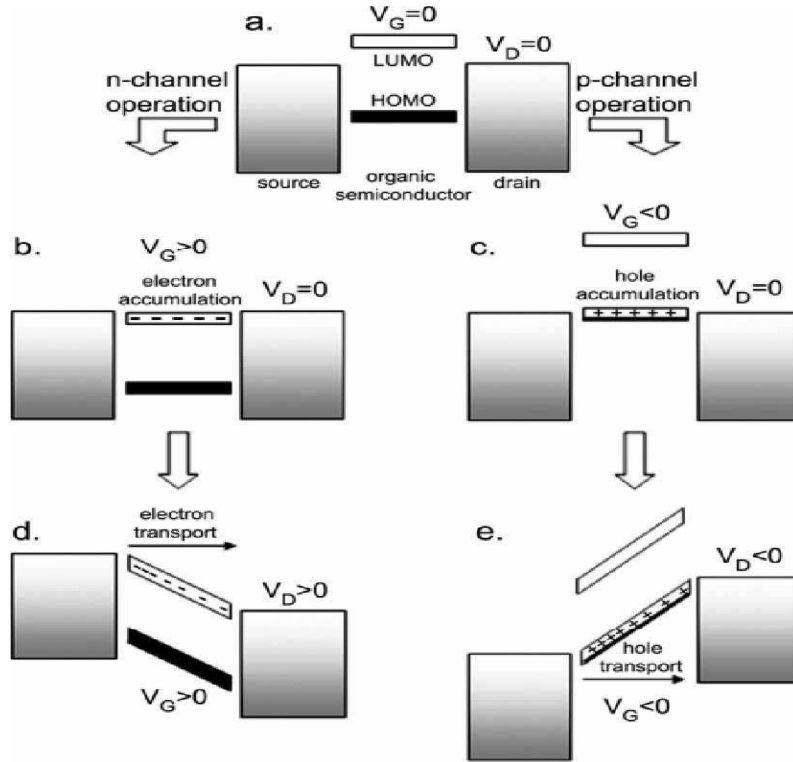


Figure 1.10 (a) Idealised energy level diagram of an organic thin TFT at $V_G=0$ and $V_D=0$. (b-e) showing the principle of field effect transistor operation for the case of (b) electron accumulation and (c) transport and hole (d) accumulation (e) transport (from reference 37)

If we define the “threshold voltage” V_T as the voltage necessary to generate mobile charge carriers in the semiconductor, the current-voltage relationship in an OFET can be described, as for conventional semiconducting devices, [39,40] by:

$$I_{D,lin} = \frac{W}{L} C \mu_{lin} \left[(V_G - V_T) V_D - \frac{V_D^2}{2} \right]$$

This equation is called “linear regime” equation, and is valid when

$V_D < (V_G - V_T)$. If $V_D = (V_G - V_T)$, the semiconductor region near the drain contact is completely depleted of free charge carriers. Once this point is reached, the current becomes independent of V_D and it follows:

$$I_{D,sat} = \frac{W}{2L} C \mu_{sat} (V_G - V_T)^2$$

In general, the transistors are characterized either by sweeping V_D at a constant V_G (I_D - V_D) or output curve, or by sweeping V_G at constant V_D (I_D - V_G), or transfer curve. By adjusting the obtained curves in the linear or saturation regime to the previous equations, the mobilities μ_{lin} and μ_{sat} can be calculated (leading often to different values, usually with higher mobilities in the saturation regime), in addition to other important parameters such as V_T , I_{on}/I_{off} , and the subthreshold swing S (a measure of the switching speed from the on to the off state).

For a given molecular material, it is the charge carrier injection into the organic semiconducting layer and the charge carrier mobility within the organic film which mainly determine its electronic performance. The charge carrier mobility depends crucially on the intermolecular overlap of the electronic π -orbitals of the molecules, which is in turn intimately related to the crystal structure [41,46]. For an optimum electronic transport, the achievement of organic single crystalline films would be the ideal case, since the intrinsic charge carrier mobility obtained in single crystals actually represents an upper limit for the thin films. [44,47-49] In practice, the growth of TFT results in the formation of polycrystalline films, introducing charge traps at the grain boundaries, [50-53] defects [54,55] and interfaces, [56] which reduce the effective carrier mobility in the films.

The charge carrier injection depends on the energy barrier at the

semiconductor-metal interface and is strongly influenced by the structural and electronic properties of the organic films at the contacts. [37] The inherent contact resistance of a metal-semiconductor junction showing a potential barrier between the metal work function and the HOMO or LUMO level, is frequently further enhanced by additional dipole barriers generated at the interfaces. [37] In addition, in bottom contact devices the semiconductor usually shows different growth behaviours on the contacts and on the dielectric, giving rise to a large number of grain boundaries in the transition region close to the contacts. [57,58] For these reasons, it is often the case that the contact resistances in the devices are large and limit their performance. [37,59-60] Another important aspect for the device properties is the material purification, [66] since the presence of impurities can have several negative effects on the device, as e.g. generating traps or increasing the semiconductor conductivity with dopants and thereby reducing its I_{on}/I_{off} ratio [38,55]

The challenge is to find a route to optimize the parameters of influence, i.e., increase the domain sizes, [67,68] obtain structures of upright standing molecules in order to have the overlap of π -orbitals and thus the favoured direction of charge carrier transport in the surface plane, [41,37,48] obtain highly aligned films, [42,54] decrease defects or other charge carrier traps, or improve the charge injection. There is a number of accessible tools which have been explored to reach each of these goals.

For the optimization of the charge carrier mobility within the organic film, special attention has to be paid to the first layers in proximity to the dielectric, since it is already well established that the charge transfer takes place mainly along these very first layers of the semiconductor close to the dielectric interface. [34d,58,69]

Among the oligothiophenes, the shorter homologue of sexithiophene (T6), quinquethiophene (T5), has been much less studied. T5 is more difficult to synthesize than T6, but has the advantage of being slightly soluble in a few organic solvents which makes it easier to purify. At the same time, solubility offers the possibility of processing thin films by solution deposition or casting, which are more relevant in view of large area applications.

Scarce data from different laboratories on field-effect charge mobility generally quoted between 1 and 2 orders of magnitude below that of T6 have been published. [70,71] Interestingly, experimental data obtained by a variety of structural techniques strongly suggest that T5 can self-organise into layered structures, [72] which makes it promising as an organic semiconductor with high charge carrier mobility.

Therefore, in this thesis, we have studied some general trends of variation in the electrical properties of T5 on changing film deposition conditions or introducing structural modifications of the backbone.

1.3.3 Thin Films and their importance in technology

As thin films represent instances of low dimensional solids, they arise nowadays a large interest in science and technology.

Many techniques can be used for the film deposition according to the state (liquid, powder, etc...) of material. In the case of vapour deposition for instance, one has to consider rate of deposition, temperature of vapour atoms or molecules, angle of incidence of vapours, electrostatic charges carried by vapours, the substrate and vapour materials, substrate temperature and thermal accommodation and condensation coefficients of the vapour atoms and the ambient gas atoms carrier. Thin films properties may vary from technique to technique.

1.3.4 Thin Films growth modes

Many of today solid state devices are based on thin films, consequently making their growth a subject of high technological interest. The requirements for the film structure and morphology can vary from couple of layers to multilayers with layers of well defined thicknesses and sharp interfaces. The control over the final film structures and morphologies is thus crucial for the device performance.

The theoretical background of film growth is very broad and has been studied under different approaches. Here, only a brief summary is presented, focused on those aspects necessary for a basic understanding of the growth

There are three basic scenarios that can describe the evolution of the film morphology upon film growth, as shown in Figure 5.2:

i. One layer starts forming and the next layer does not starts until the previous one is completed. This is called “layer-by-layer” or “Frank-Van der Merwe” growth.

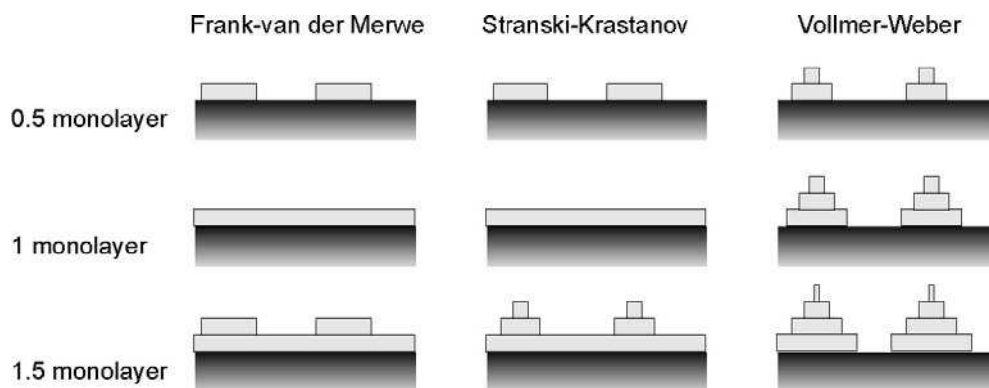


Figure 1.11 Schematic representation of the three different film growth scenarios.

ii. The deposited material assembles in islands. This is called “island” or “Vollmer-Weber” growth.

iii. Initially a layer-by-layer growth takes places, which switches to an island growth after a critical thickness. This is called “layer-plus-island” or “Stranski-Krastanov” growth.

One of the approaches to explain and predict the three different growth modes was derived by Bauer. [73] from the three macroscopic surface tensions of the involved interfaces, the overlayer-vacuum interface (γ_o), the overlayer-substrate interface (γ_i), and the substrate-vacuum interface (γ_s). If the surface tensions fulfill following condition:

$$\gamma_o + \gamma_i \leq \gamma_s \quad (1.1)$$

the system is energetically favoured if the overlayer completely covers the surface, consequently leading to a layer-by-layer growth. If this is not the case, the substrate will be only partially covered, leading to an island growth. Stranski-Krastanov growth takes place if equation (1.1) is initially fulfilled below a critical thickness, thus following a layer-by-layer growth behaviour, but only during the growth of the first layers. This growth scenario is often found in heteroepitaxial growth due to the formation of a strained overlayer. The strain accumulated in the overlayer can be considered to contribute to γ_i and shows a monotonic increase of energy with increasing film thickness. Thus, at a critical thickness an unstable situation is reached at which $\gamma_o + \gamma_i > \gamma_s$, and the system switches from layer-by-layer to island growth.

However, these considerations are only applicable in thermodynamic equilibrium, while film growth intrinsically implies being away from equilibrium. Consequently, only those systems which

are close to equilibrium, i.e. high substrate temperature and low deposition flux, can be properly described by a thermodynamic approach. To account for growth scenarios arising from systems further from equilibrium (low substrate temperatures and high deposition rates), kinetic aspects have to be considered such as adsorption, desorption, diffusion or nucleation, [74,75,76] as shown in Figure 5.2. Each of these processes has different activation barriers, and the final film morphology is determined by the hierarchy of their barriers together with the deposition rate and substrate temperature. By optimization of these two easily controllable growth parameters, the kinetic aspects can be exploited to obtain desired metastable film morphologies.

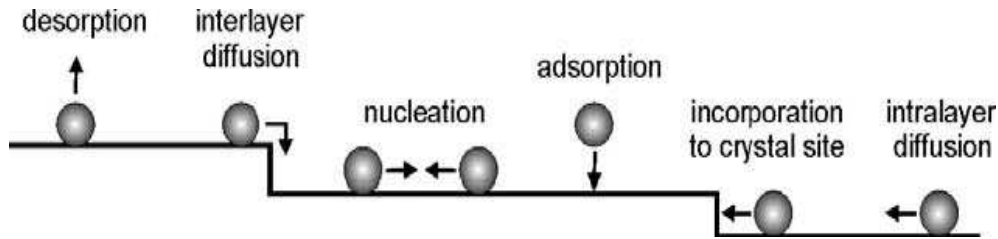


Figure 1.13. Kinetic processes occurring during film growth.

1.3.5 High vacuum deposition

Among the various film growth techniques, high vacuum deposition is widely used due to the good control it offers over the chemical purity, the atomically clean substrate and environment, film thickness, growth rate and substrate temperature. The deposition consists on holding the substrate under high-vacuum typically (10^{-6} - 10^{-8}) mbar conditions, exposed to a flow of molecules in the vapour phase. The molecular flow is generated in so-called Knudsen cells, which typically consist of crucibles with a temperature sensor, surrounded by a heating filament and a thermal shielding. The material is put into the crucible and heated until sublimation takes place. The small opening of

the crucible towards the high vacuum chamber generates a rather focused molecular flow, which can be blocked by a shutter and whose flux is controlled by the crucible temperature.

1.4 Thesis overview

The aim of part of the work done in this thesis concerns the understanding of the nature of the nanostructures, the mechanism by which spatial correlations emerge and propagate across length scales in rotaxanes and the extent to which rotaxane architecture plays a specific role in the self organisation in the solid state. The other part is about the study of quinquethiophenes (unsubstituted, substituted and modified).

This thesis is organised as follows:

this chapter: a general introduction; chapter 2: the study of the Self-organisation of rotaxanes thin films into spatially correlated nanostructures; chapter 3: Thickness control of rotaxanes thin films grown by spin coating; chapter 4: the study of the viscoelastic properties of rotaxanes thin films when undergoes crystallites; chapter 5: FET device performance, morphology and X-ray thin film structure of unsubstituted and modified Quinquethiophenes; an appendix. At the end of every chapter we draw a conclusion.

References

- [1] R. P. Feynman, *Eng. Science* **23**, 22 (1960).
- [2] G. Binnig, G. C. Rohrer, E. Weibel, *Physical Review Letters*, **49**, 57 (1982).
- [3] Eigler, D. M.; Schweizer, E. K. *Nature* **344**, 524 (1990).

- [4] a) J. M. Lehn, *Angewandte Chemie International Edition* **27**, 89 (1988), (b) J. M. Lehn, *Angewandte Chemie International Edition*, **29**, 1304 (1988).
- [3] D. M. Eigler, E. K. Schweizer, *Nature* **344**, 524 (1990).
- [5] A. M. Higgins, R. A. Jones, *Nature*, **404**, 476 (2000).
- [6] S. Herminghaus, K. Jacobs, K. Mecke, J. Bischof, A. Fery, M. Ibn-Elhaj, S. Schlagowski, *Science* **282**, 916 (1998).
- [7] W. Ross Ashby, "Principles of the Self-Organizing Dynamic System", *Journal of General Psychology* **37**, 125, (1947).
- [8] L. Von Bertalanffy, *General System Theory Foundations, Development, Applications*, New York (1968).
- [9] G. Nicolis and I. Prigogine, *Self-Organization in Non-Equilibrium Systems*, Wiley, (1977).
- [10] *Challenges in the physics of photons, atoms, molecules and Matter* FOM-06. 0875.
- [11] J. M. Lehn, *Science* **29**, 2400, (2002).
- [12] General review of self assembly: (a) J-M. Lehn, *Angew. Chem.* **100**, 1347 (1990); (b) G. Whitesides, J. P. Mathias , C. T. Seto, *Science*, **254**, 1312 (1991); G. M. whitesides, *Sci. Am.* **273**, 146 (1995).
- [13] *Molecular Catenanes, Rotaxanes and Knots: A Journey Through the World of Molecular Topology*; J-P Sauvage, C. D. Buchecker, Eds. Wiley-VCH, Germany, (1999).
- [14] (a) V. Balzani, A.Credi, F. M. Raymo, J. F. Stoddart, *Angew. Chem., Int. Ed.*, **39**, 3348. (2000) (b) V. Balzani, M. Venturi, A. Credi, *Molecular Devices and Machines - A Journey into the Nanoworld*; Wiley-VCH: Weinheim, (2003). (c) A. H. Flood, R. J. A. Ramirez, W.-Q. Deng, R. P Muller, W. A.Goddard, J. F. Stoddart, *Aust. J. Chem.* **57**, 301 (2004), (d) E. R. Kay, D. A. Leigh, *Synthetic Molecular Machines in Functional Artificial Receptors*; T. Schrader, A. D.

Hamilton, Eds. Wiley-VCH: Weinheim, Germany, (2005).

- [15] F. G. Gatti, D. A Leigh, S. A. Nepogodiev, A. M. Z. Slawin, S. J. Teat, J. K Wong, Y. *J. Am. Chem. Soc.*, **123**, 5983 (2001).
- [16] Perez, E. M.; Dryden, D. T. F.; Leigh, D. A. Teobaldi, G. Zerbetto, F. *J. Am. Chem. Soc.*, **126**, 12210, (2004).
- [17] C. P. Collier, E. W. Wong, M. Belohradsky, F. M Raymo, J. F. Stoddart, P. J. Kuekes, R. S. Williams, J. R Heath. *Science* **285**, 391 (1999).
- [18] G. Bottari, D. A. Leigh, E. M. Pérez, *J. Am. Chem. Soc.*, **125**, 13360 (2003).
- [19] (a) Q.-C. Wang, D.-H Qu., J. Ren, K. Chen, H. Tian, *Angew. Chem., Int. Ed.* **2004**, *43*, 2661-2665. (b) D.-H. Q.-C. Qu, J. Wang, H. Ren Tian, *Org. Lett.*, **6**, 2085 (2004). (c) D. A. Leigh, et al. *Angew. Chem., Int. Ed.* **44**, 3062. (2005).
- [20] (a) A. H. Flood, A. J. Peters, S. A. Vignon, D. W. Steuerman, H.-R. Tseng, S. Kang, J. R Heath, J. F Stoddart, *Chem. Eur. J.*, **10**, 6558, (2004). (b) D. W. Steuerman, H.-R. Tseng, A. J Peters, A. H. Flood, J. O Jeppesen, K. A. Nielsen J. F Stoddart, J. R Heath, *Angew. Chem., Int. Ed.* **43**, 6486 (2004).
- [21] (a) E. Katz, O. Lioubashevsky, I. Willner, *J. Am. Chem. Soc.*, **126**, 15520, (2004). (b) B. Long, K. Nikitin, D. Fitzmaurice, *J. Am. Chem. Soc.* **125**, 15490, (2003). (c) E. Katz, I. Sheeney Haj, I. Willner, *Angew. Chem., Int. Ed.* **43**, 3292, (2004). (d) T. J. Huang et al. *Nano Lett.* **4**, 2065 (2004) (e) H.-R Tseng, D. Wu, N. X. Fang, X. Zhang, J. F. Stoddart, *Chem. Phys. Chem.*, **5**, 111 (2004). (f) S. S. Jang et al. *J. Am. Chem. Soc.* **127**, 1563 (2005). (g) R. Hernandez, H.-R Tseng, J. W Wong, J. F. Stoddart, J. I Zink, *J. Am. Chem. Soc.*, **126**, 3370 (2004). (h) Y. Liu et al. *J. Am. Chem. Soc.*, **127**, 9745 (2005).
- [22] A. H. Flood, J. F. Stoddart, D. W. Steuerman, J. R. Heath, *Science* **306**, 2055 (2004).
- [23] M. Feng, X. Guo, X. Lin, X. He, X. Ji, W. Du, D. Zhang, D. Zhu, H. J. Gao, *Am. Chem. Soc.* **127**, 15338. (2005).

- [24] F. Biscarini, M. Cavallini, D. A. Leigh, S. Leon, S. J. Teat, J. K. Y Wong, F Zerbetto, *J. Am. Chem. Soc.*, **124**, 225 (2002).
- [25] M. Cavallini, F. Biscarini, S. Leon, F Zerbetto, G. Bottari D. A. Leigh, *Science*, **299**, 531 (2003).
- [26] F. Biscarini, M. Cavallini, R. Kshirsagar, G. Bottari, D. A. Leigh, S. León and F. Zerbetto, *Proc. Natl Acad. Sci. USA* **103**, 17650 (2006).
- [27] (a) M. Sferrazza, M. Heppenstall-Butler, R. Cubitt, D. Bucknall, J. Webster, R. A. L. Jones, *Phys. Rev. Lett.* **81**, 5173. (1998). (b) S. Herminghaus, K. Jacobs, K. Mecke, J. Bischof, A. Fery, M. Ibn-Elhaj, S. Schlagowski, *Science* **282**, 916, (1998). (c) K. Y Suh, H. H. Lee, *Phys. Rev. Lett.* **87**, 135502 (2001). (d) K. Kargupta, A. Sharma, *J. Chem. Phys.* **116**, 3042 2002. (e) R. Seemann, S. Herminghaus, K. Jacobs, *J. Phys.: Condens. Matter*, **13**, 4925 (2001). (f) R. Seemann, S. Herminghaus, K. Jacobs, *Phys. Rev. Lett.*, **86**, 5534 (2001).
- [28] (a) P. Ostoja, P. Maccagnani, M. Gazzano, M. Cavallini, J. C. Kengne, R. Kshirsagar, F. Biscarini, M. Melucci, M. Zambianchi and G. Barbarella, *Synt. Met.* **146**, 243 (2004). (b) Manuela Melucci, M. Gazzano, G. Barbarella, M. Cavallini, F. Biscarini, P. Maccagnani, and P. Ostoja, *J. Am. Chem. Soc.* **125**, 10266 (2003).
- [29] C. D. Dimitrakopoulos, P. R. L. Malenfant, *Adv. Mater.* **14**, 99. (2002).
- [30] H. Sirringhaus *Adv. Mater.* **17**, 2411 (2005).
- [31] A. Köler, J. S. R. Wilson, H. Friend, *Adv. Mater.* **14**, 701. (2002).
- [32] H. Hoppe, N. S. Sariciftci, *J. Mater. Res.* **19**, 1924. (2004).
- [33] (a) A. Brillante, I. Bilotti RG. Della Valle, E. Venuti, M. Masino, A. Girlando *Adv. Mat.* **17** 2549 (2005). (b) A. Brillante I. Bigotti, F. Biscarini, R.G. Della Valle, E. Venuti *Chem. Phy.* **328**, 125 (2006).
- [34] (a) F. Biscarini, R. Zamboni, P. Samori, P. Ostoja, C. Taliani, *Phys. Rev. B* **52**, 1995. (b) J. -F Moulin, F Dinelli, M Massi, C Albonetti, R Kshirsagar, F Biscarini. *Nuclear Instruments & Methods in Physics Research section b-*

- Beam Interactions with Materials and Atoms* **246**,122, (2006). (C) F. Dinelli, M. Murgia, F. Biscarini, D. M. De Leeuw *Synth. Met.* **146**, 373, (2004). (d) F. Dinelli, M. Murgia, P. Levy, M. Cavallini, F. Biscarini, de D.M. Leeuw. *Physical Review Letters* **92**, 116802 (2004). (e) G. G. Malliaras, R. Friend, *Phys. Today* **58**, 53 (2005).
- [35] A. Tsumura, K. Koezuka, T. Ando, *Appl. Phys. Lett.* **48**, 1210 (1986).
- [36] G. Horowitz, D. Fichou, X. Z. Peng, Z. G. Xu, F. Garnier, *Sol. State Commun.* **72**, 381 (1989).
- [37] C. R. Newman, C. D. Frisbie, D. A. da Silva Filho, J.- L. Brédas, P. C. Ewbank, K. R. Mann, *Chem. Mater.* **16**, 4436 (2004).
- [38] G. Horowitz, *J. Mater. Res.* **19**, 1946 (2004).
- [39] D. A. Neamen, *Semiconductor physics and devices: basic principles*, Irwin, Ed. Chicago (1996).
- [40] S. M. Sze, *Physics of semiconductor devices*, Wiley and Son, New York (1981).
- [41] F Garnier, A. Yassar, R. Hajlaoui, G. Horowitz, F. Deloffre, B. Servet, S. Ries, P. Alnot, *J. Am. Chem. Soc.*, **115**, , 8716 (1993).
- [42] N. Karl, *Synth. Met.*, **133**, 649 (2003).
- [43] V. C. Sundar, J. Zaumseil, V. Podzorov, E. Menard, R. L. Willet, T. Someya, M. E. Gershenson, J. A. Rogers, *Science* **303**, 1644 (2004).
- [44] M. E. Gershenson, V. Podzorov, A. F. Morpurgo, *Rev. Mod. Phys.* **78**, 973 (2006).
- [45] C. D. Dimitrakopoulos, A. R. Brown, A. Pomp, *J. Appl. Phys.* **80**, 2501 (1996).
- [46] T. Heim, K. Lmimouni, D. Vuillaume, *Nanolett.* **4**, 2145 (2004).

- [47] R. W. I. De Boer, M. E. Gershenson, A. F. Morpurgo, V. Podzorov, *Phys. Stat. Sol. (a)* **201**, 1302 (2004).
- [48] H. E. Katz, C. Klov, V. sundar, J. Zaumseil, A. L. Briseno, *J. Mater. Res.* **19**, 1995 (2004).
- [49] J. Niemax, A. K. Tripathi, J. Pflaum, *Appl. Phys. Lett.* **86**, 122105 (2005).
- [50] T. W. Kelley, C. D. Frisbie, *J. Phys. Chem. B* **105**, 4538 (2001).
- [51] A. B. Chwang, C. D. Frisbie, *J. Appl. Phys.* **90**, 1342 (2001).
- [52] T. Hassenkam, D. R. Greeve, T. Bjornholm, *Adv. Mater.* **13**, 631 (2001).
- [53] T. W. Kelley, E. L. Granstrom, C. D. Frisbie, *Adv. Mater.* **3**, 261 (1999).
- [54] N. Karl, K.-H. Kraft, J. Marktanner, M. Münch, F. Schatz, R. Stehle, H.-M. Uhde, *J. Vac. Sci. Tech. A* **17**, 2318 (1999).
- [55] N. Karl, *Chem. Scr.* **17**, 201 (1981).
- [56] J. Veres, S. Ogier, G. Lloyd, D. de Leeuw, *Chem. Mater.* **16**, 4543 (2004).
- [57] I. Kymissis, C. D. Dimitrakopoulos, S. Purushothaman, *IEEE Trans. Elec. Dev.* **48**, 1060 (2001).
- [58] T. Muck, J. Fritz, V. Wagner, *Appl. Phys. Lett.* **86**, 232101 (2005).
- [59] G. B. Blanchet, C. R. Fincher, M. Lefenfeld, *Appl. Phys. Lett.* **84**, 296 (2004).
- [60] K. P. Puntambekar, P. V. Pesavento, C. D. Frisbie, *Appl. Phys. Lett.* **83**, 5539 (2003).
- [61] K. Seshadri, C. D. Frisbie, *Appl. Phys. Lett.* **78**, 993 (2001).
- [62] J. A. Nichols, D. J. Gundlach, T. N. Jackson, *Appl. Phys. Lett.* **83**, 2366 (2003).

- [63] L. Bürgi, T. J. Richards, R. H. Friend, H. Sirringhaus, *J. Appl. Phys.* **94**, 6129 (2003).
- [64] R. A. Street, A. Salleo, *Appl. Phys. Lett.* **81**, 2887 (2002).
- [65] K. Müller, A. Goryachko, Y. Burkov, C. Schwiertz, M. Ratzke, J. Köble, J. Reif, D. Schmeisser, *Synth. Met.* **146**, 377 (2004).
- [66] S. R. Forrest, *Nature* **428**, 911 (2004).
- [67] D. G. de Oteyza, E. Barrena, J. O. Ossó, H. Dosch, S. Meyer, J. Pflaum, *Appl. Phys. Lett.* **87**, 183504 (2005).
- [68] G. Horowitz, M. E. Hajlaoui, *Synth. Met.* **122**, 185 (2001).
- [69] R. Ruiz, A. Papadimitratos, A. C. Mayer, G. G. Malliaras, *Adv. Mater.* **17**, 1795 (2005).
- [70] G. Barbarella, M. Zambianchi, M. Marimon del Fresno, Antolini, L.; Bongini, A. *Adv. Mater.*, **9**, 484 (1997).
- [71] X. M. Hong, H. E. Katz, A. J. Lovinger, B. C. Wang, K. Raghavachari, *Chem. Mater.*, **13**, 4686 (2001).
- [72] (a) E. Muller, C. Ziegler, *J. Mater. Chem.* **10**, 47 (2000). (b) O. Pellegrino, M. R. Vilar, G. Horowitz, F. Kouki, F. Garnier, J. D. L. da Silva, A. M. B. doRego, *Thin Solid Films*, **327**, 252 (1998). (c) Kramer, M.; Hoffmann, V. *Opt. Mater.* **9**, 65 (1998). (d) A. J. Pal, R. Osterbacka, K. M. Kallman, H. Stubb, *Appl. Phys. Lett.* **71**, 228 (1997). (e) S. Isz, I. Weissbuch, K. Kjaer, W. G. Bouwman, J. Als-Nielsen, S. Palacin, A. Ruaudel-Teixier, L. Leiserowitz, M. Lahav, *Chem. Eur. J.* **3**, 930. (1997).
- [73] D. G. de Oteyza Ph. D. thesis (2006).
- [74] A. Pimpinelli, J. Villain, *Physics of crystal growth*, Cambridge University Press, Cambridge (1999).
- [75] Z. Zhang, M. G. Lagally, *Science* **276**, 377 (1997).

[76] J. A. Venables, G. D. T. Spiller, M. Hanbücken, *Rep. Prog. Phys.* **47**, 399 (1984).

Chapter 2

Self-Organisation of Rotaxane Thin Films into Spatially Correlated Nanostructures.

2.1 Introduction

In this chapter we investigate the transformation of thin films of rotaxanes shown in Figure 2.1 cast onto carbon surfaces (highly oriented pyrolytic graphite and amorphous carbon). The transformation of the thin film is induced either by heating the samples (below their melting temperature, viz 345°C for rotaxane **1** and 360°C for rotaxane **2**) and by solvent annealing. The evolution vs time of annealing is studied by atomic force microscopy (AFM). The first rotaxane exhibits more interesting nanostructures than the second, which were investigated by bright field transmission electron microscopy (TEM), and selected area electron diffraction (SAED). [1].

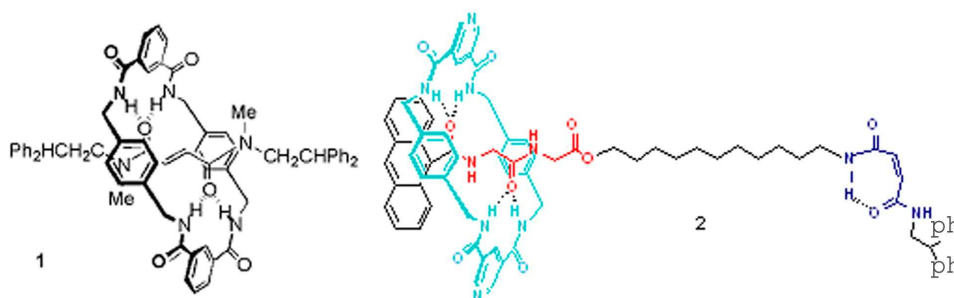


Figure 2.1. Structure of the Rotaxane **1** (left) rotaxane **2** (right)

This chapter is organized as follows: the details of the experiments are given at the “Experimental and methods” section; in the “Results section”, we describe first the morphological and structural evolution of the film upon annealing, into nanostructures and crystals, and present also the results of molecular mechanics simulations of rotaxane **1**

crystallites on the energetic of interconversion from a variety of surfaces to the minimum energy ones. The chapter is end by a “discussion and conclusion” section.

2.2 Experimental and methods.

2.2.1 Materials and thin films.

Thin films of Rotaxane **1** [2] and **2** [3] were used. For comparison, thin films of the thread or macrocycle alone were also made but they did not give similar results. Thin films at different thicknesses ranging from 3 to 35 nm were spin cast onto different substrates: freshly cleaved highly oriented pyrolytic graphite (HOPG ZYH Grade, NT-MDT, Moscow, Russia) and amorphous carbon films prepared by vacuum sputtering onto freshly cleaved mica, and native silicon (for rotaxane **2** only). On all type of substrates at room temperature, the thin films were deposited by spin casting (1500 rpm) of a rotaxane **1** solution in acetone 0,5g/l or a rotaxane **2** solutions in dichloromethane, dimethylformamide, ethanol and acetone in a concentration of 0,5g/l. All solvents were of spectroscopic grade by Aldrich.

The solution was dispensed as a few droplets on graphite substrate whose surface was normalized to 25 mm² area. The samples were then annealed in a thermostatic oven in air at progressively longer times. The annealing temperature was 90 °C for the rotaxane **1** and 90, 120 and 160°C for rotaxane **2**, so to be considerably lower than the melting temperature of rotaxane powder. These temperatures were chosen because they set a suitable timescale for the AFM experiments. At the end of each time interval, the sample was removed from the thermal bath, brought to room temperature (RT), and observed by a microscopy technique. The morphology of the samples remained unchanged for a period of several months.

2.2.2 TEM /SAED experiments

The annealed films of rotaxane **1** were transferred to copper electron microscopy grids (200 mesh). In the case of samples deposited on amorphous carbon this transfer was readily performed by a flotation technique [4]. In the case of samples made on HOPG a more indirect method was used to peel off the organic thin film from its substrate too thick to be transparent to electrons. We therefore evaporated a thin layer of amorphous carbon on top of the film, put small drops of polyacrylic acid solution (25 % in water, Aldrich) on the zones we wanted to transfer and then peeled off these patches after drying 3-4 hours at room temperature. The polyacrylic acid patches were subsequently put upside down on a distilled water surface and left to dissolve. After about 4 hours the self standing carbon film holding crystals of rotaxane **1** stripped from the original HOPG substrate were then picked up on the copper TEM grids. The samples were observed by bright field electron microscopy and electron diffraction using a Philips CM12 TEM (courtesy of CNRS ICS Strasbourg) fitted with a LaB6 filament and equipped of a CCD camera (Megaview III from Soft Imaging System). The accelerating voltage was 120 kV and, in order to minimize the beam damage, we used the low dose mode of the microscope together with small C2 aperture (30 micron) and low current (spot 8-9 setting). The selected area electron diffraction patterns were recorded at a 2.50 m chamber length using a 10 micron selecting aperture. The experiments were carried out at room temperature.

2.2.3 Morphology characterisation

We used an AFM Autoprobe CP Research Park scientific instrument at ambient conditions to investigate the morphology of the samples prepared on HOPG, and in one case of the sample stripped with amorphous carbon. AFM revealed that

films were 5-15 nm thick. AFM scans were performed on the same area on samples annealed for different times, so that the local transformation of the thin film could be monitored always in the same region. Images were analyzed using autocorrelation software with the program NIH-Image (NIH, Bethesda, MD).

2.2.4 Modelling

MM3 model [5] was used to calculate structure and energy of surfaces of rotaxane **1**. The force field was developed by fitting both heats of formation and structural parameters in the gas phase and in crystals. All the calculations reported here were performed using the TINKER package. [6] The surface geometries of the rotaxane **1** were optimized starting from the crystal structure determined by X-ray diffraction data.

2.3 Results

2.3.1 Thermal annealing of rotaxane **1**

Figure 2.2 shows the evolution of a thin film of rotaxane **1** upon heating the sample at 90°C. The sequence of images shows the occurrence of a three-step transformation: (i) the continuous film dewets into an ensemble of hemispherically capped droplets; [7] (ii) droplet size grows in time by ripening [7d,8] and a characteristic length scale emerges as outcome of spatial correlations; [9] (iii) at a later stage, some droplets transform into crystallites which then grow by depleting droplets from the surrounding region. At this later stage, there is no longer a characteristic length scale. Thus, the crystallization wipes out the spatial correlations established earlier. The spatial correlations are described by means of the height-height correlation function, $g(r) = \langle (h(r) - h(0))^2 \rangle$. [9] Here, $h(r)$ is the topography height for the radial distance r , and the average is performed on the azimuthal coordinate. [10] In Figure 2.3, $g(r)$ is plotted vs r for the image sequence shown in

Figure 2.2. The curves at earlier times exhibit a first local maximum at non zero length scales, and other maxima, damped in intensity, are observed at integer multiple length scales.

The position of the first maximum defines the characteristic length scale, viz. correlation length, whose evolution vs annealing time is shown in the inset of Figure 2.2.

It is clear that the characteristic length scale (ξ) increases linearly in time as a result of the size/distance increase of the droplets and then it saturates. In the monotonically growing regime, the increasing intensity of the maximum peaks reflects the enhancement of spatial correlations in time. Saturation of the characteristic length scale, ξ corresponds to the onset of crystallization via a massive ripening and disappearance of the droplets in the surroundings of the growing crystallite. The corresponding $g(r)$ shows an abrupt decrease of the intensity of the peaks, as the mosaic of droplets disappears in favour of the crystallites growth.

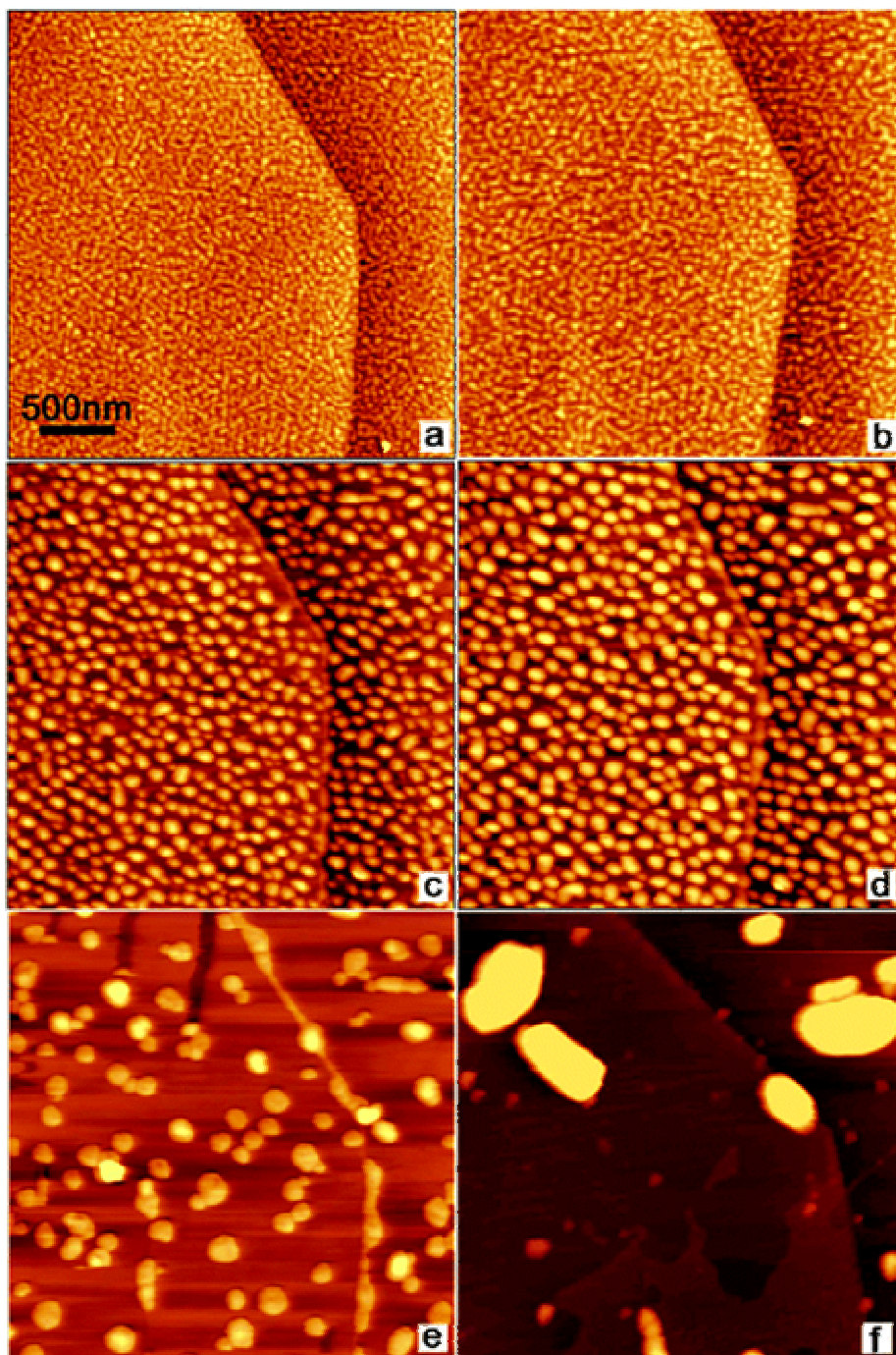


Figure 2.2 Evolution of local morphology for a rotaxane thin film spin-casted at room temperature and then annealed at 90°C for a time t : (a) $t = 0$ min, height range (black to white) $z = 8$ nm; (b) $t = 2$ min, $z = 6$ nm; (c) $t = 10$ min, $z = 10$ nm; (d) $t = 15$ min, $z = 12$ nm; (e) $t = 20$ min, $z = 12$ nm; (f) $t = 90$ min, $z = 32$ nm.

In Figure 2.4, depletion/incorporation the processes of nucleation and crystallisation via of the droplets from the area surrounding the nucleus are shown. The growing crystal exhibits the following features: (i) it nucleates 3D since the early stages, as apparent from the profile (Figure 2.4f) where the lowest layer is 5-6 nm high; (ii) edges and corners become sharper and better defined in time; (iii) the crystal exhibits a layered structure with steps 1.5 ± 0.3 nm high. This value is consistent with the interlayer spacing along the **b** direction reported for rotaxane **1** crystal (1.39 nm). [11]

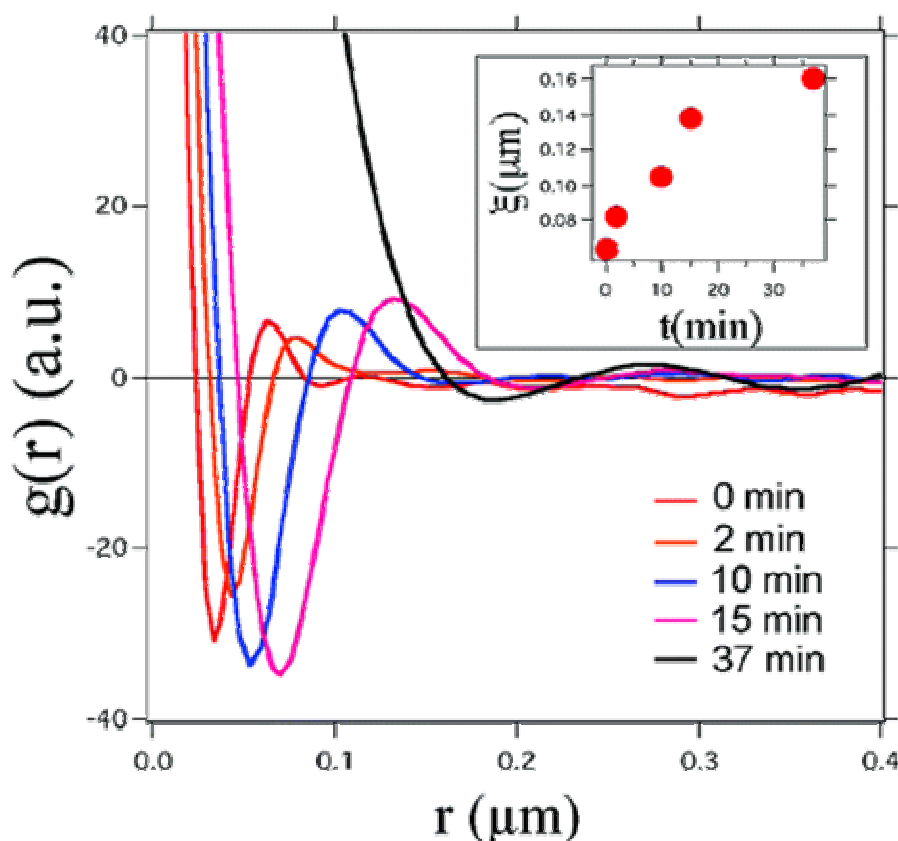


Figure 2.3. Evolution of the height-height correlation function extracted from the AFM images in Figure 2, showing both the increase and the shift in spatial correlations (height and position of the first maximum). Inset shows the evolution of the correlation length, viz. the position of the first maximum.

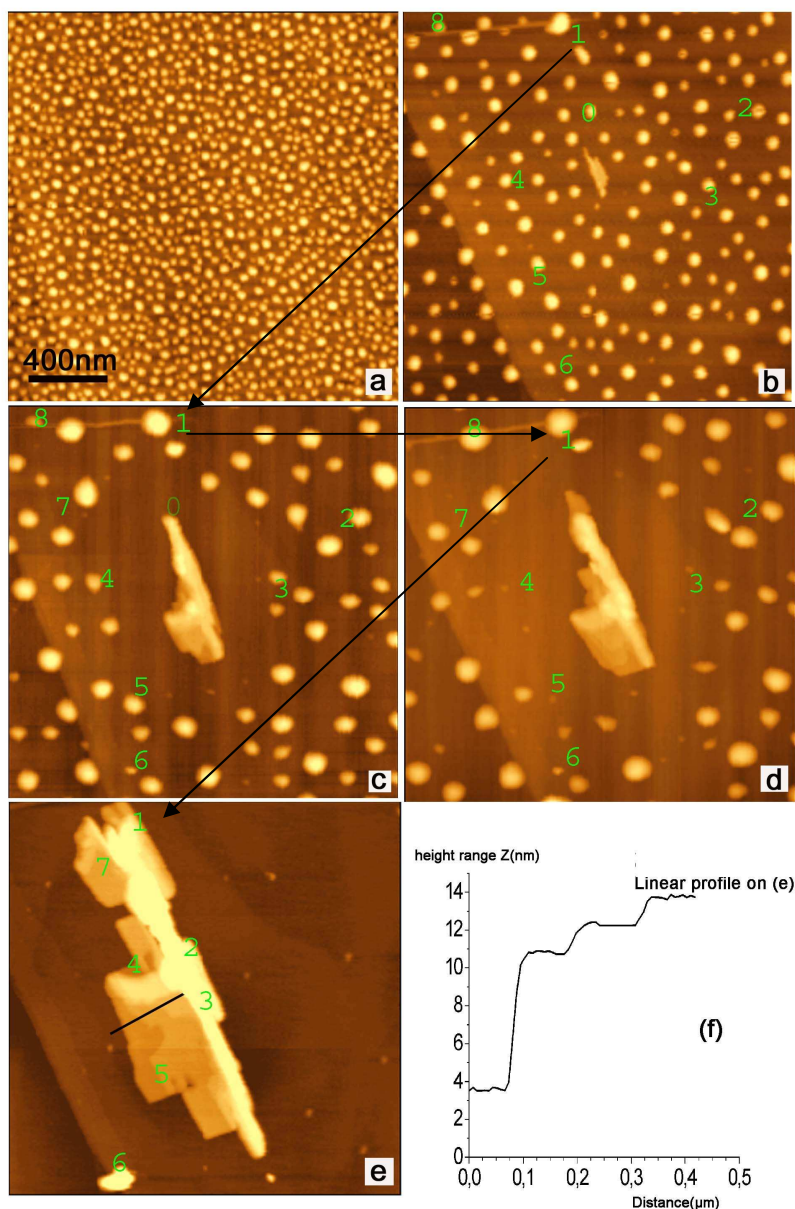


Figure 2.4. The rotaxane **1** thin film is annealed at 90°C for 20 min. After formation of the first nucleus (Figure 1.4b), the crystal grows by capturing the smaller droplets from the surroundings. Following the numbers, we can understand better the evolution of single nanodots until the recrystallisation (e.g. following the arrows to see the evolution of dot 1). The figures show the evolution at annealing time intervals $\Delta t = 5$ min: (a) the film as spin-casted at room temperature before annealing $t = 0$, height range $z = 12$ nm; (b) $t = 5$ min, $z = 18$ nm; (c) $t = 10$ min, $z = 18$ nm; (d) $t = 15$ min, $z = 19$ nm; (e) $t = 20$ min, $z = 20$ nm; (f) profile across the black line in (e).

The larger spread, viz. 10° , then largely arises from the finite width of the rotaxane **1** crystals. The underlying graphite substrate orients the growth of the rotaxane crystallites. The texturing is largely the result of the preferential nucleation of

the crystallites and the larger molecular diffusivity along terraces and steps of HOPG. Whether epitaxy, in terms of commensuration between rotaxane and graphite lattices, is relevant will be addressed in the following subsection.

2.3.2 Thermal annealing of rotaxane 2

The transformation of the thin film is induced by heating the samples at 90 °C. The evolution vs time of annealing is studied by AFM as we did with rotaxane 1, but the results (Figure 2.5) show that there is no transformation, the temperature seems to be very low to induce any transformation. The initial film with holes conserves his morphology with the annealing time and we couldn't obtain crystals. Thus, we decided to increase the heating temperature.

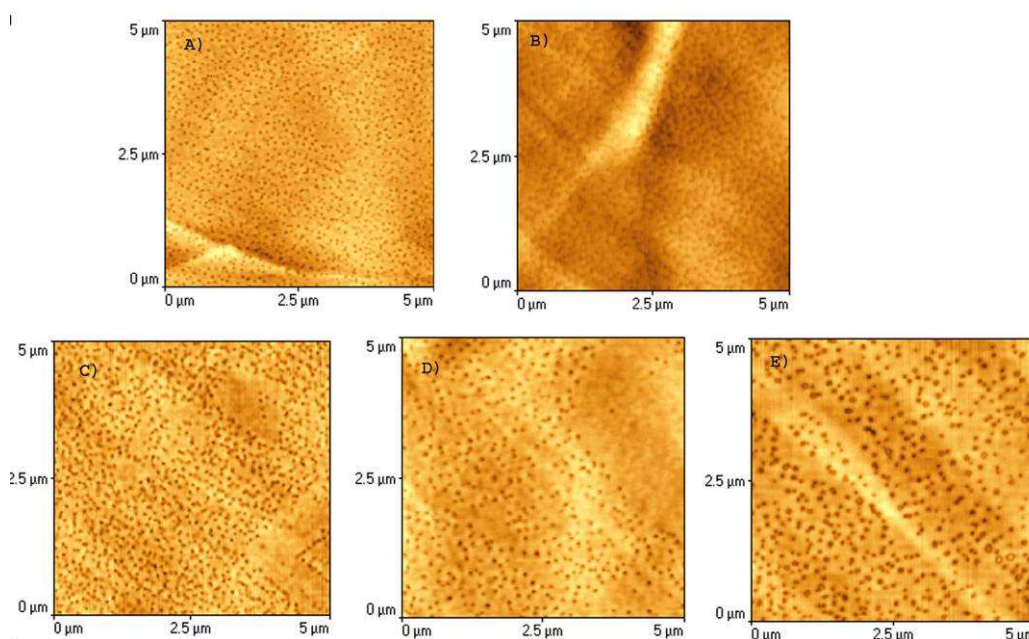


Figure 2.5 Evolution in morphology of the rotaxane 2 thin film annealed at 90°C respectively at A) 0 min; B) 5 min; C)10 min; D)15 min; E) 20 min. The samples were prepared from an ethanol solution .

We have increased the heating temperature at 120°C in next experiment. The Figure 2.6 shows the evolution in morphologies of films. The initial film present holes, after respectively 5 min, 10 min and 60 min time annealing, can

observed a small increase of holes but we have not get crystals like those of rotaxane **1**. Since we haven't observed a considerable transformation from ethanol solution on HOPG, we have thought to change the solvent and/or substrate. We have prepared samples from N,N-dimethylformamide on HOPG as shown in Figure 5.7. The results are films thick about one monolayer without change upon annealing at 160°C in 90min.

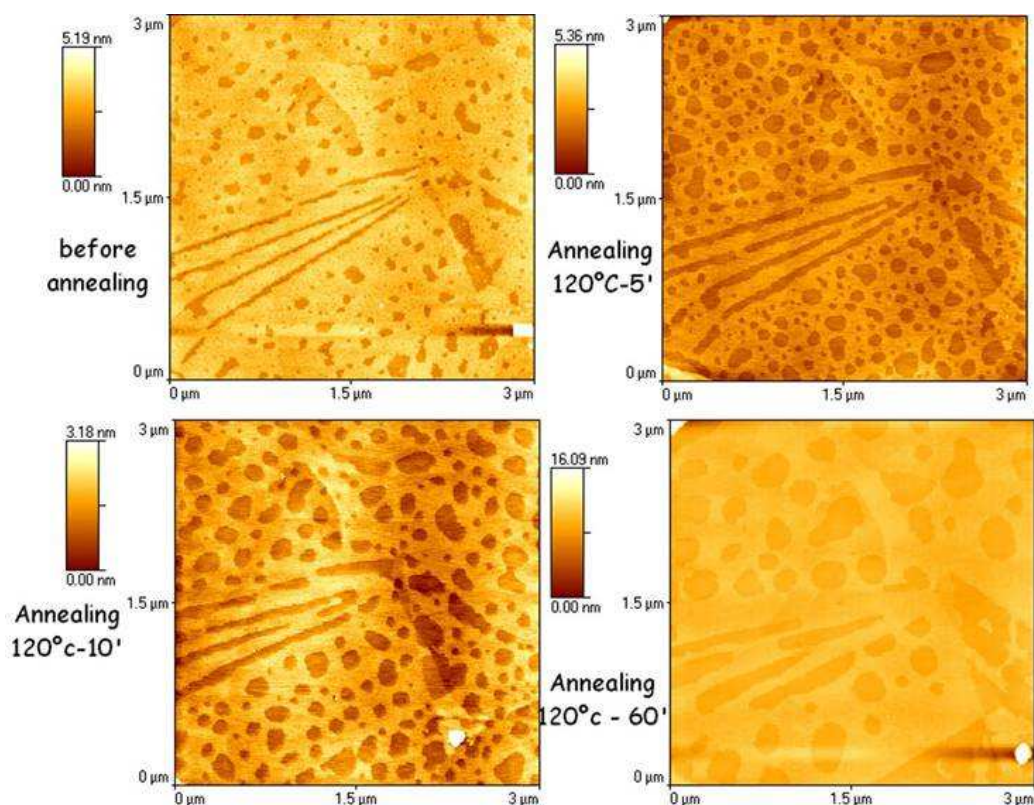


Figure 2.6 AFM images of rotaxane **2** thin films annealed at 120°C respectively at 0 min; 5 min; 10 min; 60 min. The samples were grown from an ethanol solution The images were performed in the same area.

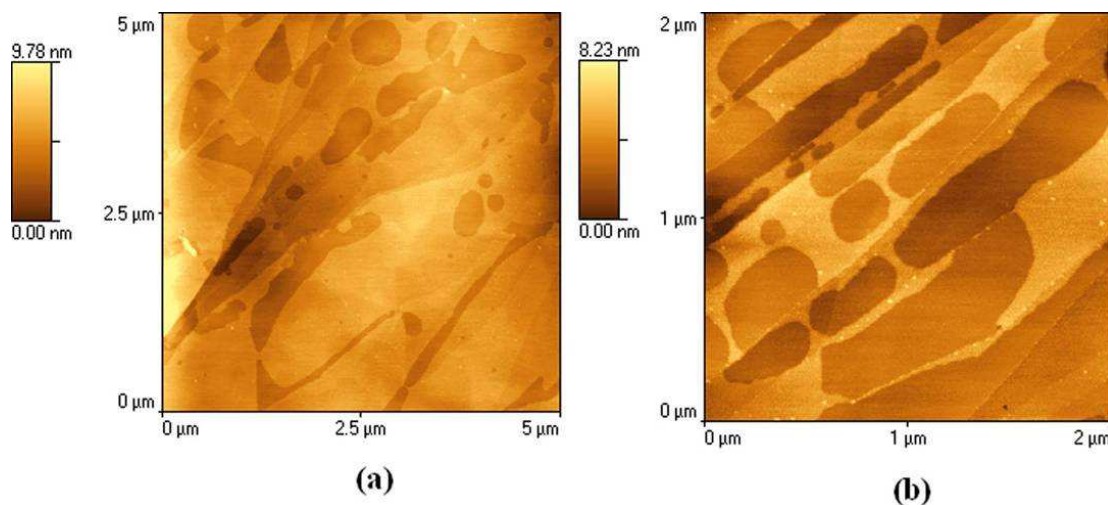


Figure 2.7. AFM images showing a monolayer of rotaxane **2** on HOPG. **a)** before annealing; **b)** after annealing at 160°C in 90 min. Films results in sublayers materials, strongly attached to the substrate.

In view of the experimental results of rotaxane **2**, it appears that the interactions of rotaxane **2** with HOPG substrate are very strong. So we check the native silicon (Si/SiO_x), a substrate technologically relevant to confirm the effect of the substrate on the recrystallisation process. We obtained only from dichloromethane a very thin film, which after 90min annealing is transformed in very correlated nanodots of about 6 nm diameter or height as shown in Figure 2.8 with a surface coverage up to 90%. The increasing of annealing time has not show further change.

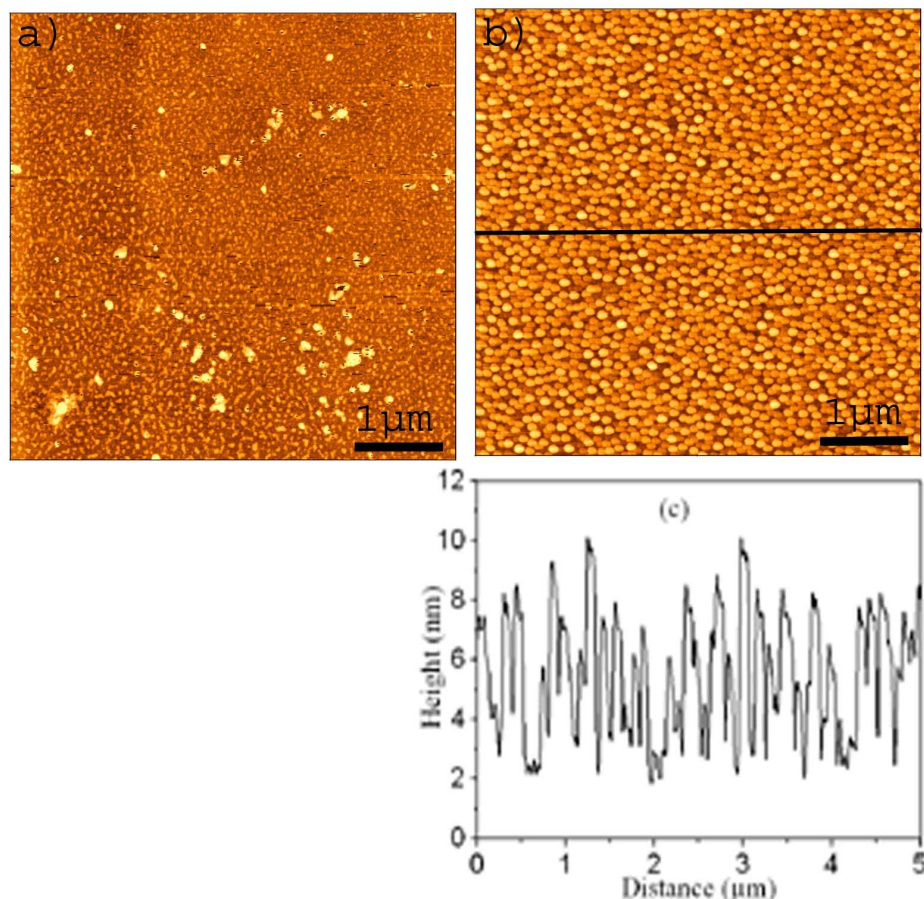


Figure 2.8 Evolution in morphology of rotaxane **2** thin film grown on Si/SiO_x substrate **a)** film at room temperature **b)** the film was annealed at 90°C in 90min and yield in very correlated nanodots of about 6 nm height as the line profile is showing in **c)**.

2.3.3 Solvent annealing of both rotaxanes

The transformation of rotaxanes thin films can be induced by exposing the film to a volatile solvent such as acetone.

The Figure 2.9 and 2.10 show the results of solvent annealing of rotaxane **1** and **2** respectively. When thin films of rotaxane **1** and **2** grown by spin coating were exposed to acetone vapours, for 24 hours rotaxane **1** showed very nice and epitaxially oriented crystals, whereas rotaxane **2** was transformed into droplets. This result confirms the strong interaction of rotaxane **2** with the substrate.

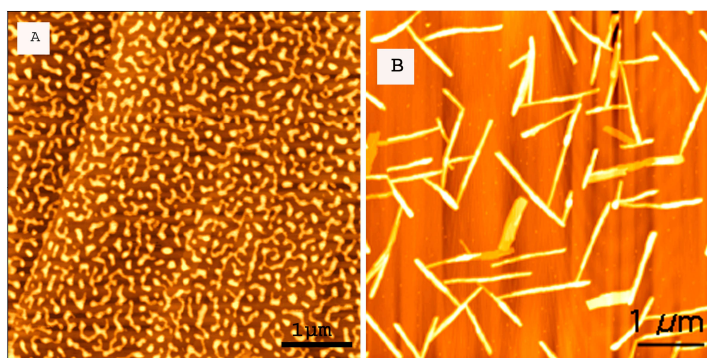


Figure 2.9 AFM images showing the results of solvent annealing of rotaxane **1** thin film on HOPG. A) film from an acetone solution, at room temperature before annealing. B) film after 24 hours under acetone vapours. The crystal morphology and texture will be presented in the following.

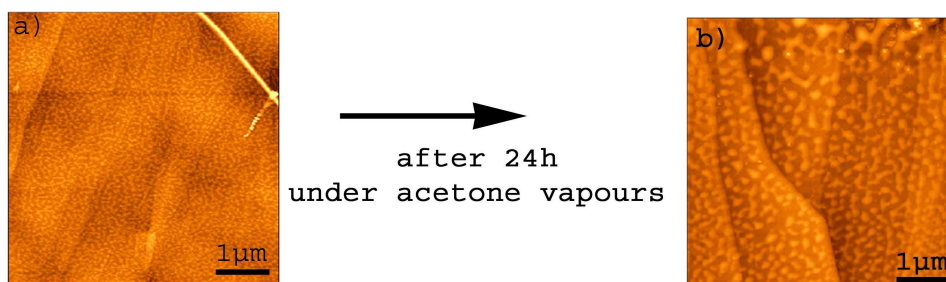


Figure 2.10 AFM images showing the evolution in morphologies of a rotaxane **2** thin film from dichloromethane (0,5g/l) on HOPG a) film at room temperature; b) after 24h under acetone vapours.

Because only rotaxane **1** yielded crystals, We have investigated crystals texturing by AFM, TEM and SAED.

2.3.4 Texturing analysis by AFM of rotaxane **1**

When crystallisation is completed, droplets have completely disappeared and a texture of crystallites on the graphite surface is formed, as shown in figure 2.11. The angular distribution of the fast growth directions of the rotaxane **1** crystal with respect to the underlying graphite lattice was measured by performing 2D-Fast Fourier Transform (FFT) on AFM images. From the 2D-FFT (inset in Figure 2.11) it appears that the main

alignment directions of the rotaxane **1** crystals form roughly 120° angles among themselves. An estimate of the angular spread in the three directions from the 2D-FFT comes out to about 10° , so the angles between the directions of in-plane orientation of rotaxane **1** crystals are $120^\circ \pm 10^\circ$. The average domain size in HOPG substrate used (grade Z) is $\sim 5\text{-}10\mu\text{m}$, which matches the typical AFM image size as in Figure 2.5. Mosaicity of HOPG used is 3.5 ± 1.5 , which sets the lower intrinsic limit on the spread of the angular distribution of rotaxane **1** crystal on HOPG

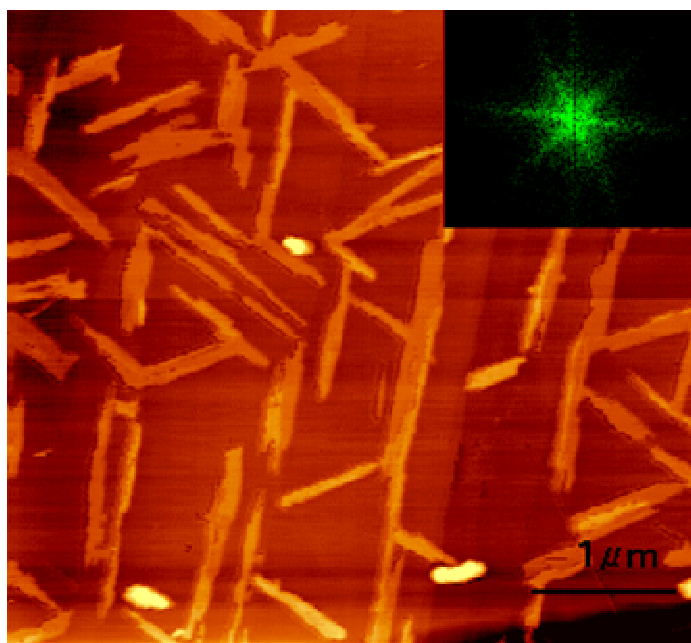


Figure 2.11. AFM image of rotaxane **1** crystallites on HOPG showing orientation along three directions. Step edges of HOPG are also visible. Inset shows 2D-FFT of the image exhibiting a 6-fold angular symmetry.

2.3.5 Structural investigation by TEM and SAED.

The annealed samples of rotaxane **1** were transferred from the graphite substrate to a copper grid coated with amorphous carbon or were prepared directly by casting and annealing on

amorphous carbon thin films for TEM investigations. Figure 2.12a shows a bright field image of **1** deposited on isotropic amorphous carbon. Large lamellae coexist together with less defined droplets, which are largely inter-connected. Large area bright field TEM images show the same type of morphologies as those observed with AFM. Upon closer examination, it appears that these smaller objects show straight edges and indeed bear similarity to the larger lamellar crystals. One should also note that it is possible to identify large domains where neighbouring objects share a common in-plane orientation. Moreover, at an initial stage of the coalescence of droplets, a pre-transitional state is observed, with droplets assuming shapes with sharp corners. The droplets give rise to a connected network which evolves into platelet crystals such as that shown in Figure 2.12b at larger magnification. The corresponding SAED pattern is shown in Figure 2.12c. The indexation was assigned on the basis of the bulk crystal structure parameters of **1**.¹⁵

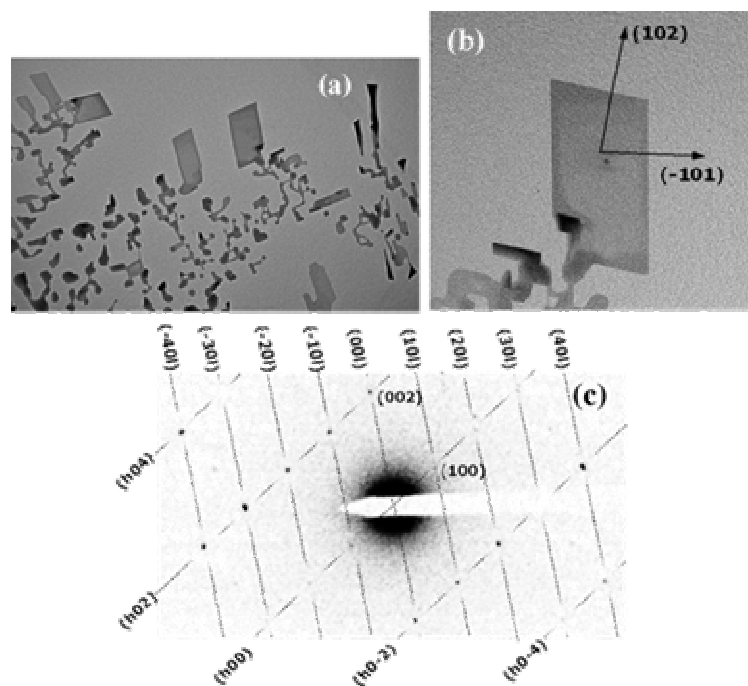
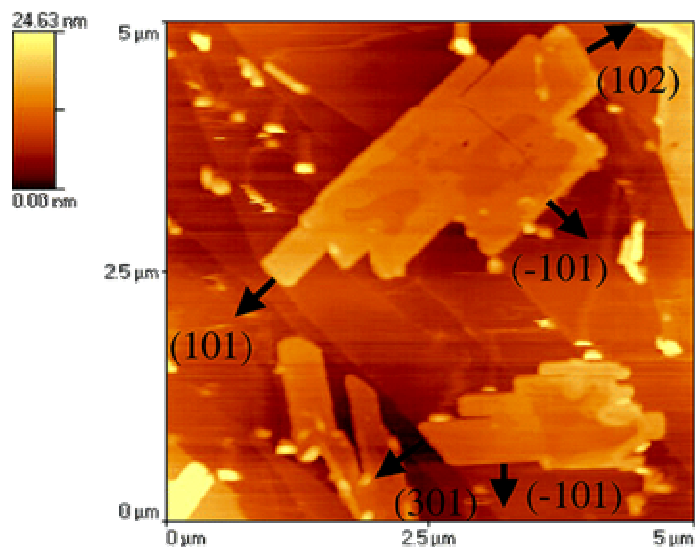


Figure 2.12 (a) Bright field image of annealed thin film of rotaxane **1** spin cast on amorphous carbon. (b) Larger magnification image of a single crystal of rotaxane

1 grown on amorphous carbon. The facets were indexed from SAED pattern (c). (c) SAED diffraction pattern of the single crystal in (b). This set of indices leads to assigning the (010) as the basal plane of the rotaxane **1** crystal.

The observed diffractions are of (h0l) type and therefore the contact plane of this platelet crystals with the substrate has been indexed as (010). The bounding facets corresponding to the fast growth directions are (102) and (-101). On HOPG, the crystal indexing has been done based on the structural results by TEM/SAED and comparison of the measurements from AFM images with the expected angles from the rotaxane **1** structure.

On HOPG, angles of 125°, 121°, and 59° were often observed in rotaxane **1** crystals. These values match the 121° angle between (301) and (-101). Thus, (-101), (102), and (301) facets are found, in some cases also (-10-1) which are expected to be at 85° from (-101). From the representative AFM image of rotaxane **1** on graphite (Figure 2.13), we infer from the aspect ratio of the crystals that (101) and (301) are faster growing facets than (-101). The (301) facets appear pinned to the graphite steps. This suggests that graphite steps either promote nucleation of this facet, and hence the crystal grows starting from there, or they stop the growth of the (301) once it reaches the edge. This relationship between crystallographic directions of rotaxane **1** crystals and graphite is sufficient to explain the orientation at 60° and 120° of the rotaxane **1** crystals as in Figure 2.13.

Figure 2.13. Indexation of rotaxane **1** crystals on HOPG

2.3.6 Energetics of rotaxane Surfaces.

In an effort to obtain further insight into the surface properties of rotaxane **1**, a computational investigation of the structures and the energy of nine surfaces characterized by low values of Miller indices were performed. Recently, both short time (sub-picosecond), harmonic, and long time (up to microsecond), large-amplitude, dynamics of this kind of systems were studied [12] with the MM3 model [13] which has become the method of choice to treat these systems. This method also reproduces rotational barriers and steric energies in cyclic and cage structures. Importantly, for the present purpose, MM3 also includes specific interatomic nonbonded potential energy functions that allow for a quantitative treatment of Van der Waals and electrostatic interactions which play an essential role in hydrogen bonding and in the π - π interactions between aromatic rings. The Figure 2.14a shows the rotaxane **1** molecular orientation in the unit cell as from the crystallographic coordinates. It's clear that, in the lamellae, the molecules of rotaxane **1** are standing with the thread almost perpendicular to the substrate. This orientation results in a contact plane made of an almost hexagonal 2D lattice of phenyl

end groups edge on the graphite surface, as shown in Figure 2.14b,c. The in-plane parameters of the **1** crystal are $a = 1.057$ nm and $c = 1.075$ nm, forming an angle $\beta = 115.25^\circ$. The results of the geometry optimization are shown in Figure 2.9 and summarized in Table 2.1. By inspection, we notice three points about the (010) surface:

i. This surface is the second most stable of the surfaces examined. The stability vouches for (010) as a possible final product of the transformations induced by an external perturbation, which can be a mechanical one (AFM tip), a thermal one or by solvent annealing.

ii. The lattice parameters of the (010) surface are within 19% misfit respect to lattice parameter of graphite. The additional role of the graphite may indeed be to further stabilize the (010) surface with respect to other minimum energy facets by epitaxy.

iii. The packing of the rotaxane in the (010) surface results in some of the strongest interaction energies between either one of the two interlocked molecules (i.e., macrocycle or thread) and the surrounding environment.

When these interactions are small, one can expect that the surface is easily modified either by a scanning AFM tip or by other external stimuli such as temperature. When these interactions are large, the molecules are strongly held in place by their neighbours. Even, if this surface is formed, it therefore appears to be more difficult to disrupt compare to other surfaces.

In short, (010) appears as the best compromise for the final product of the transformation since it forfeits a small amount of surface energy, it has large interactions of ring and dumbbell with the nearby molecules, and its lattice parameters are close to those of graphite.

Surface	γ	E_{macro}	E_{thread}	SAS	SR
100	0.0516	10.83	10.97	381.07	1.29
010	0.0910	13.21	9.19	182.53	1.78
001	0.0933	14.60	13.45	375.54	1.28
011	0.1679	8.00	4.41	582.93	1.85
101	0.1799	6.49	6.34	635.19	1.56
110	0.1607	9.64	7.07	501.60	1.59
111	0.3421	4.75	3.57	673.09	1.58
012	0.1712	8.49	7.19	637.10	1.78
210	0.1408	9.76	7.49	620.53	1.71

^a E_{macro} and E_{thread} are the sum of interactions of each of the two components of the rotaxane with the surrounding molecules. The surface accessible area, SAS ($\text{\AA}^2 \text{ cell}^{-1}$), is the size of the corrugated surface. The surface ratio, SR, is given by the SAS divided by the area of the parallelogram spawn by the lattice axes.

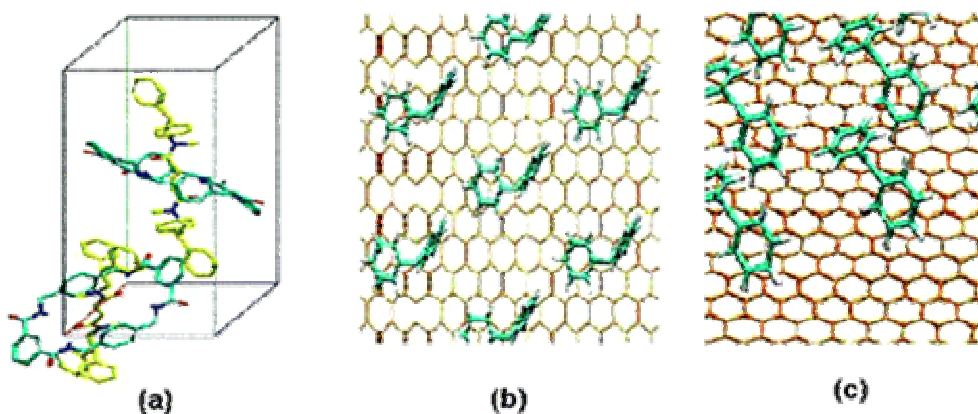


Figure 2. 14 (a) Orientation of rotaxane **1** in the unit cell; (b)-(c) contact plane of rotaxane **1** on the hexagonal 2D graphite lattice.

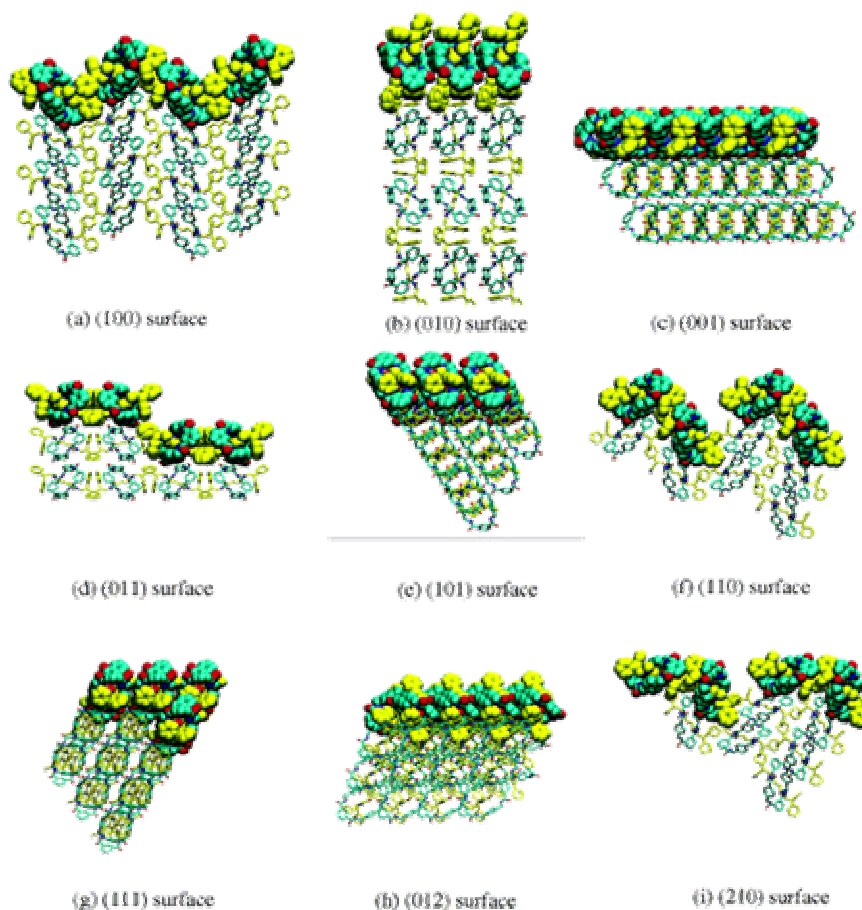


Figure 2.15 Optimised surface structures of rotaxane **1**. The thread atoms are in yellow, while the macrocycle atoms are in blue and red.

2.4 Discussion and conclusions.

The dewetting of rotaxane thin films is the first stage of a complex process leading in the steady state to the crystallization of the material. At the early stages, thermally induced dewetting or solvent annealing is the result of either nucleation and growth of holes in some instances or a spinodal mechanism in others. The droplets are formed by either one of these paths, the following evolution leads to the process described in this chapter. At a later stage some droplets nucleate into crystallites and the latter grow by incorporation of the surrounding droplets until these disappear. The coarsening or coalescence of droplets by Ostwald ripening like mechanism introduces the spatial correlations from the mesoscopic to microscopic length scales. We do not know whether these droplets undergoing ripening

are crystalline, polymorphic, or amorphous. At later stages, we observe that individual droplets undergo a restructuration at the surface and possibly internally to give rise to stable nuclei. Ripening is a universal phenomenon, observed in many different systems, from water to metals, polymers, colloids, and liquid crystals. In the case of rotaxanes, the restructuration of the individual droplets by minimum energy pathways for crystallization involves collective motion of the macrocycles with respect to the threads.

The activation energy of this small amplitude motion depends on the detailed hydrogen bond motif in the rotaxanes. Therefore, the onset of crystallization is a function of the specific rotaxanes via the energy barriers for the motions in the solid state and can be controlled by design.

On both amorphous carbon and HOPG we have observed that rotaxane **1** crystallises from solution mainly in the form of large lamellae having the same crystal structure as that of the bulk. On both substrates the contact plane of these crystals is the dense (010) plane where the terminal benzene rings (stoppers) of the thread are oriented almost normal to the surface.

The lamellae facets are indexed as very dense crystal planes and the aspect ratio is in agreement with surface energy evaluation from molecular mechanics simulation. The lamellae exhibit a common orientation over large areas. On HOPG a 3-fold symmetry of the crystals orientation reveals a strong influence of the substrate on the nucleation and diffusion.

The occurrence of epitaxy at the molecular scale cannot be either proven or ruled out here since our attempts to perform high-resolution STM on rotaxane ultrathin films and crystals did not provide conclusive evidence of the arrangement of the rotaxane molecules relative to the HOPG mesh. Also, we were not able to obtain diffraction patterns of the **1** crystals directly on their substrate since no sample was thin enough to enable electron transmission. The exact epitaxial conditions and the

relative orientation of rotaxane **1** crystals with respect to HOPG could thus not be determined. Nevertheless, it is worth noting that the 2D periodicity of the (001) plane of HOPG is very close to the one of the (010) contact plane of **1**. Although true 2D epitaxy is not realized, it is often observed that the matching of periodicity along a single direction is sufficient to lead to perfect orientation of the overgrown rotaxane layer. If epitaxy were relevant, it is worth highlighting that it does not favour the development of a new crystalline polymorph nor of a new contact plane. The bulk structure and the (010) contact plane are thus apparently the most stable ones in the conditions explored.

The transformation of rotaxanes thin films into self-organized spatially correlated nanostructures upon a thermal perturbation and solvent annealing has been investigated using atomic force microscopy, bright field transmission electron microscopy, selected area electron diffraction, and molecular mechanics simulations. The evolution follows a complex path, where the film first dewets from the substrate to form nanosized droplets whose ripening gives rise to spatially correlated motives. In a later stage, the larger droplets nucleate and coalesce into crystallites that further grow into larger crystals by incorporating the surrounding droplets. Our results show that (i) the self-organized nanostructures represent a metastable state of a crystallization process, (ii) spatial correlations emerge during ripening, but they are destroyed as stable nuclei are formed and crystallization proceeds to completion, and (iii) crystallization, either on graphite or amorphous carbon films, leads to a precise basal plane, viz. (010), which has minimum surface energy. The rotaxane architecture and the substrate favour the reorganisation and nucleation of the film in the solid state. Low-energy trajectories leading to crystallites with stable surfaces and minimum energy contact plane are found to occur

via concerted, small amplitude, internal motions without disruption of packing and intermolecular contacts.

These features combine to make rotaxanes an extremely interesting system for the investigation of self-organization across length scales, and therefore for devising new patterning strategies based on the control of spontaneous length scales.

References

- [1] L. A. Bendersky, F. W. Gayle, *J. Res. Natl. Inst. Stand. Technol.*, **106**, 997 (2001).
- [2]. F. G. Gatti, D. A Leigh, S. A. Nepogodiev, A. M. Z. Slawin, S. J. Teat, J. K. Wong, *Y. J. Am. Chem. Soc.*, **123**, 5983 (2001).
- [3] G. Bottari, D. A. Leigh, E. M. Pérez, *J. Am. Chem. Soc.*, **125**, 13360 (2003).
- [4] J. F. Moulin, M. Brinkmann, A. Thierry, J. -C. Wittmann, *Adv. Mater.*, **14**, 436 (2002).
- [5] N. L. Allinger, Y. H. Yuh, J.-H. Lii, *J. Am. Chem. Soc.* **23**, 8551 (1989).
- [6] J. W. Ponder, F. Richards, *J. Comput. Chem.*, **8**, 1016 (1987).
- [7] (a) G. Reiter, *Phys. Rev. Lett.*, **68**, 75 (1992). (b) G. Reiter, A. Sharma, *Phys. Rev. Lett.*, **87**, 166103 (2001). (c) A. Sehgal, V. Ferreiro, J. F. Douglas, E. J. Amis, A. Karim, *Langmuir*, **18**, 7041 (2002). (d) G. Reiter, R. Khanna, A. Sharma, *J. Phys. Condens. Matter.* **15**, S331 (2003).
- [8] (a) M. Zinke-Allmang, L. C. Feldman, M. H. Grabow, *Surf. Sci. Rep.*, **16**, 377 (1992). (b) G. R. Carlow, M. Zinke-Allmang, *Phys. Rev. Lett.*, **78**, 4601 (1997). (c) A. Sharma, R. Khanna, *J. Chem. Phys.*, **110**, 4929 (1999). (d) J. Singh, A. Sharma, *J. Adhes. Sci. Technol.*, **14**, 145. (2000).

- [9] M. Brinkmann, S. Graff, F. Biscarini, *Phys. Rev. B*, **66**, 165430. (2002).
- [10] Y. P. Zhao, G.-C. Wang, T.-M. Lu, *Experimental Methods in the Physical Sciences*; R. Celotta, T. Lucatorto, Eds. Academic Press: San Diego, **37** (2001).
- [11] C. P. Collier, E. W. Wong, M. Belohradsky, F. M. Raymo, J. F. Stoddart, P. J. Kuekes, R. S. Williams, J. R. Heath. *Science* **285**, 391 (1999).
- [12] M. Brinkmann, F. Biscarini, C. Taliani, I. Aiello, M. Ghedini, *Phys. Rev. B*, **61**, R16339 (2000).
- [13] (a) D. A. Leigh, A. Murphy, J. P. Smart, M. S. Deleuze, F. Zerbetto, *J. Am. Chem. Soc.* **120**, 6458 (1998), (b) M. S. Deleuze, D. A. Leigh, F. Zerbetto, *J. Am. Chem. Soc.*, **121**, 2364 (1999). (c) V. Bermudez, N. Capron, T. Gase, F. G. Gatti, F. Kajzar, D. A. Leigh, F. Zerbetto, S. W. Zhang, *Nature*, **406**, 608 (2000). (d) C.-A. Fustin, D. A. Leigh, P. Rudolf, D. Timpel, F. Zerbetto, *Chem. Phys. Chem.*, **1**, 97 (2000).

Chapter 3

Thickness control of rotaxane thin films grown by spin coating.

3.1 Introduction

In the chapter 1 we found that the transformation of a thin film into spatially correlated nanostructures of rotaxane 1 depends only on the film thickness. It is important to know the exact film thickness in order to get an accurate control of the length scale of the nanostructures obtained after the stimulus. Among several techniques for preparing thin films from solution (drop casting, dip coating, flow coating, thermal spray coating, spin coating), we chose the spin coating because it is simple and yields homogeneous films also across large areas. Research in recent years has extended the scope of spin coating by chemically engineering the interface of support and solution in order to achieve also specific structural order in the resulting thin films. The importance of spin coating is manifested by his widespread use in science and industry. The technique is used in various applications such as coating of photoresist on silicon wafers, sensors, protective coating, paint coating, optical coating, membranes, actuators and for several other applications. The most widespread use of spin coating is in microelectronics applications. The technique can lead to very uniform films of well controlled thickness.

This chapter describes the casting of rotaxane thin films and the method to access it quantitatively. [1]

3.2 Theory of spin coating

The deposition of a viscous fluid on a horizontal rotating disc produces a uniform liquid film. During deposition the disc should either be static or be rotating at a low angular velocity, whereas after the deposition of a volume of solution, the disc is rapidly accelerated to a higher angular velocity (spin speed). The adhesive forces at the liquid/substrate interface and the centrifugal forces acting on the rotating liquid result in the sheering of the liquid which causes a radial flow. In Figure 3.1 the process is illustrated.

Most of the material solution is rapidly ejected from the disc. This process combined with the subsequent evaporation of the liquid causes the thickness of the remaining liquid film to decrease. For a solution, *e.g.* a polymer solution, the evaporation process causes the solute concentration to increase and so does the viscosity at the liquid/vapor interface. After total evaporation of the solvent, an uniform solid film is obtained. [1]

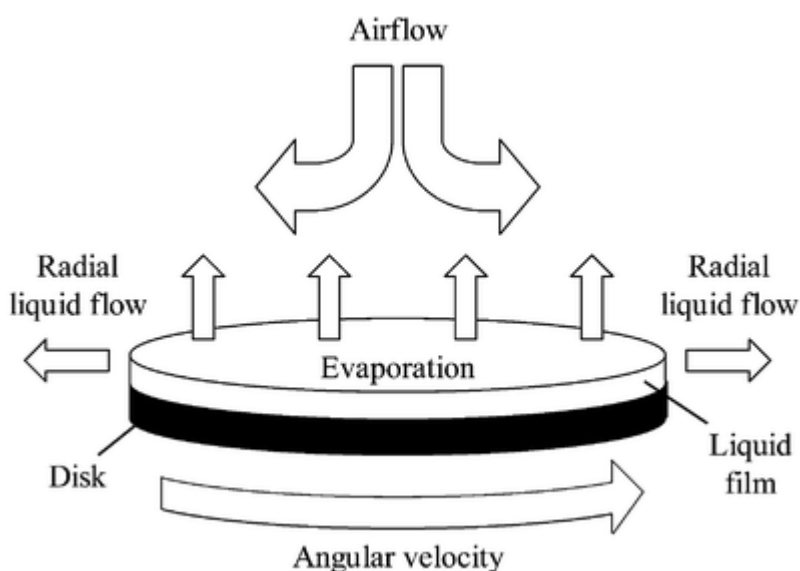


Figure 3.1. Schematic of the spin-coating process.

When the disk is static during the deposition, the film formation occurs in three steps: deposition, drainage of liquid and evaporation. In Figure 3.2 is shown the instruments we have used. After the solution deposition the substrate is spun at the desired angular velocity and the liquid spreads on the surface. The excess liquid is drained off by the centrifugal force. After a short time, thinning by drainage stops and evaporation takes over. Spin coating produce films with a typical thickness from one monolayer of material to several μm . It can give very homogeneous films with less than 5% thickness variation over areas larger than 100cm^2 .

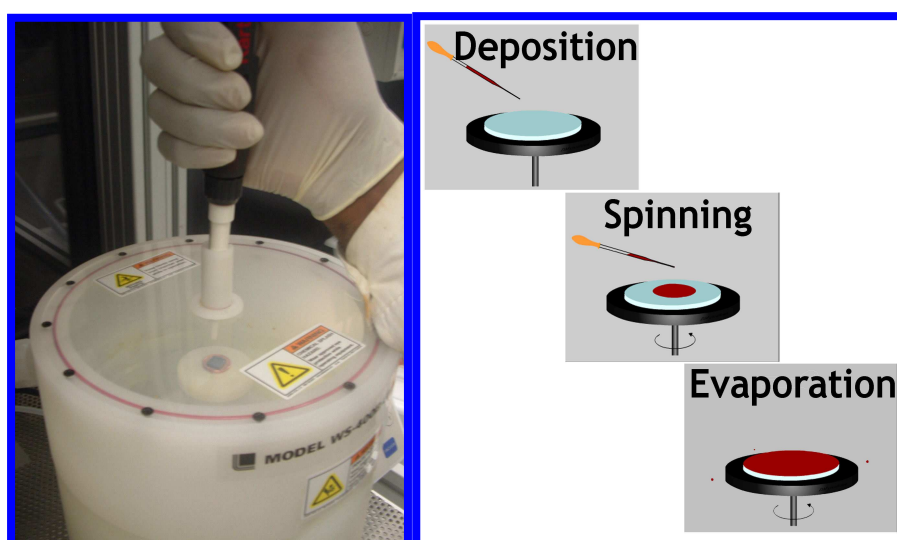


Figure 3.2 Schematic of the spin coater used (left) and the 3 steps of a spin coating process (right).

3.3 Model of the spinning process

The mechanism of spin coating is complex, due to the non equilibrium conditions and the fast time compared to the time scales of growth. It is not straightforward to model the process, and therefore it's not surprising that many assumptions and approximations has been applied when attempting to model the process. [2-8] Emslie et al. [2] were the first to describe the spin-coating process theoretically. They assumed a Newtonian behaviour of the fluid (*i.e.* a linear relationship between shear stress and shear

rate). Coriolis forces, gravitational gradients, as well as spatial and temporal variations in concentration, viscosity and vertical diffusivity were all neglected. In spite of these crude approximations, they could make generalized predictions of the flow pattern and the thickness of the resulting film. Later studies accounted for these neglected parameters resulting in significant improvement of the model to yield a better agreement with the experimental observations. [10-14]

A great amount of experimental work described in the literature deals with deducing empirical correlations between experimental parameters and film thickness [4, 5,8,15,16-22]. It is known that angular velocity, solution viscosity and solution concentration, significantly affect the film thickness, whereas the rate at which one film is deposited, the history of rotational acceleration prior to the final acceleration, and the total spin time have none or limited effects.

3.3.1 Angular velocity, concentration and viscosity

In a solution, concentration and viscosity are related and in general, viscosity increases with concentration. The angular velocity of the disc in the spin coating process and the concentration (or viscosity) have been correlated to the film thickness [13,14]. The relationship is schematically shown in Figure 3.3. This generalised correlation is a widely observed experimental result, which is phenomenologically expressed as:

$$h_f = k_1 \omega^\beta \dots\dots\dots(3.1)$$

where h_f is the film thickness, ω is the angular velocity, while k_1 and β are empirically determined constants. Figure 2.3 shows that film thickness decreases with angular velocity and increases with concentration. The constants, k_1 and β depend the physical properties of the material, substrate, on material/solvent

interactions, on solution/substrate interactions and also rheological properties. The viscosity η_0 is, amongst other parameters, incorporated in the constant k_1 .

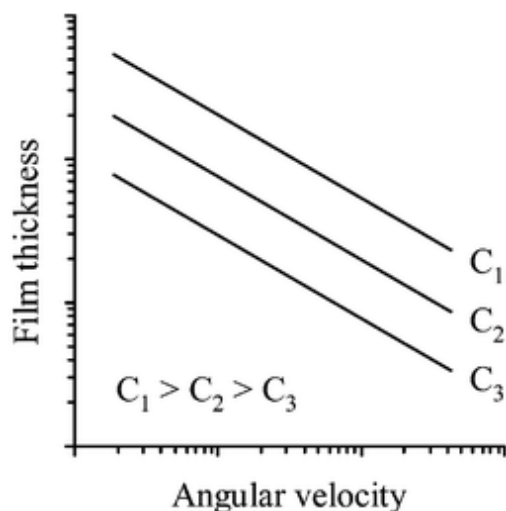


Figure 3.3 Schematic of the relation between film thickness, angular velocity and concentration (C_n) in a spin-coating process (logarithm scale). The same relation applies for viscosity.

Eqn. (1) can thus be expanded to eqn. (3.2).[20]

$$h_f = K_2 \eta_0^\gamma \omega^\beta \quad (3.2)$$

The exponent, γ , of the initial solution viscosity is typically observed to be in the range 0.29 – 0.39 for polymer solutions [4,17,18,20]. Spangler *et al.*[20] used the expression given by eqn. (3.2) and found the exponents γ and β to be fairly independent of the material/solvent systems studied. However, the proportionality coefficient, k_2 , varied significantly. It was suggested that information about the material/solvent interactions is possibly incorporated in k_2 (eqn. 3.2).

3.3.2 Solvent evaporation and solute diffusivity.

In early attempts to model the spin-coating process the solvent evaporation was neglected, [2-8] which led to models that were less consistent with experimental observations compared to more recent

models that incorporate a wider range of parameters. [9-14] Solvent evaporation changes the physical and thus the rheological properties of the solution during the coating process, especially if the latent heat of evaporation of the solvent is large. This can decrease the temperature (chilling) causing the solution properties to change (e.g. solvent volatility) and induce non-Newtonian behaviour such as elasticity and shear thinning. Chen [18] has studied the effect of solvent evaporation on spin-coating of polymer solutions. The effect of heat transfer in addition to momentum transfer (fluid flow) and mass transfer (solvent evaporation) was included. The film thickness was quantitatively correlated with the relative rate of solvent evaporation, the solution viscosity, and the angular velocity for a variety of solvents with significantly different volatility. Lawrence [14] challenged the conclusions made by Chen including solute diffusivity. Meyerhofer [2] found the viscosity of many solutions that he studied to be a power law function of the concentration.

Many works described in the literature qualitatively relate polymer film thickness with the volatility of the solvent. [18,20] Highly volatile solvents yield thicker films at a given polymer concentration and initial viscosity compared to low volatility solvents.

To determine the most suitable model for representing the thickness of our spin coated rotaxane thin films we assume that the solution acetone-rotaxane behaves as a newtonian fluid (since the acetone is highly volatile) and the rotaxane film thickness to be a power law of the concentration and spin speed. We estimate the empirical parameters and then compare them with those found in literature.

We have considered the phenomenological equation: [9]

$$h_f = K_0 C^\alpha \omega^\beta \quad (3.3)$$

where h_f is the film thickness in nanometer; K_0 , α , and β are constant depending on the system (acetone – rotaxane) and the experimental

conditions; ω is the spinning speed (in revolutions per min); C_0 the initial concentration of the solution (in g/l). In this work we measure the film thickness with AFM changing systematically, the concentration and the spinning speed.

3.4 Experimental section

Thin films were prepared by spin coating using highly pyrolytic graphite (HOPG). The area of HOPG is always 10mm X 10mm. The thickness was measured by scraping the film out of the surface with an AFM tip operated in contact mode and applying a sufficient force (2-5nN). Subsequently, we imaged in non contact mode a large area including the scraped area. From a linear profile on the topography image, we get the thickness of our samples (Figure 3.3). For every sample we have measured the thickness at four different area and found the values very similar in one sample. This confirms the homogeneity in thickness. We have investigated five samples for each single parameter. The topography images of other areas of the same sample show that films are homogeneous (Figure 3.4). We have studied the effect of the change in concentration at (1000, 1500, 2000, 3000) rpm respectively and consequently change in spinning speed at concentration (0,166; 0,25; 0,5; 0,75; 1) g/l. The volume of material cast every time is constant and the spinning time 10s. During all the experiments the relative humidity and the temperature were controlled and kept constant.

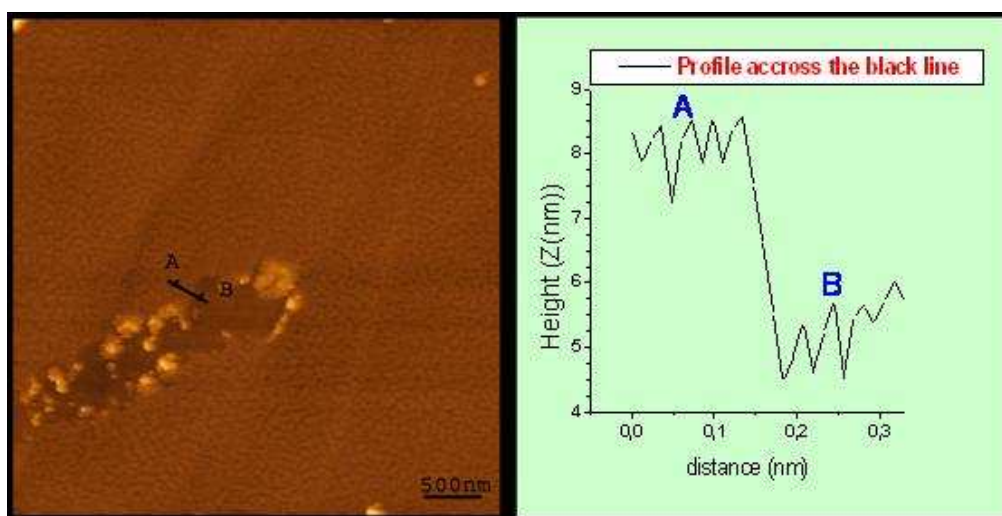


Figure 3.3 AFM images enclosing the scraped area with a line AB (left) whose profile is shown in the right image. The difference between the average height on the regions A and B gives film thickness $h_f = \Delta Z_{AB} \approx 3\text{nm}$.

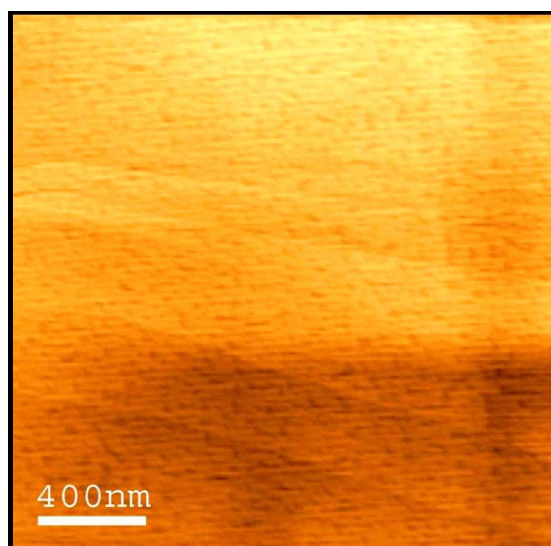


Figure 3.4 AFM topography image showing the typical morphology of a sample obtained for state the spin conditions. The film is rather homogeneous with a thickness of $3 \pm 0,3\text{nm}$ and a r.m.s. around 1 nm.

3.5 Results and discussion

In Figure 3.5 film thickness h_f is plotted vs spin speed ω , while in Figure 3.6 h_f is plotted vs concentration (C_0) The results show that the film thickness decreases by decreasing the initial solution concentration or by increasing the spinning speed as predicted by

the models. The parameters α and β were calculated plotting thickness vs the concentration and then vs the spinning speed on logarithm scale. We have extracted four values of α shown in table 3.1 and six values of β shown in table 3.2, then we have taken the mean of each series ($\alpha = 0,61$ and $\beta = - 0,17$) as representative results. The values were normalised to K since it encloses solvent and substrate physical parameters.

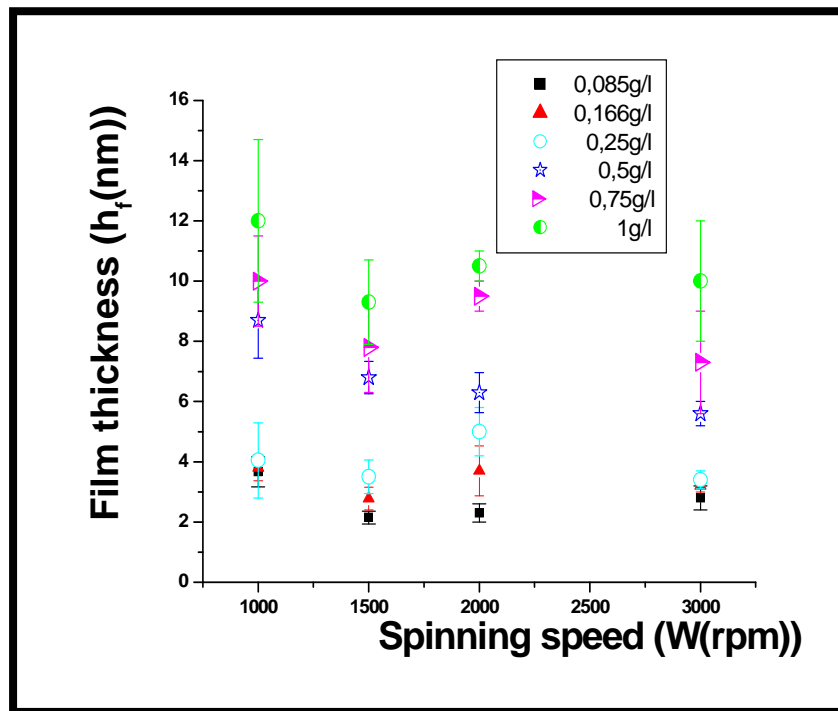


Figure 3.5 Dependence of film thickness vs spinning speed at five concentrations.

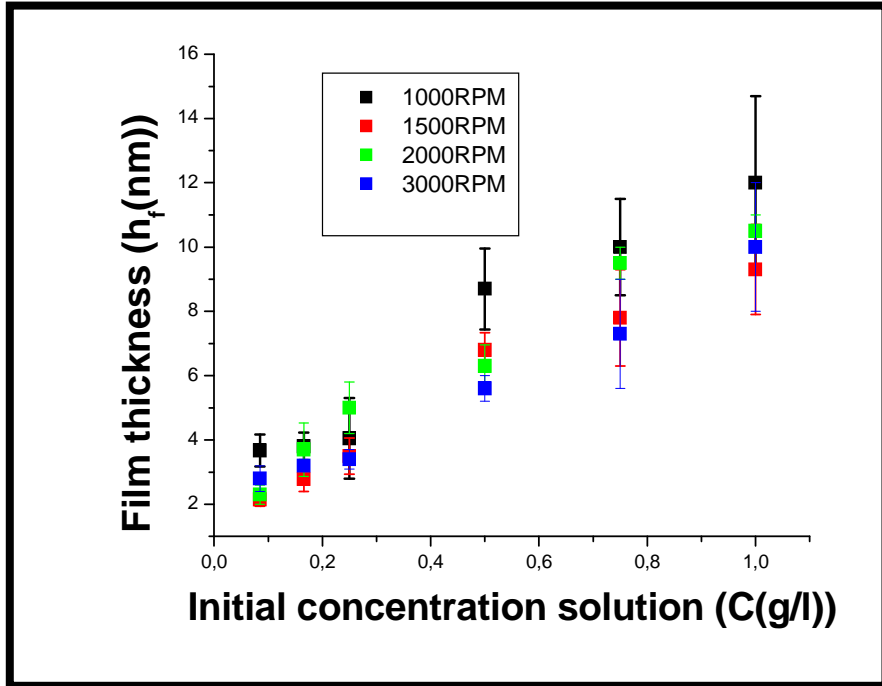


Figure 3.6 Dependence of film thickness vs initial rotaxane concentration at four spinning speeds

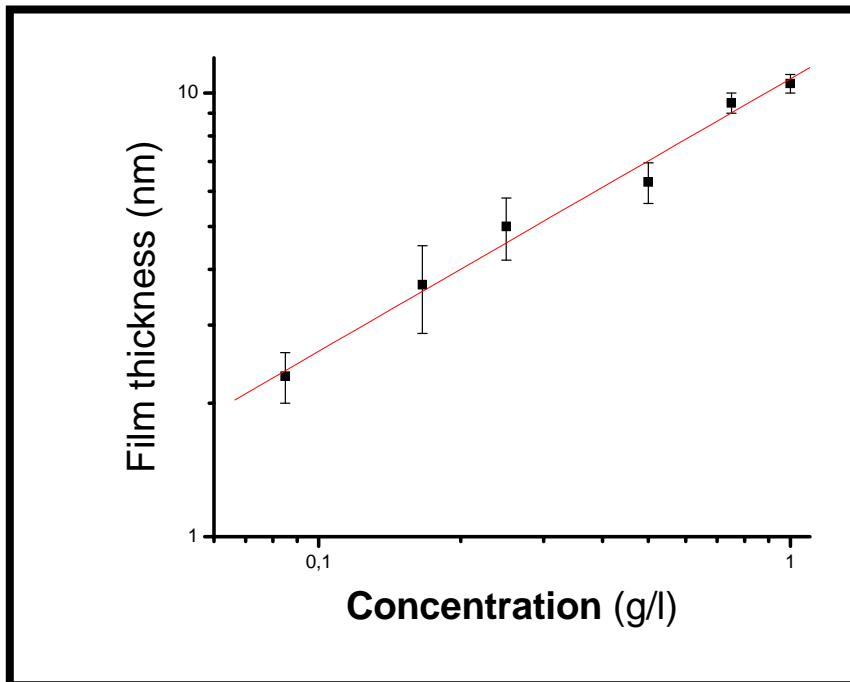


Figure 3.7 Log-Log plot of film thickness versus concentration for one speed (2000rpm), gives value of α (**0,614**).

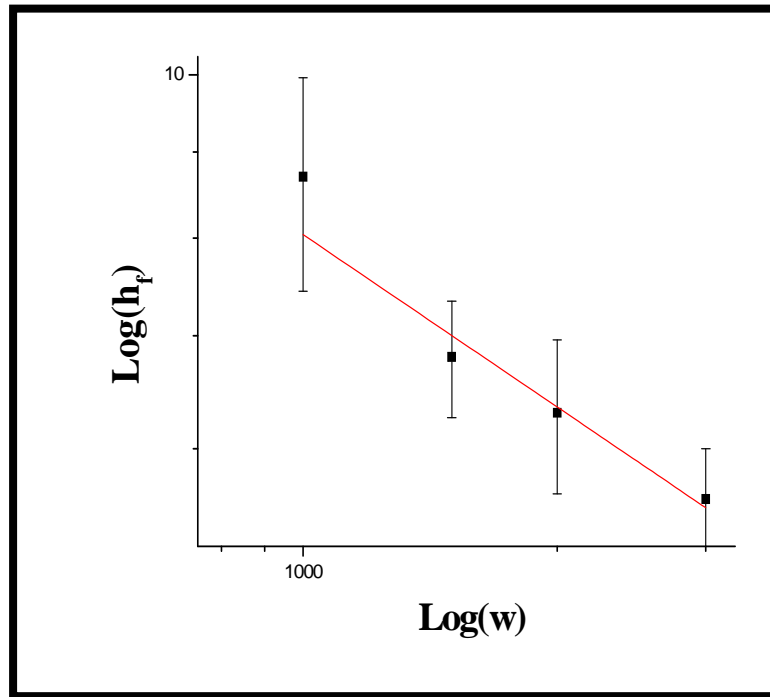


Figure 3.8 Log-Log plot of film thickness vs spinning speed gives one value of β (-0.33963)

Table 3.1

Concentration	β	Error
0,085	-0,11	$\pm 0,21$
0,166	-0,07	$\pm 0,12$
0,25	-0,15	$\pm 0,20$
0,5	-0,34	$\pm 0,12$
0,75	-0,11	$\pm 0,19$
1	-0,02	$\pm 0,25$
Mean value	-0,17	$\pm 0,57$

Table 3.2

Rpm	α	Error
1000	0,55	$\pm 0,09$
1500	0,64	$\pm 0,05$
2000	0,62	$\pm 0,04$
3000	0,50	$\pm 0,08$
Mean value	0,61	$\pm 0,03$

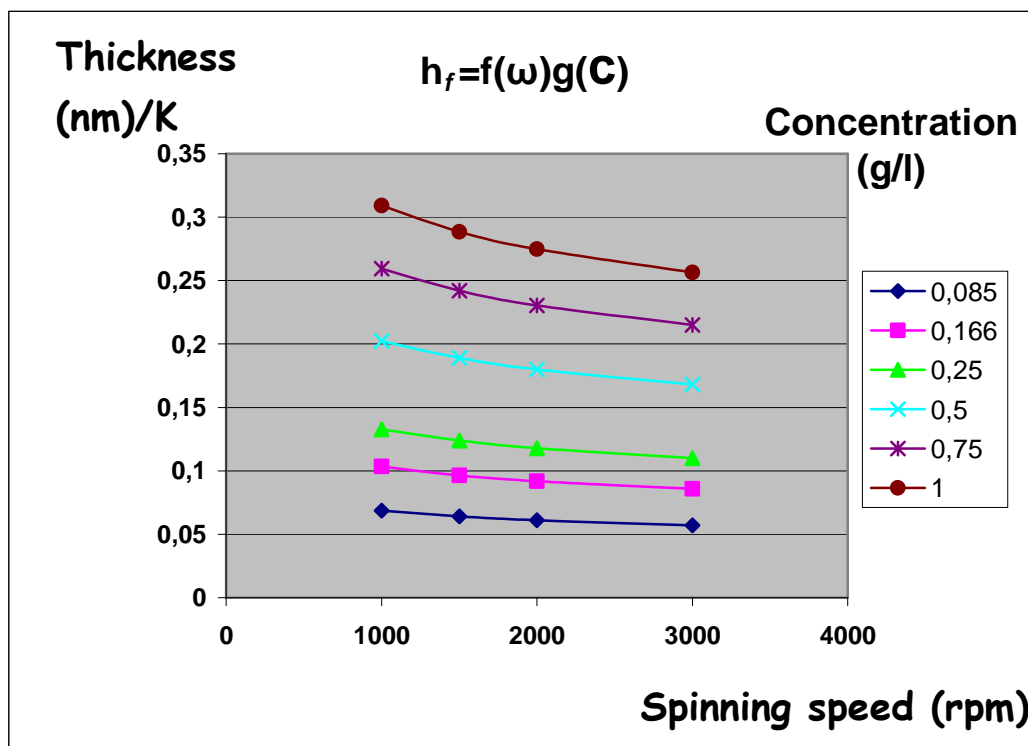


Figure 3.9-Thickness normalized vs spinning speed and concentration.

3.6 Conclusion

We have calculated the empirical parameters ($\alpha=0,61$ and $\beta = -0,17$) that allows us to estimate the thickness of the rotaxane thin film from an acetone solution. The graphs normalised of the thickness versus concentration and versus spin speed is based on the equations of Emslie and co-workers using the values of parameters that we have calculated. The curves show the same trend as Meyerhofer found for photoresists thin films [63] if we assume the solutions are very diluted. The outcome of the spin-coating process is not only influenced by the angular velocity and the physical properties of the solution, but, in addition, appear rather sensitive to parameters such as temperature, relative humidity and thermal surroundings for the evaporating solvent (heat transfer). Thus in order to perform systematic studies or reproduce rotaxane thin films, it is necessary to control a broad set of operational parameters.

Reference

- [1] K. Norrman, A. Ghanberi-Siahkali and L. B. Larsen, *Ann. Rep. Prog. Chem., Section C* 101, 174 (2005).
- [2] A. G. Emslie, F. T. Bonner and L. G. Peck, *J. Appl. Phys.*, 29, 858 (1958).
- [3] A. Acrivos, M. J. Shah and E. E. Peterson, *J. Appl. Phys.*, 31, 963 (1960).
- [4] B. D. Washo, *IBM J. Res.*, 21, 190 (1977).
- [5] S. A. Jenekhe, *Polym. Eng. Sci.*, 23, 830 (1983).
- [60] S. A. Jenekhe and S. B. Schuldt, *Ind. Eng. Chem. Fundam.*, 23, 43261 (1984).
- [7] S. A. Jenekhe and S. B. Schuldt, *Chem. Eng. Commun.*, 33, 135 (1985).
- [8] B. G. Higgins, *Phys. Fluids*, 29, 3522 (1986).
- [9] D. Meyerhofer, *J. Appl. Phys.*, 49, 3993 (1978).
- [10] S. A. Jenekhe, *Ind. Eng. Chem. Fundam.*, 23, 425 (1984).
- [11] W. W. Flack, D. S. Soong, A. T. Bell and D. W. Hess, *J. Appl. Phys.*, 56, 1199, (1984).
- [12] P. C. Sukanek, *J. Imag. Technol.*, 11, 184 (1985).
- [13] D. E. Bornside, C. W. Macosko and L. E. Scriven, *J. Imag. Technol.*, 13, 122 (1987).
- [14] C. J. Lawrence, *Phys. Fluids*, 31, 2786 (1988).
- [15] J. H. Lai, *Polym. Eng. Sci.*, 19, 1117(1979).
- [16] F. L. Givens and W. J. Daughton, *J. Electrochem. Soc.*, 126, 269 (1979).
- [17] W. J. Daughton and F. L. Givens, *J. Electrochem. Soc.*, **129**, 173 (1982).
- [18] B. T. Chen, *Polym. Eng. Sci.*, **23**, 399 (1983).

- [19] A. Weill and E. Dechenaux, *Polym. Eng. Sci.*, **28**, 945 (1988).
- [20] L. L. Spangler, J. M. Torkelson and J. S. Royal, *Polym. Eng. Sci.*, **30**, 644 (1990).
- [21] J. Q. Pham and P. F. Green, *J. Chem. Phys.*, **116**, 5801 (2002).
- [22] J. H. Kim, J. Jang and W.-C. Zin, *Langmuir*, **17**, 2703 (2001).

Chapter 4

Viscoelastic properties of rotaxanes

4.1 Introduction

The variation of the viscoelastic properties as the films dewet may also provide insight into the phenomenon of dewetting of these films. The material properties of samples can be investigated with AFM force microscopy by the force distance curves by relating the applied force to the depth of indentation as the tip is pushed against the sample. [1-5] In this chapter, we report the investigation by Atomic Force Microscopy (AFM) of the force curves between the tip and the rotaxane nanostructures. The aim is to measure the adhesion force and the surface energy of thin films during the transformation that ultimately leads to rotaxanes crystallites.

4.2 Forces in AFM

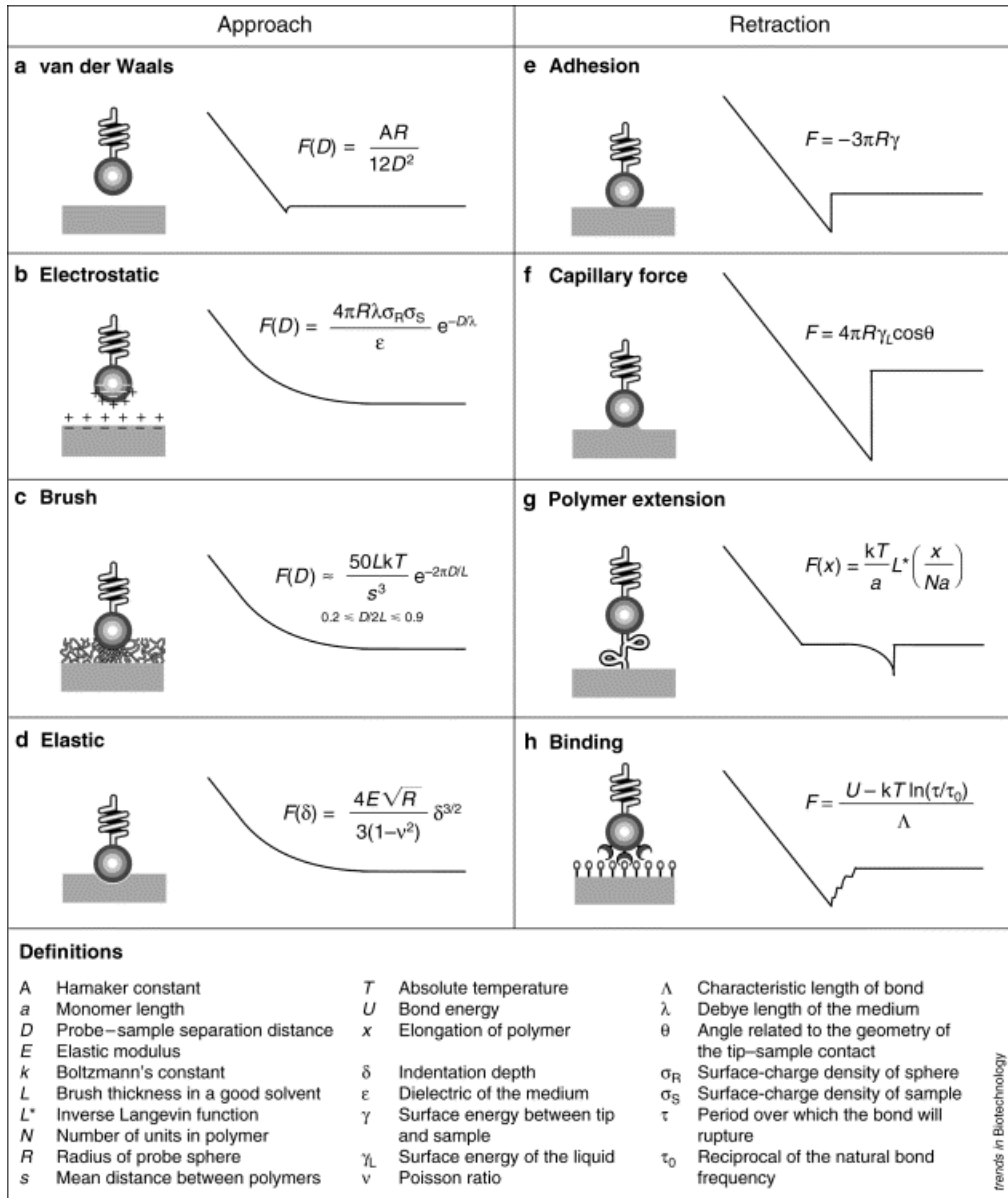
The knowledge of the forces acting between the tip and the sample is the basis of any quantitative analysis of AFM measurement. [6-8] In addition to the topographic measurements, the AFM can also provide much more information. It can record the amount of force sensed by the cantilever as the probe tip is brought close to, or even indented into a sample surface, and then pulled away. In Figure 4.1, examples of AFM force curves and the force law to interpret them are shown. This force mode can be used to measure the long range attractive or repulsive forces between the probe tip and the sample surface and to extract information on local chemical and mechanical properties like adhesion, elasticity and even thickness of adsorbed molecular layers, bond rupture lengths.

Force curves (force-versus-distance curve) typically show the deflection of the free end of the AFM cantilever as the fixed end of the cantilever is brought vertically towards and then away from the sample surface. Experimentally, this is done by applying a triangle-wave voltage pattern to the electrodes for the z-axis scanner. This causes the scanner to expand and then contract in the vertical direction, generating relative motion between the cantilever and sample. The deflection of the free end of the cantilever is measured and plotted at many points as the z-axis scanner extends towards the surface and then retracts back. By controlling the amplitude and frequency of the triangle-wave voltage pattern, the researcher can vary the distance and speed that the AFM cantilever tip travels during the force measurement. Measurements of cantilever amplitude and/or phase versus separation can provide more information about the details of magnetic and electric fields over surfaces and also provide information about viscoelastic properties of sample surfaces.

Interaction forces play a very important role in AFM imaging. There are three different types of interaction forces that have to be considered:

- A) force between the tip and the supporting surface.
- B) force between the tip and the molecules of our interest.
- C) force between the molecules and the supporting surface.

However, to separate the contributions of these interaction forces in the overall interaction force is often difficult. We have acquired force–distance curves prior to the measurements and we have adjusted load to be small as possible in order to not deform the sample under the tip.



trends in Biotechnology

Figure 4.1 Examples of atomic force microscope (AFM) force curves and the force laws used to interpret them. (a) An ideal, attractive, van der Waals force in the absence of other forces. (b) Repulsive electrostatic double-layer force in solution (c) Polymer-brushing forces that result from the thermally driven motion of polymers grafted onto a solid surface in solution. (d) Indentation curve on an elastic sample; (e) Adhesion between a sphere and a plane in the absence of contaminating adsorbates (typically in a vacuum). (f) Capillary adhesion, results from the formation of a water bridge between the tip and sample. (g) Polymer-extension force curves show a characteristic negative deflection far from the surface and a jump back to zero deflection as the polymer breaks or detaches from one of the surfaces (h) The unbinding of specific receptor–ligand pairs sometimes produces a stepwise return to zero deflection from the point of maximal adhesion. (adapted from [8])

4.3 Force Curves measurements

A plot of a force interaction between the tip mounted on a cantilever beam and the substrate as a function of the Z displacement constitutes a force curve. The force curve ($f(Z)$ Vs Z) is given by Hooke's law

$$F_z = K * \Delta Z$$

Z is the piezo displacement, ΔZ is the deflection of the cantilever, K the spring constant deflection of the cantilever and it is assumed that $\Delta(Z \rightarrow \infty) = 0$

Forces-distance curves provide information on repulsion, attraction and adhesion between the tip and the sample surface. In Figure 4.1, at left we illustrated a force-curve measurement and at right, the movements of the tip and deformation of the cantilever during a measurement. In the following, we will present how to extract information from the force-curve.

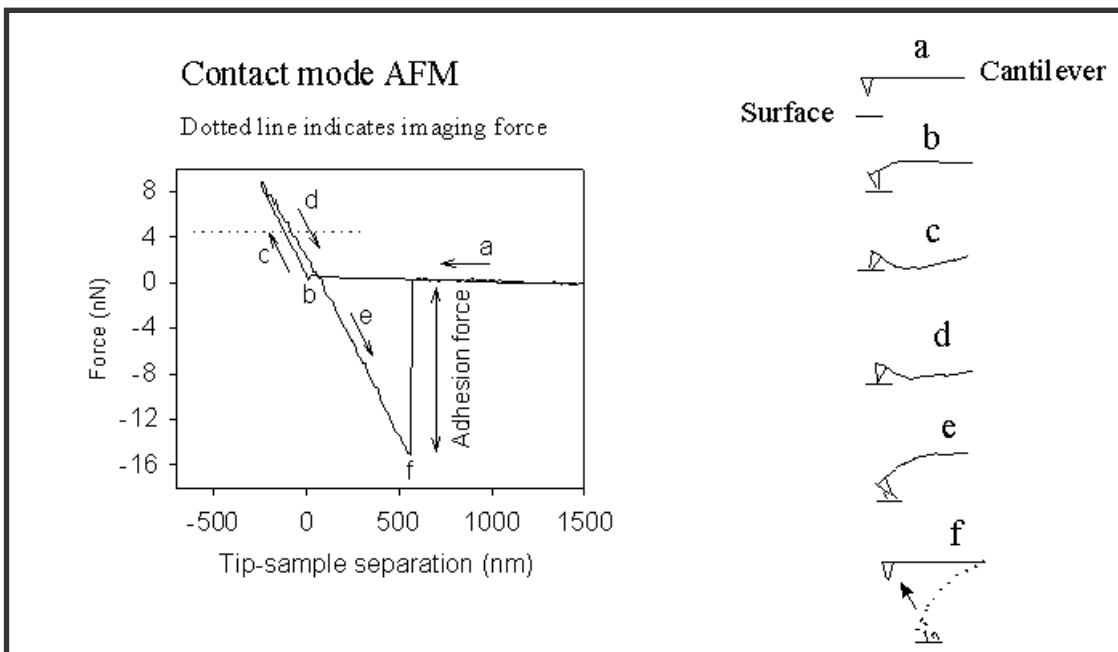


Figure 4.2 Illustration of a force-curve plot.

- ‘a’ The piezo extends; the tip approaches the surface and there is no contact with the surface yet. In this region, if the cantilever feels a long-range attractive (or repulsive) force it will deflect downwards (or upwards) before making contact with the surface.
- ‘b’ as the probe tip is brought closer to the surface, it may “jump to contact” if the gradient of attractive force from the sample exceeds the spring constant of the cantilever. The “jump to contact” force represents the maximum attractive force that can be probed.
- ‘c’ Once the tip is in contact with the surface, the cantilever will deflect upwards as it is pushed closer towards the sample this region is dominated by repulsive forces. If the cantilever is sufficiently stiff, the probe tip may indent into the surface at this point. The slope or shape of the contact part of the force curve provides information about the compliance of the sample surface.
- ‘d’ Piezo retracts; first repulsive forces are decreased and the cantilever relaxes downward. As the “zero” force line is crossed, the attractive forces become dominant, bending the cantilever downwards.
- ‘e’ The cantilever bends downwards as the surface attraction holds into the tip.
- ‘f’ As the tip continues its ascend, it finally breaks free of surface attraction due to adhesion force and the cantilever jumps out abruptly from the contact as the maximum adhesion force is reached.

A key measurement of the AFM force curve is the point at which the adhesion is broken and the cantilever comes free from the surface. This jump in deflection is the rupture force required to break the bond between tip and sample or **adhesion force**.

4.4 Theoretical considerations

Adhesion forces between solids particles: JKR theory

One of the first attempts at a rigorous theoretical treatment of the adhesion of elastic spheres is due to Johnson, Kendall and Roberts, whose theory, “JKR theory” [9] forms the basis of modern theories of adhesion mechanics. JKR theory states that as two elastic spheres whose radii are R_1 and R_2 , are pressed together under an external load force F , the radius of their area of contact is given by:

$$a^3 = \frac{R}{K} \times \sqrt{[F + 3\pi RW_{12} + (6\pi RW_{12}F + (3\pi RW_{12})^2)]} \quad 4.1$$

where

$$R = \frac{R_1 R_2}{R_1 + R_2}, \quad 4.2$$

W_{12} is the surface energy per unit area

$$K = \frac{4}{3} \pi (k_1 + k_2) \quad 4.3$$

with k_1, k_2 elastic constants of the two spheres

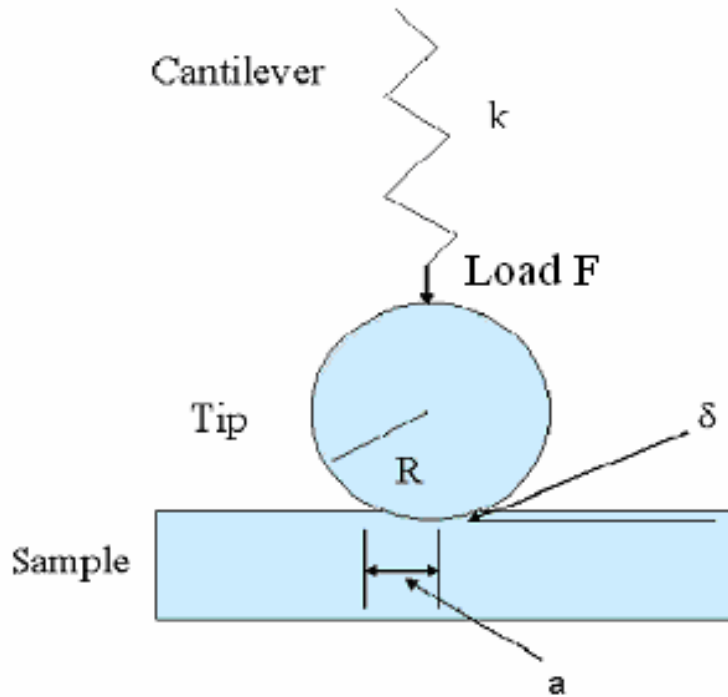


Figure 4.3 Schematic representation of the tip-cantilever system in AFM

For a sphere (tip) on a flat surface of the same material, ($R_2=\infty$) then $R = R_1$.

Under zero external load force $F = 0$, the contact radius is a_0 and given by

$$a_0 = \sqrt[3]{\left(\frac{6\pi RW_{12}}{K}\right)} = \sqrt[3]{\frac{12\pi R\gamma_{12}}{K}} \quad 4.4$$

where

γ_{12} is Surface energy

The solids still adhere under negative load ($F < 0$) until at some critical force and the surface suddenly jump apart.

For a sphere on a flat surface this “pull-off” force is given by

$$\boxed{F_{adh} = -3\pi\gamma_{12}R} \quad 4.5$$

and the separation occurs abruptly once the contact radius reaches

$$a_s = a_0/4^{1/3} = 0,63a_0 \quad (4.5)$$

4.5 Experimental section

The samples were prepared by spin coating of 20ml of the rotaxane **1** 0,5g/l in acetone, spun at 1500 rpm for 15s. The substrate is freshly cleaved highly oriented pyrolytic graphite (HOPG) 10 mm X 10 mm, cleaned by exfoliation.

The topography was first investigated every time by AFM in non contact mode and then we switched to contact mode and performed the force-distance curves measurements. Upon annealing, the measurements were repeated successively. The relative humidity during the whole experiment was kept at 46%.

The radius of the tip measured by a scanning electron microscopy (SEM) was found to be 75nm. There is no specific preparation for the tip but we need to calibrate it before starting the measurements.

4.6 Results and discussion

In this experiment the films recrystallise by two different routes:

- 1) Nucleation and growth of holes
- 2) Ostwald ripening.

We performed the measurements in the two situations and the results are presented here.

4.6.1 Recrystallisation by nucleation and growth of holes

In Figure 4.5 we report a plot of the evolution of the surface energy during the recrystallisation process as obtained by the measurements of the adhesion force. The energy is almost constant during the whole experiment. The error bars are very large and this

could be due to the fact that we performed the experiment in air. The initial film presents small holes that grow with the annealing time (90°C). Figure 4.6 shows the AFM images of the samples investigated.

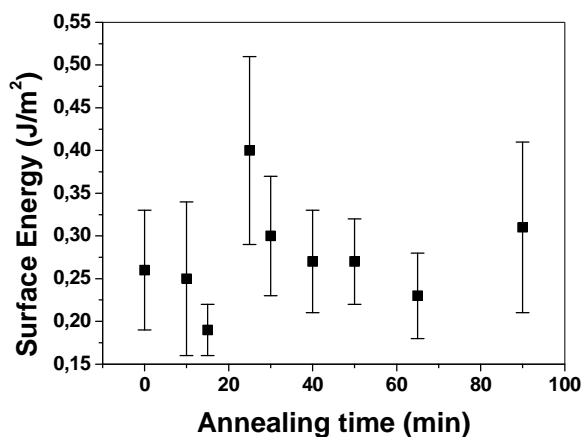


Figure 4.5 Plot of the variation of the surface energy of rotaxane **1** thin film with the annealing time according to nucleation and growth of holes mechanism as shown in figure 4.6..

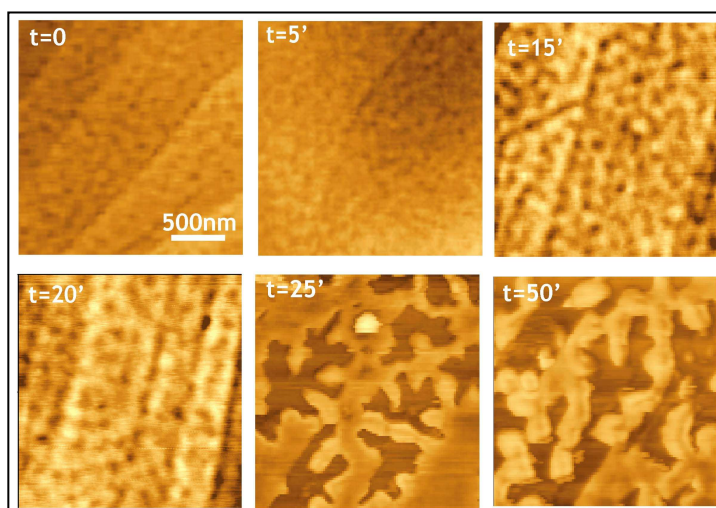


Figure 4.6 AFM images showing the morphology of the films during the annealing process. The corresponding adhesion force was previously shown in figure 4.5. The images show a dewetting by nucleation and growth of holes. The initial film thickness is around 25nm. Up to 50 min annealing time, they were no morphological changes on the topographic images.

4.6.2 Recrystallisation by Ostwald ripening

We observed that the films dewet and recrystallise by Ostwald ripening mechanism as already shown in chapter 2, the film first dewets from the substrate to form nanosized droplets whose ripening gives rise to spatially correlated motives. In a later stage, the larger droplets nucleate and coalesce into crystallites that further grow into larger crystals by incorporating the surrounding droplets.

We have extracted the adhesion force of the nanodots and the crystal in every sample after many annealing time intervals throughout the whole experiment. The adhesion force or energy of the nanodots turns out to be higher than that of the crystals. This confirms the stability of the crystal which is growing at the expense of the nanodots. Figure 4.7 shows the trend of the surface energy during the annealing process and the corresponding morphology of the samples (viz AFM) is shown figure 4.8.

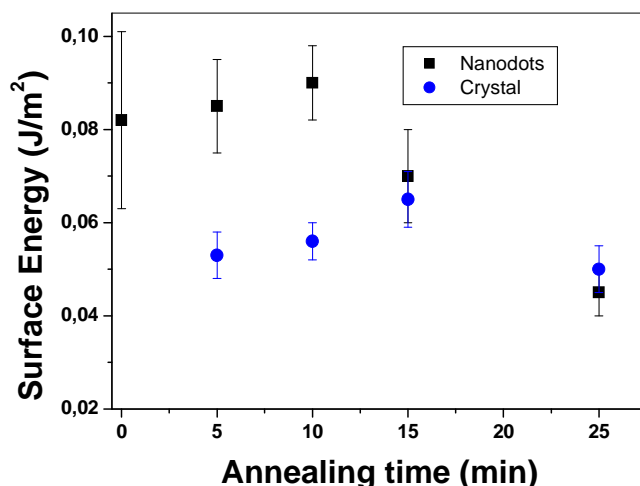


Figure 4.7 plot showing the variation of the surface energy of the rotaxane **1** with the annealing, according to the Ostwald ripening mechanism, as shown in Figure 4.8.

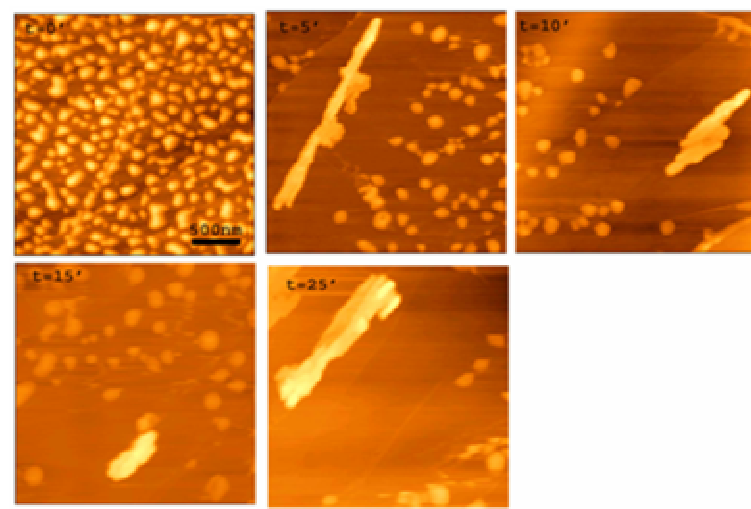


Figure 4.8 AFM image showing the topography of the samples. In this case the recrystallization occurs by Ostwald ripening. The corresponding surface energy versus annealing time was shown previously in figure 4.7.

4.6.3 Comparison of Surface Energies by three methods

We have compared the surface energy obtained by measuring the adhesion force with an AFM with those given by computational investigation reported in the chapter 2 and by contact angle measurements, performed before the annealing of the films. These values are summarized in the table 4.1.

Table 4.1

Surface Energy (J/m ²)	By AFM		Computational investigations			By Contact angle
	Nucleation and growth of holes (route 1)	Ostwald ripening (route 2)	111	100	010	
	0,260±0,051	0,080±0,021	0,342	0,052	0,091	0,025

4.7 Conclusions

AFM has been used to investigate viscoelastic properties of rotaxanes.

The surface energy of rotaxane thin films via nucleation and growth of holes exhibits significant variations as it undergoes the transformation from film to crystals under the influence of temperature. The energy landscape for route 1 is more complex compared to route 2. Also, the energies are an order of magnitude higher for route 1. For route 2, the droplets have slightly higher energy than crystallites, but eventually both attain the same energy. This may indicate that droplets in time crystallise, the timescale of this crystallisation depends on the droplets size. The measured values of surface energy compare well with those obtained from molecular mechanics simulations and contact angle measurements.

References

- [1] J. A. Ruan and B. Bhushan, *Trans. ASME J. Tribol.* **116**, 378. (1994).
- [2] N. A. Burnham, R. J. Colton, and H. M. Pollock, *Nanotechnol.* **4**, 64 (1993).
- [3] J. P. Aime, Z. Elkaakour, C. Odin, T. Bouhacina, D. Michel, J. Curely, and A. Dautant, *J. Appl. Phys.* **76**, 754 (1994).
- [4] H. A. Mizes, K.-G. Loh, R. J. D. Miller, S. K. Ahuja, and E. F. Grabowski, *Appl. Phys. Lett.* **59**, 2901 (1991).
- [5] S. M. Hues, C. F. Draper, and R. J. Colton, *J. Vac. Sci. Technol. B* **12**, 2211 (1994).

- [6] E. Palacios-Lidón and J. Colchero *Nanotechnology* **17** 5491 (2006).
- [7] R. E. Mahaffy, S. Park, E. Gerde, J. Käs, and C. K. Shih, *Biophys J.* **86**,1777, (2004).
- [8] W. F. Heinz and J. H. Hoh, *Trends in Biotechnology* **17**, 143 (1999).
- [9] J. Israelaschvili, *Intermoleculars and Surface Forces*, Academic press London (1992).

Chapter 5

FET device performance, morphology and X-ray thin film structure of unsubstituted and modified Quinquethiophenes

5.1 Introduction

Few years ago, it has been demonstrated that field effect transistors (FET) fabricated with thiophene oligomers [1,2] can reach charge carrier mobility values in the order of $1 \times 10^{-2} \text{ cm}^2/\text{V s}$ and $I_{\text{on}}/I_{\text{off}}$ ratios in the order of 10^6 – 10^7 , which are in the range of the best values obtained so far with organic materials, when using pentacene thin films [3] as the active semiconductor layers. Although early measurements on oligothiophenes indicated that charge carrier mobilities should increase on increasing the oligomer size, [4,5] more recent experimental evidence indicates very similar mobility values for quater- quinque- and sexithiophenes. [1,6a] These results encourage investigations into thin film field-effect transistors based on the shorter thiophene oligomers, such as quinquethiophene (T5), the least investigated one, which are more soluble and, owing to their higher ionisation potentials [7] also less susceptible to oxidation. Figure 5.1 shows the quinquethiophene's that we have investigated (unsubstituted quinquethiophene (T5) substituted quinquethiophene (T5Me), and modified quinquethiophene (T5A)).

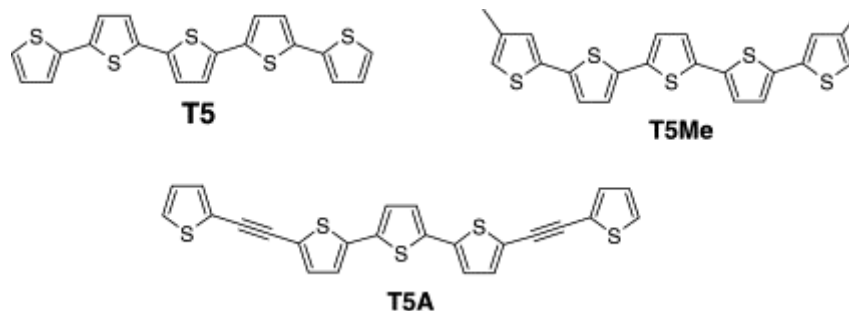


Figure 5.1 Schema of unsubstituted Quinquethiophene (T5), substituted Quinquethiophene (T5Me) and modified Quinquethiophene (T5A).

In the last years, it was reported that T5 exhibits a hierarchical organisation across length scales with highly crystalline thin films characterised by high carrier mobility values [6a]. To date, no investigation has been carried out on the dependence of the charge carrier mobility of T5 with the morphology of the thin films. Moreover, no systematic studies have been carried out on how structural modifications affect the solid-state organization and the electrical characteristics of odd-number thiophene oligomers. Although remarkable improvements have recently been achieved on thiophene-based molecular semiconductors, from optimization of device and deposition conditions [5] to material design [8], to the synthesis of *n*-type [9] and ambipolar [10] semiconductors, no clear relationship has as yet been established between molecular structure and electrical performance.

5.2 Motivations and Aim of the chapter

The aim of this chapter is to discuss the general trends of the variation of the electrical properties of T5 on changing film deposition conditions or introducing structural modifications of the backbone. This work aims to contribute a rationale for the design of new and more performant materials and has been the subject of reference [11].

5.3 Experimental section

5.3.1 Material instruments and methods

The bottom configuration FET devices used in this study is shown in Figure 5.2 [6], with interdigitated source and drain gold contacts, channel width and length of 1.1 cm and 10 μm , respectively. The SiO_2 surface was not functionalised with any primer or chemical treatment. The different oligomers were deposited on the channel region, by vacuum evaporation, at a rate of about 0.1 nm/s. Film thickness was measured during evaporation with a quartz thickness monitor and verified at the end of the process, using a mechanical profiler (Veeco Dektak 6M). All electrical measurements were performed in ambient atmosphere. All oligomers were purified by silicagel chromatography before use, followed by vacuum sublimation. X-ray diffraction (XRD) measurements were carried out at room temperature, using a Bragg/Brentano diffractometer (Philips PW1050/61-PW1710), equipped with a graphite monochromator in the diffracted beam, with a Cu anode as X-ray source. Atomic force microscopy (AFM) images were obtained with an atomic force microscope (Autoprobe CP Research Park scientific instrument) operated in air in intermittent contact mode. The cantilevers were silicon cantilevers (NT-NDT NSG10) with high reflective Au coating. The typical curvature radius of the tip was less than 10 nm with a typical resonant frequency of about 255 kHz. Typical relative humidity (RH) during the measurements was controlled with a hygrometer (about 55%).

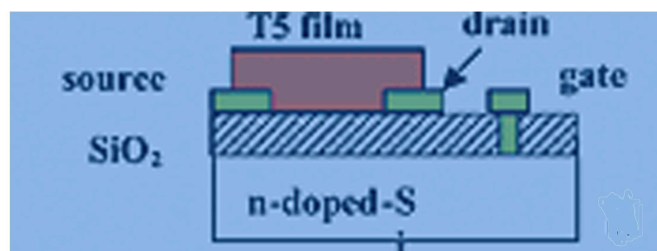


Figure 5.2 Bottom contact configuration FET with T5 thin film

5.3.2 Results

5.3.2.1 Structure by XRD

The molecular structure of the oligomers used here is given in Figure 5.1. With respect to unsubstituted quinquethiophene (T5), one of the modified derivatives bears two methyl groups (—CH_3) grafted at the external β -position (T5Me), while in the other one (T5A) the two terminal thiophene rings are separated from the internal terthiophene core by acetylenic spacers ($\text{—C}\equiv\text{C—}$). The microwave-assisted synthesis, purification methodology and differential scanning calorimetry characteristics of these compounds are reported in references [6a,b]. Of the three compounds, only T5Me displays liquid-crystalline properties [6a,b].

All compounds show a remarkable ability to form highly ordered and crystalline thin films, as shown by the numerous intense high-order reflections in the XRD profiles. The XRD plots of 150 nm thick films of the three samples, deposited at different substrate temperatures, are shown in Figure 5.3, Figure 5.4 and Figure 5.5.

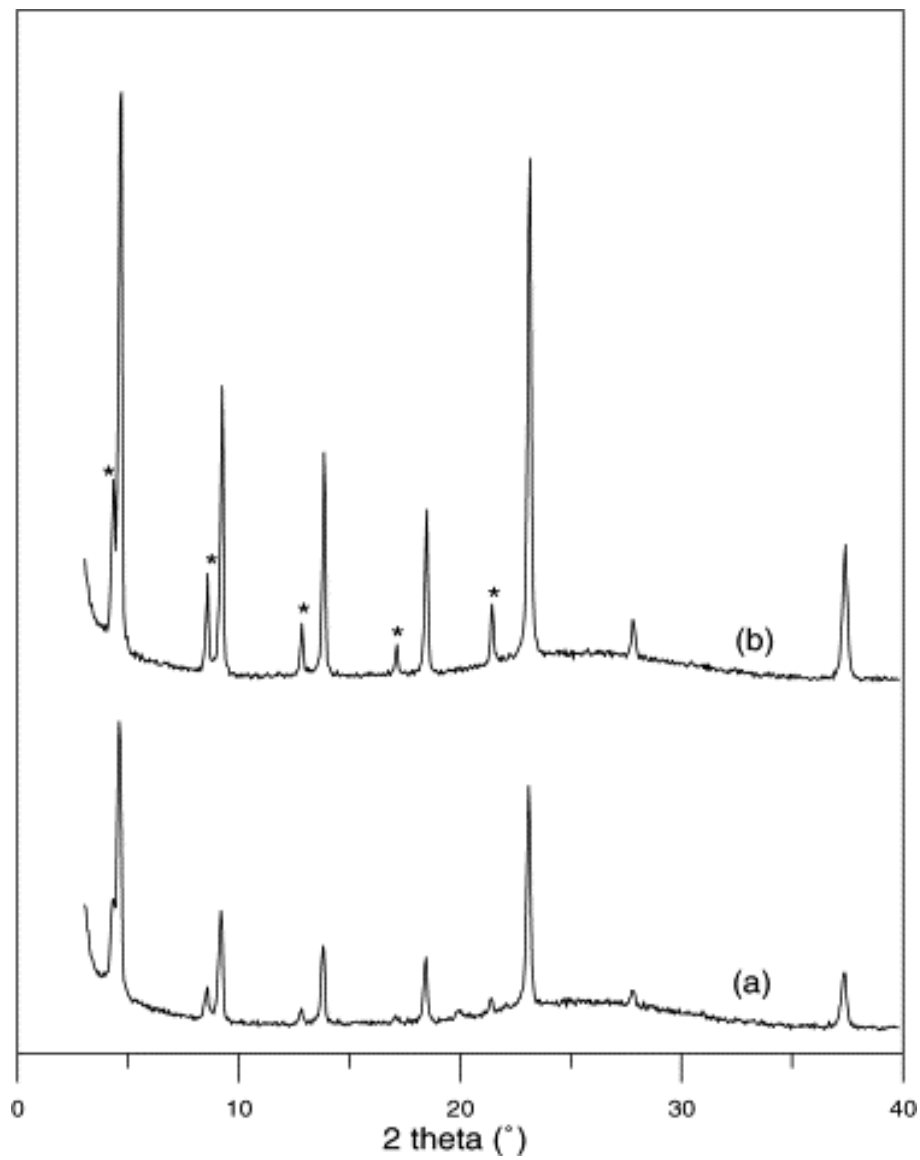


Figure 5.3 XRD profile of 150 nm thick films of T5 vacuum evaporated at a substrate deposition temperature of 30 °C (a) and 90 °C (b).

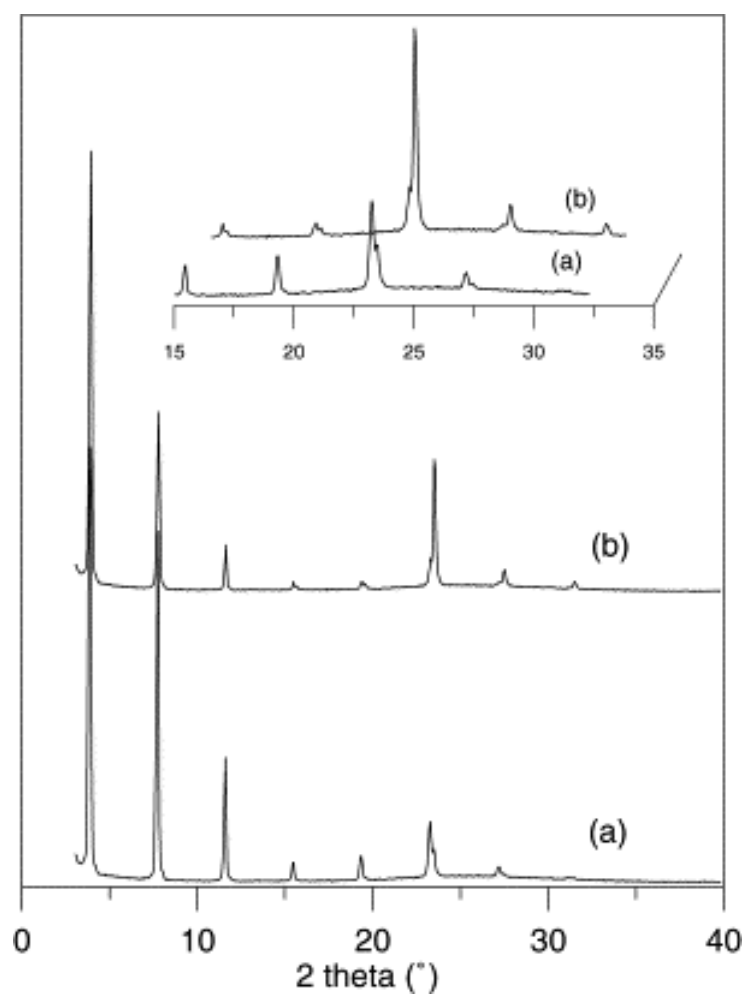


Figure 5.4 XRD plots of 150 nm thick films of T5Me for substrate deposition temperatures of 30 °C (a) and 90 °C (b). The inset is a magnification of the region between 15 and 35 at the two temperatures.

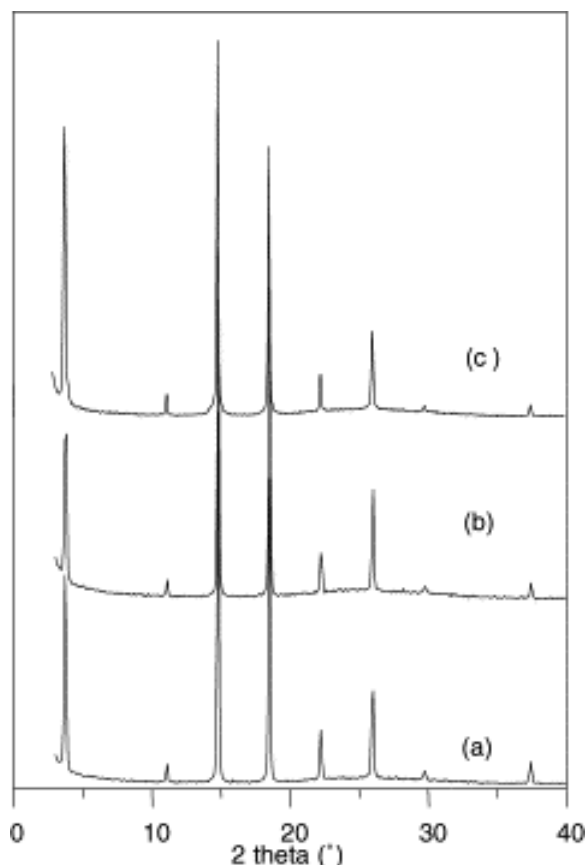


Figure 5.5. XRD plots of 150 nm thick films of T5A for substrate deposition temperatures of (a) 30 °C, (b) 90 °C and (c) 140 °C.

Figure 5.3 shows the XRD patterns of two films of T5 deposited at 30 and 90 °C. The same reflections appear in both samples, belonging to two distinct series of peaks with periodicities of 1.92 nm (most intense peaks) and 2.06 nm (peaks indicated by asterisk), respectively, or to multiples of these values. Since the crystal structure previously reported for T5 [12] shows a monoclinic cell with an a -axis of 3.9 nm, we can assume the most intense peaks as being due to the $h00$ reflections (h even). Although T5 is known for its tendency to form very ordered thin films [6], here the presence of a population of T5 ordered in a slightly different way has to be assumed in order to explain all reflections. The presence of a polymorph with a different inclination of the molecules with respect to the unit cell axes can be hypothesized. As

shown in the figure, the effect of increasing the substrate deposition temperature on T5 is to increase the amount of the minor polymorph in the film. It is worth noting that polymorphs of the shorter and the longer homologues of T5, namely, quater- and sexithiophenes, have also been described from single crystal X-ray structures, only differing in the magnitude of the herringbone angle [13,14].

Comparing the peak widths of the films of T5 obtained at the different substrate deposition temperatures, an enlargement of the domain size in the *h00* direction is observed. Application of Scherrer equation [15] allows us to estimate the size of the coherent domains to be 53 and 66nm for the samples prepared at 30 and 90 °C, respectively.

The XRD patterns of two T5Me samples deposited at different temperatures are shown in Figure 5.4. The most intense reflections appear at the same angular positions in both samples and all reveal a periodicity of 2.29 nm (or multiple thereof). They are likely to be of the *h00* kind, although the fact that no single crystal or powder X-ray structures have been reported for this compound makes the assignment somewhat uncertain. Some differences in the diffraction profiles are appreciable for the reflections for 2θ greater than 15°. As reported in the inset of Figure 5.4, some reflections are splitted and the relative intensities in each couple is reversed in the samples deposited at the different temperatures. The figure shows that the reflections at the smaller angles are more intense in the substrate deposited at 30 °C.

From the *d*-spacing values we assume these peaks as higher orders of *h 0 0* type reflections. We used different experimental conditions to test the presence of a splitting also in the reflections for 2θ less than 15°, but with negative results. Therefore, the presence of a second polymorph can be excluded in this case. The more intense

reflections at $2\theta > 15^\circ$ for the sample obtained at 90°C should instead be explained by assuming that a fraction of the sample is oriented in a slightly different way with respect to the substrate. In that case, these reflections should be indexed as $h0l$ with a large l value. Thus, in the case of T5Me, the effect of increasing the substrate deposition temperature is to change the orientation of some crystalline domains with respect to the substrate. The size of the domains, calculated from the peak width, is not appreciably affected by the deposition temperature, being about 72 nm for both samples.

The XRD patterns of T5A deposited at different substrate temperatures are reported in Figure 5.3. Contrary to T5 and T5Me, no changes were observed in the X-ray patterns of the films increasing the substrate deposition temperature up to 140°C . The figure shows that for $T=30, 90$ and 140°C the plots are very similar and consistent with highly crystalline films. The plots are characterized by several reflections, all corresponding to a period of 2.39 nm (or multiple). The reflections are very sharp and it is possible to estimate a size of the crystalline domains of about 100 nm.

5.3.2.2 Morphology by AFM

The morphology of T5 thin films was imaged by intermittent contact AFM. Figure 5.6 shows the AFM images of 15, 80 and 150 nm thick films of T5 deposited at 30, 60 and 90°C substrate temperatures.

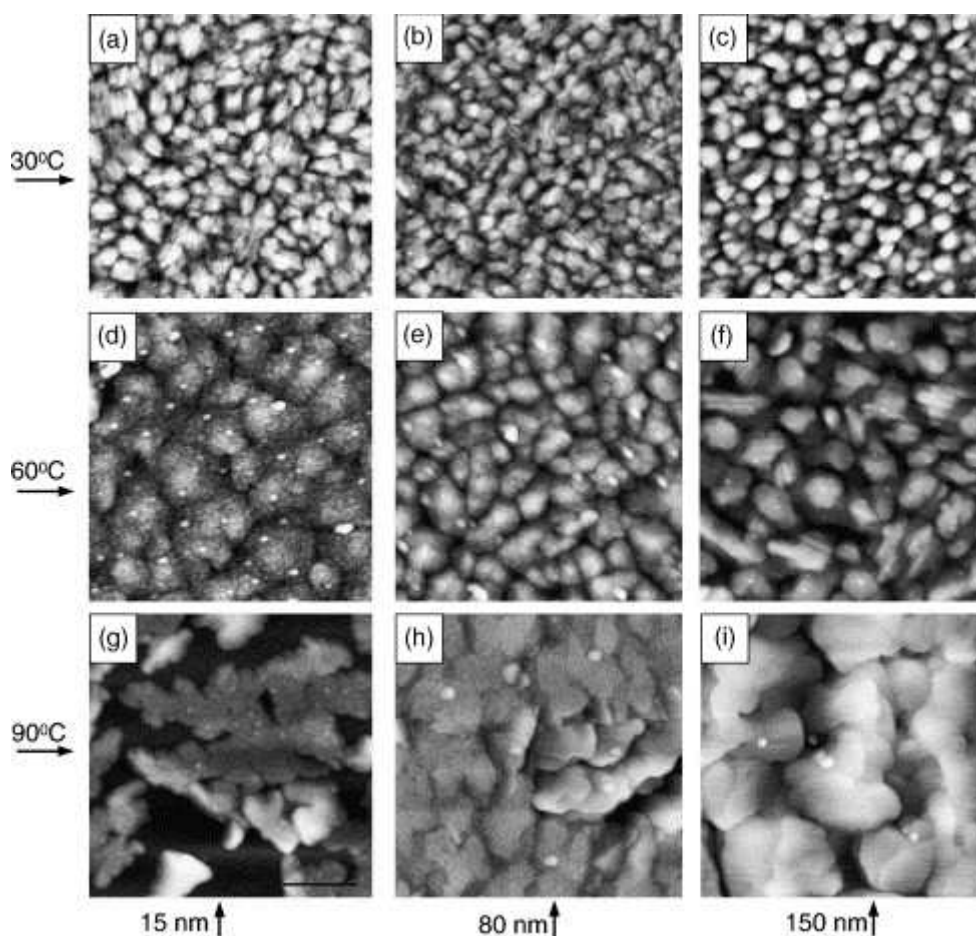


Figure 5.6 AFM topographical images of 15, 80 and 150 nm thick films of T5 (z -scale is 0–180 nm, all figures have $3\ \mu\text{m} \times 3\ \mu\text{m}$ size) on thermal SiO_2 . The films were grown at three different substrate deposition temperatures: 30, 60, 90 °C as indicated in the figure.

Upon increasing the substrate deposition temperature there is a dramatic change in the morphology of the film. Figure 5.6 a–c show the topography of the T5 films grown at 30 °C. The morphology exhibits grains, homogeneously dispersed on the surface. The r.m.s. roughness of the surface is 16 ± 2 nm, almost independent of film thickness and growth temperature. In the thinner films (15 and 80 nm, corresponding to Figure 5.6a and b), the clusters appear to be slightly elongated. No ordered layered structure within the grains is observed. However, with the exception of 150 nm thick films, the presence of striped domains inside the clusters is evident. These striped domains have always the same orientation inside a cluster

but there is no relation among the stripes orientation of different clusters. The striped domains were already observed in samples prepared by melting-quenching processes of T5 films. [6a] Figure 5.7 shows a zoom of the 80 nm thick film grown with a substrate deposition temperature of 30 °C.

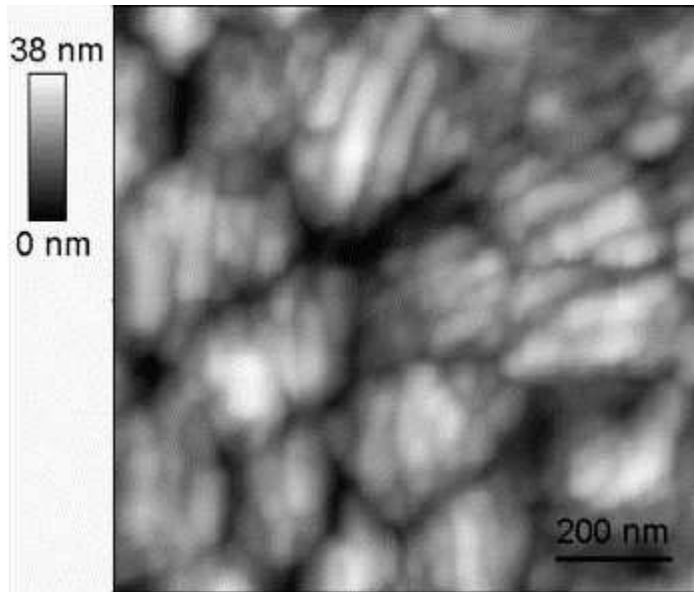


Figure 5.7 AFM topographical image of the 80 nm thick film of T5 grown at 30 °C on thermal SiO₂. The film exhibits striped domains similar to those already observed in samples prepared by melting-quenching processes [6a].

The mean diameter of the clusters, measured from the power spectra (Figure 5.8a), was 336 ± 20 nm. In order to investigate the spatial correlation of the clusters we compare the power spectral densities (PSD) [16] estimated from the AFM images. All films grown at 30 °C exhibit very similar PSD. Furthermore the PSD shows that the topographic fluctuations are spatially correlated.

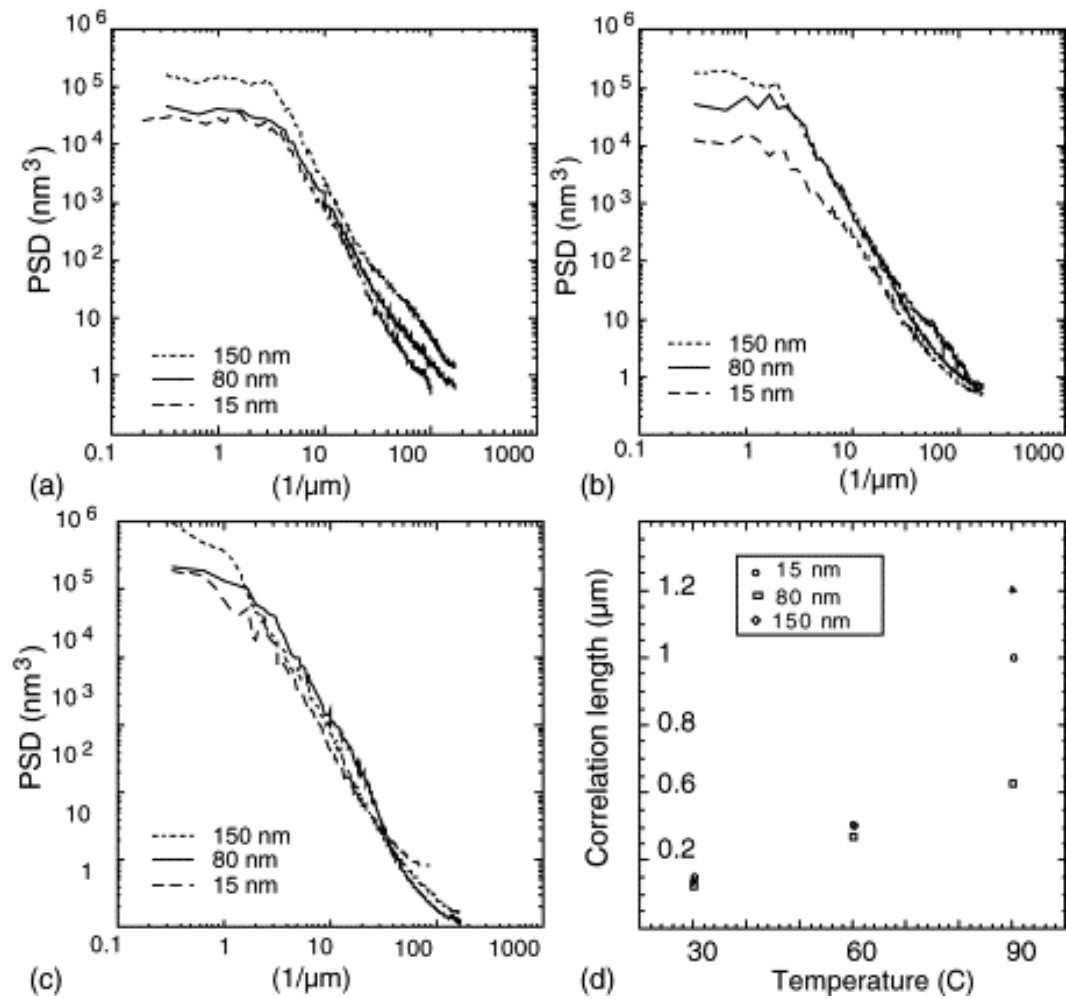


Figure 5.8 Power spectral densities measured from the AFM topographic images. (a) Films grown at 30 °C; (b) films grown at 60 °C; (c) films grown at 90 °C. (d) Plot of correlation length vs. deposition temperature.

Growing the sample at 60 °C (Figure 5.6d–f) the shape slightly elongates (this is more evident in the 150 nm thick sample) and the mean diameter, measured from the power spectra (Figure 5.8b), increases in the range 480 ± 20 nm, while the r.m.s. roughness remains almost constant (15 nm). As the thinner films (15 and 80 nm) grown at 30 °C, those grown at 60 °C, do not exhibit an ordered layered structure within the grains. On the contrary, some clusters of the thicker film (150 nm thick) exhibit small terraces typical of layer-by-layer growth. Furthermore, in this film (Figure 5.6f) the striped domains in some clusters are visible. As in the films grown at 30 °C, the PSD plots do not exhibit any significant

difference among the films with different thickness (Figure 5.8b). At this temperature the PSD plot shows a spatial correlation at high spatial frequency.

In the films grown at 90 °C (Figure 5.6g–i), the presence of a terraced structure that is typical of oligothiophene crystals or layered thin films can be observed. The smallest step observed between adjacent terraces was 2.0 ± 0.2 nm, which is consistent with the expected height of a monolayer of T5 molecules (molecular length, 2.2 nm) oriented almost normal with respect to the substrate. The samples exhibit larger islands compared to those of the samples grown at lower temperature, whose size ranges from 0.7 to 1 μm . In the films grown at 90 °C, the striped domains within the grains are not visible. The PSD do not exhibit strong differences among the different thicknesses (Figure 5.8c). However, in this case, the spatial correlation is not clear.

Figure 5.8d shows the trend of autocorrelation length measured from PSD versus the temperature of film growth. The graph shows a good agreement among the correlation length at 30 and 60 °C, which disappears at high temperature. The plot of correlation length with respect to the deposition temperature (Figure 5.8d) shows that the surface exhibits correlation up to 60 °C. At 90 °C, the surface correlation is seen to disappear; further studies are required to investigate the cause of this behaviour. The correlation length is also seen to rise steadily with temperature up to 90 °C.

5.3.2.3 Field-effect transistors

Thin film transistors have been realized, using the three different materials at different substrate deposition temperatures (30, 60 and 90 °C). The measurements were performed in air. All compounds showed typical p-type FET behaviour. Examples of the I – V characteristics of the devices are reported in Figure 5.9 (T5), Figure 5.10 (T5Me) and Figure 5.11 (T5A).

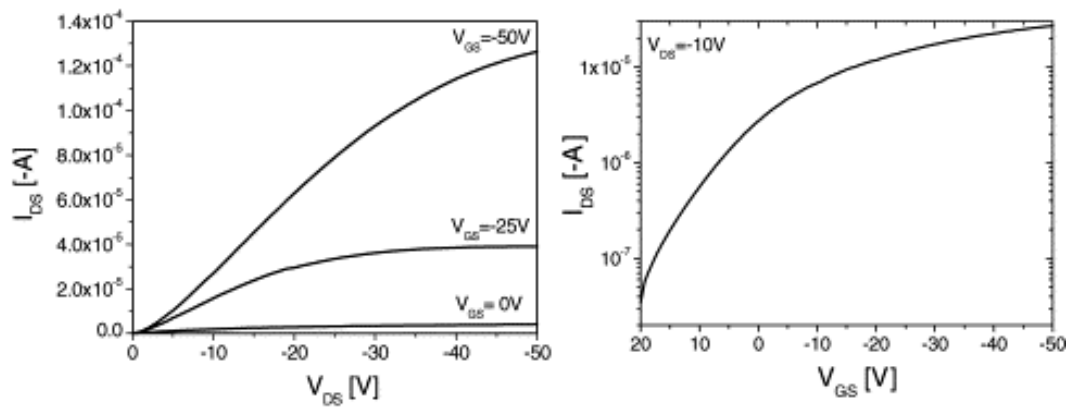


Figure 5.9 *Left*: Plot of the drain current I_D vs. drain voltage V_{DS} at different gate voltages (V_{GS}) obtained for a 150 nm thick film of T5A deposited at a substrate T of 30 °C. *Right*: Semilogarithmic plot of I_D vs. V_{GS} at $V_{DS} = -10$ V.

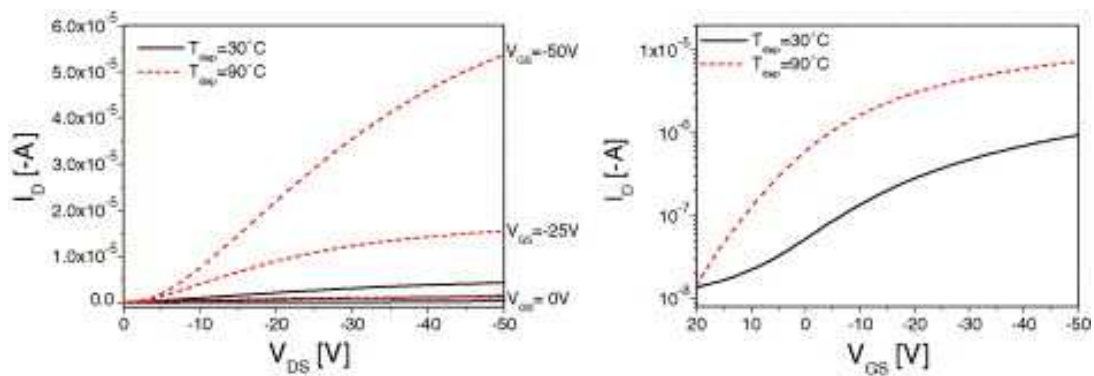


Figure 5.10 *Left*: Plot of the drain current I_D vs. drain voltage V_{DS} at different gate voltages (V_{GS}) obtained for a 80 nm thick film of T5 deposited at a substrate T of 30 °C. *Right*: Semilogarithmic plot of I_D vs. V_{GS} voltage at $V_{DS} = -10$ V.

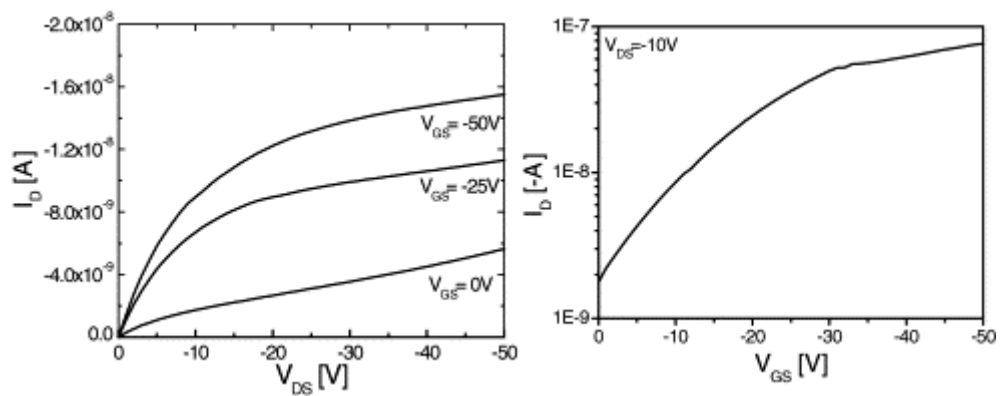


Figure 5.11 *Left*: Plot of the drain current I_D vs. drain voltage V_{DS} at different gate voltages (V_{GS}) obtained for a 150 nm thick film of T5Me deposited at a substrate T of 30 °C (continuous line) and at 90 °C (dotted line). *Right*: Semilogarithmic plot of I_D vs. V_{GS} at $V_{DS} = -10$ V.

Table 1 shows the carrier mobilities, I_{on}/I_{off} ratios and threshold voltages for devices obtained with films of T5 of different thicknesses and deposited at different substrate temperatures. The values reported for carrier mobility and threshold voltage are obtained by drawing the square root of the saturation current (taken at $V_{DS} = V_{GS}$) as a function of the gate voltage. Indeed, in the saturation regime, the expression of the drain current can be simplified, assuming that dopant and carrier concentration are equal, as in (5.1):

$$I_{D,sat} = \frac{W\mu C_i(V_{GS} - V_T)^2}{2L} \quad (5.1)$$

Table 5.1. Charge mobility, I_{on}/I_{off} ratio and threshold voltage for T5 as a function of film thickness and substrate deposition temperature

Substrate T (°C)	Thickness (nm)	Carrier mobility ($\text{cm}^2/\text{V s}$)	I_{on}/I_{off}	Threshold voltage (V)
30	15	8.4×10^{-4}	10^4	-0.05
	80	1.7×10^{-2}	10^3	0.8
	150	1.8×10^{-2}	10^3	4
60	15	2.0×10^{-2}	10^2	9
	80	2.7×10^{-2}	10^1	5
	150	1.3×10^{-2}	10^2	6
90	15	9.0×10^{-3}	10^2	3
	80	4.9×10^{-2}	10^1	20
	150	7.8×10^{-2}	10^2	23
140	150	2.2×10^{-2}	10^1	5

In Eq. (5.1), C_i is the insulator capacitance per unit area ($5.16 \text{ nF}/\text{cm}^2$), W and L the channel width and length, respectively, and V_T is the threshold voltage. From (5.1) a value for the carrier mobility is obtained assuming a constant mobility [17].

As shown in the table, the carrier mobility of T5 is always around $10^{-2} \text{ cm}^2/\text{V s}$. The only film with a lower mobility value is the 15 nm thick one deposited at 30 °C.

For the thicker T5 films (80 and 150 nm) we observe a slight and progressive increase in carrier mobility with substrate deposition temperature up to $7.8 \times 10^{-2} \text{ cm}^2/\text{V s}$, which is the highest value

reported so far for this compound. The value of threshold voltage is near 0 V for the films deposited at room temperature (4 V for the thicker film) and increases with the deposition temperature, reaching 20 V at 90 °C. Similarly, the $I_{\text{on}}/I_{\text{off}}$ ratio decreases at higher deposition temperatures, due to the higher conduction of the FET device.

Carrier mobilities, $I_{\text{on}}/I_{\text{off}}$ ratios and threshold voltages for devices obtained with 150 nm thick films of T5Me and T5A deposited at different temperatures, are given in Table 5.2.

Table 2. Charge mobility, $I_{\text{on}}/I_{\text{off}}$ ratio and threshold voltage of T5Me and T5A as a function of substrate temperature

	Substrate T (°C)	Carrier mobility ($\text{cm}^2/\text{V s}$)	$I_{\text{on}}/I_{\text{off}}$	Threshold voltage (V)
T5Me	30	7.5×10^{-4}	10^2	-5
	60	1.6×10^{-3}	10^2	-5
	90	9.2×10^{-3}	10^3	-5
T5A	30	4×10^{-6}	10^1	
	60	9×10^{-6}	10^1	
	90	2×10^{-5}	10^2	
	140	8×10^{-4}	10^1	

Film thickness is 150 nm.

Both compounds display much lower charge mobilities than T5, with a trend towards higher mobilities on increasing the substrate deposition temperature, more accentuated than in T5.

We can observe that the introduction of structural modification in the aromatic backbone affects the carrier mobility of the material. In particular, introducing two methyl groups at the β -terminal

positions, the carrier mobility is two orders of magnitude smaller than that of T5, while introducing acetylenic spacers lowers the carrier mobility of almost four orders of magnitude. Moreover, Table 5.2 shows that the threshold voltage of T5Me does not change with temperature.

5.4 Discussion and conclusion

It is well known that the vacuum evaporated thin films of thiophene oligomers tend to orient with the long axis perpendicular to the substrate, with a tilt angle with respect to the normal, which depends on the molecular structure and deposition conditions and that charge transport occurs preferentially in plane [1,2,6,18].

XRD and AFM measurements performed on T5 offer a key to interpreting the trend of variation of the electrical characteristics of the FET devices on increasing the substrate deposition temperature of the active layers.

First of all, the AFM image reported in [Figure 6.a](#) indicates that the low carrier mobility ($8.4 \times 10^{-4} \text{ cm}^2/\text{V s}$) of the 15 nm thick film of T5 grown at a substrate deposition temperature of 30 °C is due to an incomplete surface coverage. For all the other films the carrier mobility varies in the range $\sim 1 \times 10^{-2}$ to $\sim 8 \times 10^{-2} \text{ cm}^2/\text{V s}$, the highest value being that of the 150 nm thick film grown at 90 °C. For this film, the AFM image shows the presence of a terraced structure typical of layered thin films, with the smallest step between adjacent terraces being consistent with the height of a monolayer of T5 molecules almost upright to the substrate. The fact that the film displays a mobility value of $\sim 8 \times 10^{-2} \text{ cm}^2/\text{V s}$, the highest reported so far for T5, suggests that also the few first layers of the film are organized in the same way. Indeed, it has been demonstrated that in sexithiophene the charge mobility is controlled by the first two monolayers. [15b] However, since in bottom contact FETs the carrier injection is limited to thin lines along the

edges of the contacts, it cannot be excluded that a further contribution to the charge mobility of the film also comes from the presence of larger crystalline domains (as indicated both by XRD and AFM), which allow a more efficient carrier injection and smaller contact resistance.

We relate the increase of “off” currents observed in T5 FET devices (Table 5.1), on increasing the substrate deposition temperature, to the increase in the amount of a second crystalline form of T5, revealed by XRD of thin films deposited at the same temperatures. As shown in Table 1, the presence of a second polymorph has only a small effect on the carrier mobility of T5. However, the growth of the amount of the minority polymorph of T5 on increasing the substrate deposition temperature reduces the degree of order in the film and hence increases the density of structural defects acting as traps in the device. The presence of the traps comes out from the analysis of the threshold voltage values (V_T) of the devices. Indeed, as the oligomer is undoped, the shift of V_T from 0 V towards more positive values can be ascribed to charged defects at the oligomer–SiO₂ interface. Table 5.1 shows that for the film deposited at room temperature, V_T is closed to 0 V (4 V for the thicker film) indicating that both the oxide and the oligomer are relatively free of charge defects, while V_T values increase up to 20 V for deposition at 90 °C. Moreover, the shift of V_T towards large positive values is strictly related to the lowering of the I_{on}/I_{off} ratio, which is due to the higher conduction of the device. It is worth noting that it has recently been demonstrated that carrier transport in thiophene oligomers is traps dominated [2].

Despite the fact that the electronic structure of the frontier orbitals of T5Me and T5A are very similar to those of T5 [6] and despite the highly crystalline nature and larger domains size of their thin films, as determined by XRD, their carrier mobilities are lower than that of T5 by several orders of magnitude (Table 5.2). The increase of

the deposition temperature causes much larger increases in the carrier mobilities of these compounds.

Also in the case of T5Me, XRD data offer a clue to understand the electrical behaviour of the FET device. XRD data show indeed that the increase in deposition temperature causes the reorientation of some crystalline domains. The rearrangement of the material with the deposition temperature is accompanied by a marked increase in the carrier mobility. On the contrary, the threshold voltage is not affected by the temperature, indicating that in the film the temperature change does not cause the increase of charge traps. On the basis of these data, one can infer that the increase in the deposition temperature leads to a more homogeneous alignment and a better stacking of the T5Me molecules with respect to the substrate, thus favouring the carrier mobility.

Probably, this is also the reason why we observe the increase in the carrier mobility with the substrate temperature in T5A. However, in this case, no indications come from XRD plots, which remain the same even at 140 °C. Also, the domain size, around 100 nm as measured by XRD, much larger than that of T5 and T5Me, does not show any variation with temperature. Since, the low carrier mobilities measured for this compound cannot be ascribed to the lack of film crystallinity or to the smaller size of crystalline domains, other factors, such as a poor overlap of the electronic wave functions within the transport layer, related to a looser packing caused by the different molecular shape (Figure 5.1), have to be invoked. An indication in this direction comes from the photoluminescence quantum yield of T5A, which is roughly one order of magnitude greater than that of T5. In thiophene oligomers the photoluminescence in the solid state is generally very low owing to the close molecular packing. Work is currently in progress to elucidate this point.

In conclusion, our data show that in T5 the presence of a second polymorph leads to a remarkable decrease of the $I_{\text{on}}/I_{\text{off}}$ values, whereas it does not affect the carrier mobility values. Substitution of methyl groups at the terminal positions, as in T5Me, or the introduction of acetylenic spacers, as in T5A, prevents the formation of polymorphs but leads to a remarkable decrease in carrier mobility. In the case of T5Me, XRD data indicate that the increase in the substrate deposition temperature affects the orientation of the crystalline domains with respect to the substrate, in a direction that is favourable to the increase of carrier mobility. These data suggest that the good results achieved with oligothiophenes terminated by long alkyl chains [1] are related both to the absence of polymorphs and to the homogeneous orientation of the crystalline domains with respect to the substrate.

We believe that systematic electrical characterization of libraries of purposely synthesized molecules, paralleled by thin film XRD and AFM measurements, will allow the different factors contributing to charge transport, from the energy of HOMO and LUMO frontier orbitals to crystalline domains size and orientation to intermolecular overlap of the electronic wave functions - to be disentangled. In this way, it will be possible to establish the molecular structure/electrical properties relationships that will allow the rationale design of better performing materials.

References

- [1] M. Halik, H. Klauk, U. Zshieschang, G. Schmid, S. Ponomarenko and S. Kyrchmeyer, *Adv. Mater.* **15**, 917 (2003).
- [2] S. Mohapatra, B.T. Holmes, C.R. Newman, C.F. Prendergast, C.D. Frisbie and M.D. Ward, *Adv. Funct. Mater.* **14**, 605 (2004).
- [3] (a) T.W. Kelley, D.V. Muires, P.F. Baude, T.P. Smith and T.D. Jones, *Mater. Res. Soc. Symp. Proc.* **771**, L6.5.1 (2003); (b) H. Meng, M.

- Bendikov, G. Mitchell, R. Helgeson, F. Wudl, Z. Bao, T. Siegrist, C. Kloc and C.H. Chen, *Adv. Mater.* **15**, 1090 (2003); (c) S.E. Fritz, S.M. Martin, C.D. Frisbie, M.D. Ward and M.F. Toney, *J. Am. Chem. Soc.* **126**, 4084 (2004).
- [4] (a) R. Hajlaoui, G. Horowitz, F. Garnier, A. ArceBrouchet, L. Laigre, A. ElKassmi, F. Demanze and F. Kouki, *Adv. Mater.* **9**, 389 (1997). (b) R. Hajlaoui, D. Fichou, G. Horowitz, B. Nessakh, M. Constant and F. Garnier, *Adv. Mater.* **9**, 557 (1997).
- [5] C.D. Dimitrakopoulos and P.R.L. Malenfant, *Adv. Mater.* **14**, 99 (2002)
- [6] (a) M. Melucci, M. Gazzano, G. Barbarella, M. Cavallini, F. Biscarini, P. Maccagnani and P. Ostoja, *J. Am. Chem. Soc.* **125**, 10266 (2003). (b) M. Melucci, G. Barbarella, M. Zambianchi, P. Di Pietro, A. Bongini, *J. Org. Chem.*, **69**, 4821 (2004).
- [7] (a) D. Jones, M. Guerra, L. Favaretto, A. Modelli, M. Fabrizio and G. Distefano, *J. Phys. Chem.* **94**, 5761 (1990); (b) K. Meerholz and J. Heinze, *Electrochim. Acta* **41**, 1839 (1996).
- [8] A.R. Murphy, J.M.J. Fréchet, P. Chang, J. Lee and V. Subramanian, *J. Am. Chem. Soc.* **126**, 1596 (2004).
- [9] R.J. Chesterfield, C.R. Newman, T.M. Pappenfus, P.C. Ewbank, M.H. Haukaas, K.R. Mann, L.L. Miller and C.D. Frisbie, *Adv. Mater.* **15**, 1278 (2003).
- [10] A. Facchetti, M.H. Yoon, C.L. Stern, H.E. Katz and T.J. Marks, *Angew Chem. Int. Ed.* **42**, 3900 (2003).
- [11] P. Ostoja, P. Maccagnani, M. Gazzano, M. Cavallini, J. C. Kengne, R. Kshirsagar, F. Biscarini, M. Melucci, M. Zambianchi and G. Barbarella, *Synt. Met.* **146**, 243 (2004).
- [12] W. Porzio, S. Destri, M. Mascherpa and S. Brückner, *Acta Polym.* **44**, 266 (1993).
- [13] (a) L. Antolini, G. Horowitz, F. Kouki and F. Garnier, *Adv. Mater.* **10**, 382 (1998). (b) T. Siegrist, C. Kloc, R.A. Laudise, H.E. Katz and R.C. Haddon, *Adv. Mater.* **10**, 379 (1998).
- [14] (a) G. Horowitz, B. Bachet, A. Yassar, P. Lang, F. Demanze, J.L. Fave and F. Garnier, *Chem. Mater.* **7**, 1337 (1995). (b) T. Siegrist, R.M. Fleming, R.C. Haddon, R.A. Laudise, A.J. Lovinger, H.E. Katz, P. Bridenbaugh and D.D. Davis, *J. Mater. Res.* **10**, 2170 (1995).

- [15] H.P. Klug and L.E. Alexander, *XRD Procedures for Polycrystalline and Amorphous Materials*, Wiley-Interscience, New York (1974).
- [16] (a) F. Biscarini, P. Samori, O. Greco and R. Zamboni, *Phys. Rev. Lett.* **78**, 2389 (1997) (b) F. Dinelli, M. Murgia, P. Levy, M. Cavallini, F. Biscarini and D.M. de Leeuw, *Phys. Rev. Lett.* **92**, 1168021 (2004).
- [17] G. Horowitz, Physics of organic field-effect transistors In: G. Hadziioannou and P.F. van Hutten, Editors, *Semiconducting Polymers*, Wiley, **463** (2000).
- [18] F. Garnier, A. Yassar, R. Hajlaoui, G. Horowitz, F. Deloffre, B. Servet, S. Ries and P. Alnot, *J. Am. Chem. Soc.* **115**, 8716 (1993).

Appendix

Atomic Force Microscopy (AFM)

Figure A.1 shows the scanning probe microscope we have used to investigate the topography of samples. The instrument was built by the CP research and it can work very well both as AFM and as STM.

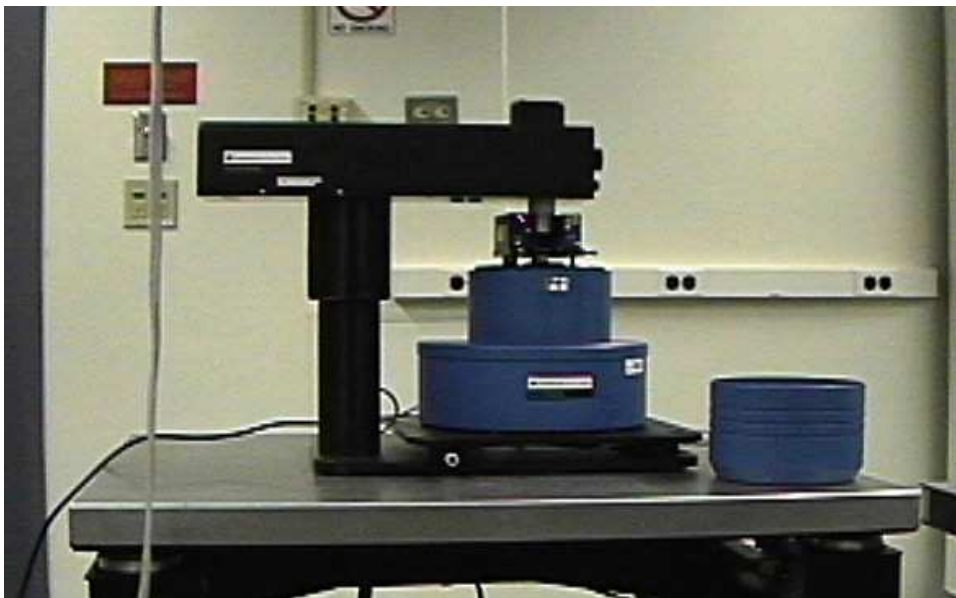


Figure A.1. Schematic representation of the Autoprobe SPM of the CP research.

Atomic force microscopy was first implemented in 1986 with the goal of overcoming the STM limitation of imaging only conductive samples. The principle is thus not related to the measurement of a tunneling current, but of the probe-sample interactions. The idea is to use a tip attached to the end of a cantilever with elastic constant K , and measure the tip-sample forces by the cantilever deflection, which are related, according to Hooke's law, by

$$F_z = K * \Delta Z \quad (\text{A.1})$$

The same relation applies for the x direction if the force on the tip has also a component along the surface plane. There are various detection systems for the cantilever deflection, [1] but the most common one is the optical beam deflection method shown in Figure A.2. In this system, a laser beam is focused on the cantilever and reflected towards a position-sensitive photodiode. Initially the reflection is centred with respect to the photodiode, but as soon as the cantilever is deflected by the tip-sample forces, the reflection on the photodiode is displaced. Normal forces bend the cantilever in the z direction, while the main effect of lateral forces is the torsion of the cantilever, leading to displacements of the reflection in the vertical and horizontal directions, respectively. The photodiode is divided into four independent parts (sectors A, B, C and D as shown in Figure A.2).

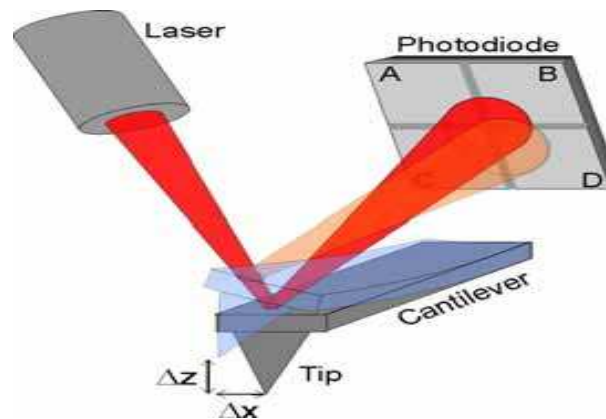


Figure A.2 Schematic description of the detection system of the cantilever deflection

Each of them generates a voltage proportional to the total intensity it receives, and the displacements of the reflected beam on the photodiode are quantified by measuring the changes in the relative voltages of the four sectors. Thus, normal forces are related to the signal

$$V_z = (V_A + V_B) - (V_C + V_D) \quad (\text{A.2})$$

and lateral forces to the signal.

$$V_x = (V_A + V_C) - (V_B + V_D) \quad (\text{A.3})$$

The calibration to correlate the measured signals to the tip displacements Δz and Δx , or to the tip-sample forces by applying Hooke's law, depends on the cantilever and tip characteristics (dimensions, Young modulus) and thus has to be performed for every different tip. [1]

The general behaviour of the tip-sample forces versus distance is shown in Figure A.3.

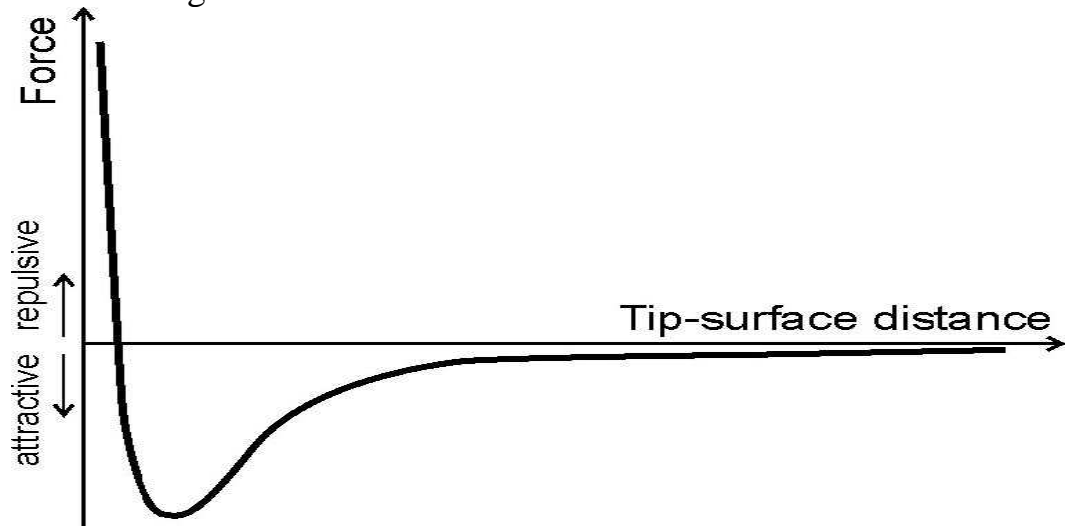


Figure A.3 Tip.sample force vs distance.

The Figure A.3 is the plot of the non monotonic behaviour of the forces versus distance with contributions of long range attractive interactions and short range repulsive interactions. This presents an additional complication inherent to AFM, since a stable feedback is only possible on a monotonic subbranch of the feedback signal.

The AFM measurements can be performed in different modes, which can be classified into the contact mode and the dynamic modes.

a. Contact mode

In the contact-mode, the tip is brought in contact with the surface and the tip-sample interaction forces are measured recording the cantilever deflection. At this point, many different interaction forces contribute to the deflection. Among them, there are long range Van der Waals or electrostatic forces, short range repulsive forces due to the overlap of tip and sample electronic orbitals, or adhesion forces. The adhesion forces depend on the contact area, which in turn depends on the tip radius and the stiffness of probe and sample. Furthermore, adhesion is greatly enhanced in presence of water adsorbed on the surface, which forms meniscus bridges between tip and sample. This contribution, however, can be cancelled by performing the measurements in a liquid environment.

In general, the topography measurements are performed by scanning the surface at constant force (i.e., constant cantilever deflection). When the tip is scanned over a bump or hollow, the tip will follow the surface by changing the cantilever deflection. The consequent change in the measured signal is used as a feedback to readjust the cantilever-surface distance and get back to the initial deflection. In this way, the recorded changes in the cantilever-surface displacements correspond to the topography of the sample. Obviously, the deflection of the cantilever should be significantly larger than the deformation of tip and sample upon contact. To satisfy this, the cantilever should be softer than the interatomic bonds in tip and sample. Typical interatomic spring constants range from 10 to 100 N/m, though in biological samples they can be as low as 0.1 N/m. Thus, typical values for contact-mode cantilever spring constants are 0.01-5 N/m.

The images of the measured topographic features are broadened (for protrusions) or narrowed (for hollows) by the lateral size of the

tip (with typical curvature radius for commercial tips from 5 to 15 nm). This effect consequently has to be considered in the interpretation of images with features in the nm range. [1,3] Nevertheless, sub-nanometer resolution images can be obtained on crystalline surfaces, resolving the surface structure. This is explained taking into consideration the large contact area of tip and sample (in comparison with the crystal periodicity) and considering that the forces matching the surface periodicity are transmitted to the tip, resulting in an “averaged image” of the periodic lattice. In this way, small periodicities can be resolved if they extend over distances much larger than the contact area.

The optical beam deflection method used for the detection of the cantilever deflection allows the simultaneous measurement of both the normal deflection and the cantilever torsion generated by lateral forces. It is well known that, during the lateral displacement of a solid over a surface, there is a force opposing to the movement. This force is the friction and is also present when scanning the surface with the tip, consequently leading to a measurable torsion of the cantilever. On a microscopic scale, there are many different processes involved in the friction, but for a thorough description of the underlying theory the reader is referred to references. [1,5]

b. Dynamic modes

In the dynamic modes the cantilever is deliberately vibrated by externally exciting it with an excitation amplitude A_{ex} and an excitation frequency ω . The cantilever oscillation is characterized by its amplitude, the frequency, and the phase difference between excitation and oscillation. In order to provide an understanding of the fundamental concepts involved in dynamic mode AFM, the cantilever can be described by harmonic approximations. In the absence of tip-surface interactions (i.e. tip far away from the

surface) the movement of the tip can be considered as a forced harmonic oscillator with damping, thus following

$$m\ddot{Z}(t) = -\frac{m\omega_0}{Q}\dot{Z}(t) - KZ(t) - KA_{ex}\cos(\omega t) \quad (\text{A.4})$$

where $\omega = (k/m)^{1/2}$ is the resonance frequency of the free cantilever, and Q is the dimensionless quality factor related to the damping of the cantilever. The solution is a linear combination of a transient term related to the adaptation of the cantilever movement to the excitation frequency, and a steady-state term with constant frequency, amplitude and phase over time:

$$Z(t) = A_t e^{-\omega_0 t / 2Q} \sin(\omega_0 t + \varphi_t) + A_0 \cos(\omega t + \varphi) \quad (\text{A.5})$$

After a time $\tau = 2Q/\omega_0$ the transient term is reduced by a factor $1/e$ and the motion is dominated by the steady term. If we evaluate now the steady solution in the differential equation, the following expressions are found for the amplitude and phase as a function of ω :

$$A_0 = \frac{A_{ex} Q \omega_0^2}{\sqrt{\omega^2 \omega_0^2 + Q^2 (\omega_0^2 - \omega^2)^2}} \quad (\text{A.6})$$

$$\varphi = \arctan\left(\frac{\omega \omega_0}{Q(\omega_0^2 - \omega^2)}\right) \quad (\text{A.7})$$

The corresponding diagrams of amplitude and phase vs. ω are shown in Figure A.4, calculated for A_{ex} , Q and ω_0 values of 10 nm, 10 and 10 kHz respectively. From equation (A.6) it can be seen that the damping causes the maximal amplitude to be obtained at a frequency

$$\omega_0 = \omega_0 \sqrt{1 - \frac{1}{2Q^2}}. \quad (\text{A.8})$$

However, the shift is negligible for Q values in the usual range of 100 or more.

Up to now, no interaction forces have been considered. The simplest case would be a tip-sample force whose range of interaction is much larger than the oscillation amplitude and with a gradient with respect to the tip-sample distance which does not vary significantly over one oscillation cycle.

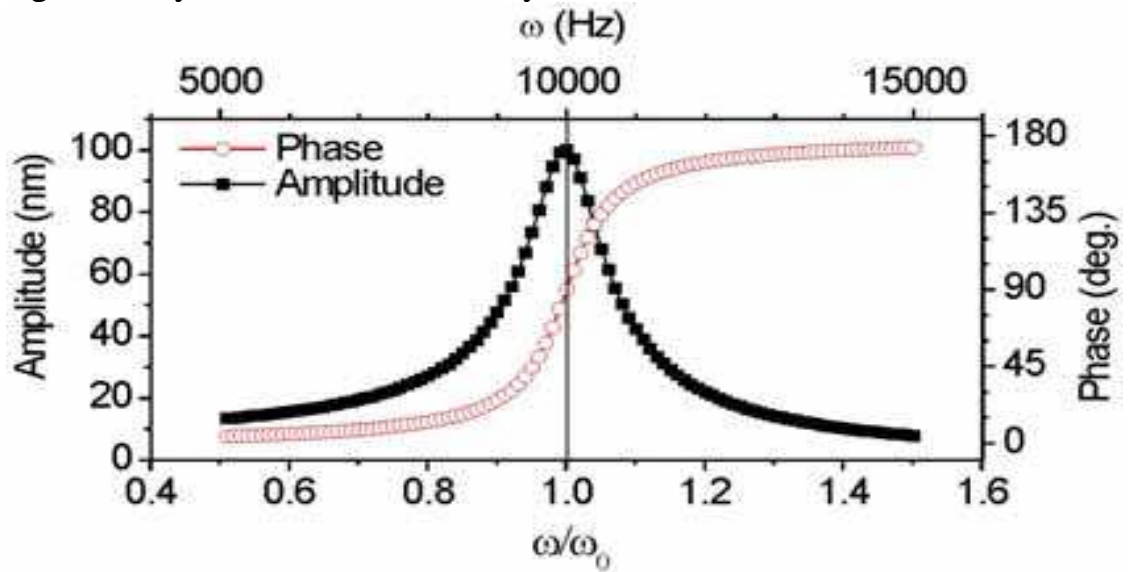


Figure A.4 Amplitude and phase diagrams vs frequency for a free cantilever, calculated for A_{ex} , Q and ω_o value of 10nm, 10 and 10KHz respectively.

This gradient can thus be represented by a spring constant k_{ts} which varies with the average tip-sample distance but is nearly constant within an oscillation cycle. In this case, the tip-sample force can be included in the movement equation (A.4) by simply considering a new spring constant

$$K_{total} = K + K_{ts} = K + \frac{\partial F_{ts}}{\partial Z} \quad (\text{A.9})$$

which consequently leads to a new resonance frequency shifted by $\Delta\omega$ (neglecting the damping) at

$$\omega^2 = (\omega_0 + \Delta\omega)^2 = \frac{K_{total}}{m} = \frac{K + \frac{\partial F_{ts}}{\partial Z}}{m} \quad (\text{A.10})$$

A change in the resonance frequency leads to a shift of the curves in Figure A.4, consequently changing also the oscillation amplitude and phase.

This analytic and simplified model shows qualitatively that in dynamic force microscopy the oscillation parameters depend on the force gradient, as opposed to the dependence on the force itself in the contact-mode, and that the tip-sample interaction influences all of the oscillation parameters, that is, the resonance frequency, amplitude and phase. However, the approximations made often do not hold for real

measurements, and much more complex models and numeric calculations have to be developed to get quantitative agreement with the experiments.

Dynamic force microscopy is performed in two different measurement modes: tapping mode or amplitude modulation, and non-contact mode or frequency modulation. Both of them have been used in the frame of this thesis and are briefly presented in the following.

i. **Tapping mode**

In this mode the cantilever is excited externally with a constant excitation amplitude at a constant frequency near its resonance. The measured signals are the oscillation amplitude and phase, and the former is used as feedback parameter while scanning the sample. The initial oscillation amplitude decreases upon reduction of the tip-sample distance, which is typically reduced until the amplitude is decreased to 40 to 90 % of its initial value. Then, while scanning

the surface, a feedback loop controls the cantilever-sample distance in order to maintain the amplitude constant. Typical oscillation amplitudes are in the range of 10 to 100 nm, consequently encountering a wide range of tip-sample interactions within each cycle, including both attractive as well as repulsive forces. This is what makes an analytical description of the processes taking place very difficult. Some of the models and numerical simulations applied to get some understanding of the tip-sample interactions can be found in references. [1,6,7]

ii. **Non-contact mode**

The time constant τ for the transient term in the oscillation amplitude to adjust to a change in the tip-sample interaction scales with $2Q/\omega_o$. In vacuum, typical quality factors are in the range of 10000, making the data acquisition in the tapping mode (with the amplitude as feedback parameter) too slow for vacuum applications. Albrecht et al. developed in 1991 the non-contact measurement mode, where the change in frequency settles on a time-scale of $1/\omega_o$ thus overcoming this problem. [8] Its working principle is as follows: the cantilever is excited and the oscillation parameters recorded. These are in turn used in a feedback loop to control the excitation signal in such a way that the excitation is with the same frequency but phase-shifted by 90 degrees (therefore exciting in resonance) and with a variable excitation amplitude that keeps the oscillation amplitude constant. Consequently, the only degree of freedom left for the cantilever to adjust to a changing tip-sample interaction is a change of its resonance frequency. This signal is used in a second feedback loop to adjust the cantilever-surface distance while scanning the surface and keeping a constant oscillation frequency. Despite the fact that there is no tip-surface mechanical contact while measuring, upon the appropriate choice of the experimental parameters, the tip-sample interactions can include

contributions of short-range forces when the tip is closest to the surface. This in turn allows obtaining images with atomic resolution and corrugations in the same order of magnitude as for STM. imaging. [1,9] The excitation amplitude necessary to keep the oscillation amplitude constant is simultaneously recorded and is directly related to the energy dissipation within one oscillation cycle. This, together with maps of the averaged tunneling current for the oscillating tips, or frequency shift vs. cantilever-surface distance curves, are additional data available with non-contact AFM, which are related to different material properties. However, these kinds of measurements have not been used in this thesis and their description can be found elsewhere. [1,9]

References

- [1] B. Bushan, *Handbook of nanotechnology*, Springer (2004).
- [2] D. J. Keller, F. S. Franke, images, *Surf. Sci.* **294**, 409 (1993).
- [3] F. Biscarini, P. Levy, *Appl. Phys. Lett.* **71**, 888 (1997).
- [4] B. Persson, *Sliding friction, physical principles and applications*, Springer Verlag, Berlin, Heidelberg, New York (1998).
- [5] F. P. Bowden, D. Tabor, *The friction and lubrication of solids*, Clarendon, Oxford (1964).
- [6] R. Garcia, R. Perez, *Surf. Sci. Rep.* **47**, 197 (2002).
- [7] R. Garcia, C. J. Gomez, N. F. Martinez, S. Patil, C. Dietz, R. Magerle, *Phys. Rev. Lett.* **97**, 016103 (2006).

[8] T. R. Albrecht, P. Grütter, D. Horne, D. Rugar, *J. Appl. Phys.* **69**, 668 (1991).

[9] F. J. Giessibl, *Rev. Mod. Phys.* **75**, 949 (2003).

Acknowledgements

For those who are not going to read anything but this, I want to take the chance to remind you that I was studying for the last three and half years the self organisation of rotaxanes thin films into spatially correlated nanostructures, the growth, the morphology and the structure of organic semiconducting thin films.

Now, I can start with the acknowledgements to those who have contributed in one way or another to the completion of this thesis.

The four persons without whom the accomplishment of this thesis would be impossible are: Dr Fabio Biscarini, Prof. Aldo Brillante, Dr Massimiliano Cavallini, and Dr Elisabetta Venuti.

I have learnt a lot from their scientific intuition and know-how. Thanks to their good humour.

I also wish to thank a lot:

- all the member of Biscarini's group (about 20 persons) and Brillante's group , in particular Dr. Ivano Bilotti for his help.
- my best friends dott. Remy Chassem, dott. Christophe Kuinan, Justin Kamga, Lise Chekam, Alain Tafou etc.....because they are numerous.
- my brother, sisters and relative in Italy and Cameroon.
- all the persons who have believed like me in this job.
- those who don't know the importance of a PhD. Make god forgive them.

A particular acknowledgement to

- Fabio Biscarini for providing the financial support and for giving me the opportunity of working under such excellent experimental conditions and with such a group.
- to my daughter Loraine Kengne, since she is the most important person in my life. She makes me forget many things. These two last years, she has been my stimulus, giving me energy to organise myself, like rotaxanes upon annealing.